Reviewer #1 (R#1):

First of all, we would like to thank the anonymous reviewer for the detailed and helpful comments. In the following, we first state the comment of the reviewer (R#1-X, except for the 'general comment') and then give our response. References to the manuscript are related to the original discussion manuscript: P2L30 → page 2, line 30.

General comments: The study nicely illustrates a use-case for the MAMAP instrument and how the combined use of airborne remote-sensing and in-situ instruments can help to assess emissions from a landfill site. Unfortunately, the structure of the paper is confusing and should be revised to help the reader to focus on the key results (see general comments below). For example, the methodology of how uncertainties are calculated (e.g. for CH4 emission rates) is given in the results section (6), while other results are given in the emission comparison section (7). I would suggest to include the comparison with the inventory in the results section. Furthermore, the uncertainty calculation should either be a specific section or logically added to section (5), where the MAMAP retrieval and calculation of emission rates are described. In the last paragraph of the conclusion, the authors claim that this study shows that this type of airborne remote sensing observations are "well-suited" to estimate CH4 emissions from a "large landfill". Yet, the study showed that for 3 out of 4 landfills investigated, the instrument did NOT detect a significant plume. Here the authors need to critically discuss: Why were the other sites neglected in the analysis and conclusions? What were the EPA emission estimates for the other sites? Maybe there is a detection limit for this methodology or are there other limiting external factors (e.g. meteorology, topography of the site)? These would be crucial information to be added. All that can really be claimed seems to be that, in this instance, a landfill with emissions of above ca. 11ktCH4/a can be monitored using this technique. Concerning the size of the landfill ("large landfill") – I doubt that the size of the landfill is critical here, but rather its CH4 emissions, or maybe its CH4 emission density.

We agree with the reviewer about his/her major concerns regarding the structure of the manuscript and the not existing comprehensive discussion on the three other landfills. We significantly restructured the manuscript – further details are given in the specific responses to R#1-4, R#1-6, R#1-9, R#1-11, R#1-12, R#1-14, R#1-17 and R#1-18. We added a more comprehensive discussion on the three other landfills and also expanded our claims on the suitability of remote sensing measurements for quantifying emission from landfills – further details are given in the specific responses to R#1-3, R#1-20, R#1-21.

R#1-1) P2 Line 7: consider citing a peer-reviewed publication instead of a webpage here, http://www.earth-syst-sci-data.net/8/697/2016/essd-8-697-2016.pdf

Done. We updated the reference and replaced Kirschke et al. (2013) by Saunois et al. (2016). Additionally, we also stated the new estimates (P2L7) as given by Saunois et al. (2016) for the year 2012. The final revised version of the manuscript of Saunois et al. (2016) was not published at the time this manuscript (Krautwurst et al., 2016) was written. Therefore we had referenced the older values from Kirschke et al. (2013).

R#1-2) P2 L30f: Please give an order of magnitude for the size. As a significant share of publications in AMT focus on regional to global scale studies, a landfill might not qualify as having a *large* surface area.

We agree. At this position in the manuscript, the term 'relatively large' might be confusing for the reader (later in the manuscript, P5L5, the approximate size is stated. In comparison to emissions

from point sources like power plants or coal mine ventilation shafts, a landfill has a relatively large area from which emissions can potentially develop.) In order to avoid any confusion, we added a size indication 'up to some square kilometres' on P2L30.

R#1-3) P4 L6f: A more diligent reason for why 3 out of 4 landfills are ignored in the manuscript from here on out needs to be given. Why do those other landfills not produce pronounced plumes? What are their (EPA) estimated emissions? Are they lower, equal or higher than the expected emissions at Olinda Alpha? Consider adding a table with the key indicators for all 4 sites.

The aim of this study was not to survey and measure all landfills in the Los Angeles Basin but to show, that it is possible to derive emission rate estimates from remote sensing measurements in the short-wave infrared (SWIR) region. The measurement flights analysed in this manuscript were part of the CO_2 and Methane Experiment (COMEX). COMEX was also dedicated to other target types and effects, which were related to the satellite concept missions HyspIRI and CarbonSat. Therefore, the measurement time allocated to landfills was limited. As described in the manuscript (Sect. 4, "Flight strategy"), a target (in this case one of the landfills) was first surveyed by the remote sensing instrument utilising the capabilities of the developed real-time retrieval. Due to the limited amount of flight hours dedicated to landfill measurements, it was decided to gather in-situ measurements within the boundary layer for validation purposes primarily if a plume like structure had already been observed by the remote sensing instrument. As seen in the overview plot (Fig. 1), only the Olinda Alpha Landfill showed pronounced plume like structures in the remote sensing data. In order to show, that remote sensing measurements in the SWIR region have the potential to detect and quantify emissions from landfills, the focus was set to the most promising target, the Olinda Alpha Landfill.

Nevertheless, we agree that the manuscript would benefit from a more comprehensive discussion on the three other landfills, especially, why these landfills do not produce pronounced plumes. Therefore, we added the estimated EPA inventory values for 2014 of all landfills to the main manuscript (Sect. 2 "Campaign and target description", P4L5ff) and also added a more comprehensive overview regarding the reported emissions of the four landfills over the past years and a description of the used methodology how these emissions were estimated in the supplementary material (New Sect. S9, "Landfill reporting practice in the U.S."). Additionally, a further discussion, where we investigated the detection limit of the MAMAP instrument for the other landfills using Observation System Simulation Experiments (OSSEs), was added at the end of the manuscript (see comment to R#1-20).

R#1-4) P4 L9: Why are: "Campaign and target description", "Aircraft instrumentation and collected data sets" and "Flight strategy" three different sections? Please consider combining them as subsections into one "methods" section.

We agree with the reviewer but we would rather call the section "Measurements" instead of ''Methods" because the actual methods to retrieve concentrations and emission rates are presented in Sect. 5. Thus, the three sections were summarized by the new section "Measurements".

R#1-5) P5 L12: Please correct CDRS to CRDS

Done.

R#1-6) P5 L14: What is the uncertainty of total column concentrations determined with the MAMAP instrument? There is a discussion of this in the "results" sections. Please consider moving this discussion into the method section of the paper.

In general, the single measurement precision of the retrieved total column concentrations of CH_4 (or normalised column-averaged dry air mole fractions of CH_4, XCH_4) is better than 0.4% (Krings et al., 2013) and was added in Sect. 3 "Aircraft instrumentation and collected data sets" (P5L17). In this context, accuracy is of less importance due to the normalisation of the retrieved columns with the local background beforehand to the flux estimate, see P9L23-25.

R#1-7) P5 L25: What was the typical uncertainty (repeatability and reproducibility) of the in-situ measurements

The uncertainty of the Picarro greenhouse gas in-situ analyser has been estimated to around 0.15 ppm for dry CO_2 and 2.3 ppb for dry CH_4 as determined from laboratory experiments. This uncertainty estimates contain also the contribution due to repeatability of the measurements, whereas by far the largest contribution originates from the water vapour and water vapour correction, respectively. We added the relevant parameters on P5L29.

R#1-8) P7 L10: Please consider adding the flight track of the second instrument hosting the AVIRIS-NG on Figure 2 if possible.

This is a good idea, especially for a comparison of the dimensions, but one has to be careful not to clutter Fig. 2 with details and lines, respectively. The second remote sensing instrument AVIRIS-NG aboard a second Twin Otter gathered five flight tracks in total (compare to Sect. S6 in the supplementary material). In order to keep Fig. 2 clear, only one flight track (flight track shown in Fig. S18, c, in the supplementary material and in Figs. 9, b, and 11 in the main manuscript) was added. In case, the reader is interested in the position of another flight track, the landfill is emphasised in Fig. S18 for reference purposes. The approximate dimensions of such a flight line were given in Sect. 6.3 (P24L20).

R#1-9) P9 L2f: The resulting uncertainty of choosing 0.31 as mean albedo could be discussed here. (Similar point for other assumptions/simplifications made throughout section 5).

We agree and performed a simple error analysis for the parameter 'surface albedo' to examine its influence on the final emission rate estimate. For that, RTM simulations were performed with the two extreme cases of the surface albedo of 0.22 and 0.40. The resulting effect on the final fluxes was less than 1% for all cases and was added in Table 2.
Additionally, we shifted the methodology of how the uncertainties were calculated to Sect. 5 (see also R#1-11).

R#1-10) P10 L3: The authors correctly note that the estimated emissions are only valid during the overflight, yet the units indicate an annual estimate. Suggestion: report the emissions as tCH4 per hour and also calculate the mean hourly emission according to EPA. This avoids the erroneous implication that annual emission rates can be calculated from this data set.

We do not agree and consider the unit $ktCH_4/yr$ as more convenient for our purposes. It allows for easy comparison to inventories and to previous publications. As mentioned by the reviewer, we clearly stated in the manuscript that the derived emission rates are strictly speaking only valid for the time of the overflight.

R#1-11) P14f: After nicely describing all calculations in section 5, why are the uncertainties associated with these calculations now included in the "results" section and not within the previous section? Are the calculated uncertainties considered a key result of this study? If so, this needs to be stated more clearly.

Agreed. We added the methodology of how errors are calculated to Sects. 5.1 (remote sensing related uncertainties, Sect. 3.1.1 in the revised manuscript) and 5.2 (in-situ related uncertainties, Sect. 3.2.1 in the revised manuscript).

R#1-12) P14/15/16: Here CH4 emissions are reported without any uncertainties and the reader will have to "wait" for the next subsection to judge if emission of 13.0ktCH4/a (27.8.2014) are significantly different from the reported 13.7 ktCH4/a a day later – why?. Please consider restructuring to improve the readability of the manuscript

We agree with the reviewer and added the estimated uncertainties to the estimated emission rates (P14L30, P15L10, P16L6, P16L8) in Sects. 6.1 (Sect. 4.1 in the revised manuscript) and 6.2 (Sect. 4.2 in the revised manuscript) to allow for an immediate assessment.

R#1-13) P18 L6: It seems that only a bias in the determined wind-direction has been accounted for here. What would be the impact of changing wind conditions between two legs of the down-wind legs?

That is true but we would rather call it maximal uncertainty originating from the wind direction uncertainty of 10°. As stated on P18L6, the wind direction affects the flux via modifying the perpendicular wind speed (via a cosine function).
Assuming that all flight tracks of one flight day would be aligned perfectly perpendicular to the prevailing wind direction, the error of the flux due to the wind direction uncertainty of +-10° would then be +-1.5% for each track. One can now assume (as done in the manuscript) that the flux for each track is either wrong by the +1.5% (or -1.5%), which results in a final / total flux also being wrong by +1.5% (or -1.5%).
Applying the suggestion from the reviewer would mean that, e.g., for the first track, the wind direction is wrong by +10°, for the second track, the wind direction is wrong by -10°, for the third track, the wind direction is wrong by +10°, etc. In this case, the error on the final / total flux due to an error in the wind direction would be less because the error contributions of the single tracks can cancel.
Additionally, if the flight tracks are not aligned perpendicular to the wind direction (standard case), the error due to the wind direction becomes asymmetrical. In this case, always the larger error is given in Table 2.

R#1-14) P20 L19: Is subsection 6.1.2 really an independent "result" that needs a subsection or rather additional information about the data exploitation/error calculation?

Subsection 6.1.2 delivers additional information about the data exploitation and, thus, was moved to Sect. 5.1 (Sect. 3.1.2 in the revised manuscript).

R#1-15) Table 2: Why is the uncertainty of the albedo of the landfill not considered here?

Uncertainty of the albedo was added to Table 2. See also comment to R#1-9.

R#1-16) P23 L25: Why/How was the pseudo-surface concentration enhancement range determined to be 50%-150% of the lowest flight track?

One does actually not know the surface concentrations without measuring them. They can depend on, e.g., the type of source, emission height, atmospheric conditions (stability), and surface terrain.

For our baseline, we choose a vertically homogenous distribution of the concentration below the lowest flight track (corresponds to 'pseudo surface track has the same concentrations as measured at the lowest track'). The assumption of a vertically homogenously distributed plume was also chosen in a first order approximation in many studies in case only one flight track and transect, respectively, was available (e.g., Turnbull et al., 2011; Peischl et al., 2013; Karion2013). Additionally, these studies had no measurements at or near the boundary layer height, whereas in our study for the investigated landfill the upper plume limit is well confined.

But as shown in Fig. S9, the plume emitted by the landfill cannot be assumed to be well mixed, at least, at the altitudes (usually between 600 and 1200 m) sampled by the aircraft. Therefore, there is no reason to believe that the plume is well-mixed below the lowest flight track. We have tried to capture this effect by the error assessment using, in a first order approximation, a +-50% variation of the CH_4 enhancement, which was measured at the lowest flight track, at the surface. In extreme cases, the surface CH_4 enhancement could also be -100% or could exceed +100%. We believe that -100% is an unlikely scenario, because landfills are surface sources and CH_4 concentrations might increase towards the surface for those source types (Gordon et al., 2015). On the other hand, our measured in-situ walls were acquired some kilometres downwind of the landfill so that it is expected that some vertical mixing had occurred suppressing very high accumulations of CH_4 at the surface.

The missing measurements of surface concentrations can be a large source of uncertainty in terms of flux calculations. Our error estimate might be on the lower end. This disadvantage can be avoided by using remote sensing measurements, which probe the entire atmospheric column.

In order to achieve better estimates of the surface concentrations, one could combine large eddy simulations with the airborne measurements (as done by, e.g., Lavoie et al. 2015) but were out of scope for this work or one could simultaneously collect surface measurements by, e.g., car.
We adapted P23L19 – L23 to reflect these thoughts.

R#1-17) P24 L27: Why is the "comparison of emissions" not considered a result (sect. 6) or included in the conclusions (sect. 8), but discussed in an independent section?

Agreed. Section "Comparison of emissions" was merged with section "Results".

R#1-18) P24 following: Section 7 is called "comparison of emissions" – yet subsection 7.2 compares CH4 concentration results only.

Agreed. Section "Comparison of emissions" was removed and merged with section "Results" (see also comment R#1-17).

R#1-19) P25 L16: Is the reported average absolute difference statistically significant?

We changed the term "average absolute difference" to "average of the absolute differences" to not confuse the reader with the also existing term "mean absolute difference (MAD)". We also added the corresponding uncertainty of 2.8 $ktCH_4yr^{-1}$ showing that the average of the absolute differences of 2.4 $ktCH_4yr^{-1}$ is statistically not significant. In this context, we also shortened this section, Sect. 7.1 (Sect. 4.4 in the revised manuscript), to account for better readability. The single emission rates, which had been given in this section, were removed because they can already be found in Table 2 in a more structured and comprehensive way. The average of the absolute differences is a sufficient and meaningful summary of the comparison between the emission rates based on in-situ and remote sensing data.

R#1-20) P27/P28: Please consider adding a discussion on the implications of the ability of the suggested observational techniques given that only 1 out of 4 landfills could be studied within COMEX.

We added a dedicated section in the "Results" section (Sect. 4.7 in the revised manuscript) and in the supplementary material (Sect. S8), which investigate possible causes for not measuring CH_4 enhancements at the other landfills with the MAMAP remote sensing instrument (also see R#1-3).

For that we performed Observation System Simulation Experiments (OSSEs), which are based on Gaussian plume forward model simulations. These simulations incorporate atmospheric conditions like wind speed and wind direction but also consider instrumental characteristics like the MAMAP single measurement precision, ground scene size and the respective flight track. Based on a comparison of simulations and actual measurements it can be investigated whether the reported emission rates by EPA for the three other landfills were below the detection limit of the MAMAP remote sensing instrument or should actually have been detected in the MAMAP measurements for the given days, atmospheric conditions and instrumental and flight characteristics.

The results of this investigation have revealed that the reported emission rate for the Puente Hills Landfill (5.0 $ktCH_4yr^{-1}$) might be below the detection limit of the MAMAP remote sensing instrument for the given day, atmospheric conditions and instrumental characteristics.

On the other hand, based on the simulations, the emissions of the BKK Landfill (15.1 $ktCH_4yr^{-1}$) and the Scholl Canyon Landfill (5.9 $ktCH_4yr^{-1}$) should likely have been visible in the MAMAP remote

sensing measurements. This indicates that the actual emission rates for these landfills for the time of the overflight might have been lower than reported by EPA.

R#1-21) Especially - P28 L28f: Please expand on the claim that the observations are well suited to estimate CH4 emissions from larger landfills (see general comments). The uncertainties of the in-situ estimates you report are smaller than the uncertainties for the remote-sensing estimates and you can only detect stable plumes for 1 out of 4 landfills.

We expanded and relativized, respectively, our claim that remote sensing measurements are well suited for measuring landfills based on the previous discussions in R#1-3, R1-20 and R#1-16 (P28L28ff).

References

Gordon, M., Li, S.-M., Staebler, R., Darlington, A., Hayden, K., O'Brien, J., and Wolde, M.: Determining air pollutant emission rates based on mass balance using airborne measurement data over the Alberta oil sands operations, Atmospheric Measurement Techniques, 8, 3745–3765, doi:10.5194/amt-8-3745-2015, http://www.atmos-meas-tech.net/8/3745/2015/, 2015.

Karion, A., Sweeney, C., Pétron, G., Frost, G., Hardesty, R. M., Kofler, J., Miller, B. R., Newberger, T., Wolter, S., Banta, R., Brewer, A., Dlugokencky, E., Lang, P., Montzka, S. A., Schnell, R., Tans, P., Trainer, M., Zamora, R., and Conley, S.: Methane emissions estimate from airborne measurements over a western United States natural gas field, Geophysical Research Letters, 40, 4393–4397, doi:10.1002/grl.50811, 2013.

Kirschke, S., Bousquet, P., Ciais, P., Saunois, M., Canadell, J., Dlugokencky, E., Bergamaschi, P., Bergmann, D., Blake, D., Bruhwiler, L., Cameron-Smith, P., Castaldi, S., Chevallier, F., Feng, L., Fraser, A., Heimann, M., Hodson, E., Houweling, S., Josse, B., Fraser, P., Krummel, P., Lamarque, J.-F., Langenfelds, R., Le Quere, C., Naik, V., O'Doherty, S., Palmer, P., Pison, I., Plummer, D., Poulter, B., Prinn, R., Rigby, M., Ringeval, B., Santini, M., Schmidt, M., Shindell, D., Simpson, I., Spahni, R., Steele, L., Strode, S., Sudo, K., Szopa, S., Van Der Werf, G., Voulgarakis, A., Van Weele, M., Weiss, R., Williams, J., and Zeng, G.: Three decades of global methane sources and sinks, Nature Geoscience, 6, 813–823, doi:10.1038/ngeo1955, 2013.

Krings, T., Gerilowski, K., Buchwitz, M., Hartmann, J., Sachs, T., Erzinger, J., Burrows, J. P., and Bovensmann, H.: Quantification of methane emission rates from coal mine ventilation shafts using airborne remote sensing data, Atmospheric Measurement Techniques, 6, 151–166, doi:10.5194/amt-6-151-2013, 2013.

Lavoie, T. N., Shepson, P. B., Cambaliza, M. O. L., Stirm, B. H., Karion, A., Sweeney, C., Yacovitch, T. I., Herndon, S. C., Lan, X., and Lyon, D.: Aircraft-Based Measurements of Point Source Methane Emissions in the Barnett Shale Basin, Environmental Science & Technology, 49, 7904–7913, doi:10.1021/acs.est.5b00410, 2015.

Peischl, J., Ryerson, T. B., Brioude, J., Aikin, K. C., Andrews, A. E., Atlas, E., Blake, D., Daube, B. C., de Gouw, J. A., Dlugokencky, E., Frost, G. J., Gentner, D. R., Gilman, J. B., Goldstein, A. H., Harley, R. A., Holloway, J. S., Kofler, J., Kuster, W. C., Lang, P. M., Novelli, P. C., Santoni, G. W., Trainer, M., Wofsy, S. C., and Parrish, D. D.: Quantifying sources of methane using light alkanes in the Los Angeles basin, California, Journal of Geophysical Research: Atmospheres, 118, 4974–4990, doi:10.1002/jgrd.50413, 2013.

Saunois, M., Bousquet, P., Poulter, B., Peregon, A., Ciais, P., Canadell, J. G., Dlugokencky, E. J., Etiope, G., Bastviken, D., Houweling, S., Janssens-Maenhout, G., Tubiello, F. N., Castaldi, S., Jackson, R. B., Alexe, M., Arora, V. K., Beerling, D. J., Bergamaschi, P., Blake, D. R., Brailsford, G., Brovkin, V., Bruhwiler, L., Crevoisier, C., Crill, P., Covey, K., Curry, C., Frankenberg, C., Gedney, N., Hoeglund-Isaksson, L., Ishizawa, M., Ito, A., Joos, F., Kim, H.-S., Kleinen, T., Krummel, P., Lamarque, J.-F., Langenfelds, R., Locatelli, R., Machida, T., Maksyutov, S., McDonald, K. C., Marshall, J., Melton, J. R., Morino, I., Naik, V., O'Doherty, S., Parmentier, F.-J. W., Patra, P. K., Peng, C., Peng, S., Peters, G. P., Pison, I., Prigent, C., Prinn, R., Ramonet, M., Riley, W. J., Saito, M., Santini, M., Schroeder, R., Simpson, I. J., Spahni, R., Steele, P., Takizawa, A., Thornton, B. F., Tian, H., Tohjima, Y., Viovy, N., Voulgarakis, A., van Weele, M., van der Werf, G. R., Weiss, R., Wiedinmyer, C., Wilton, D. J., Wiltshire, A., Worthy, D., Wunch, D., Xu, X., Yoshida, Y., Zhang, B., Zhang, Z., and Zhu, Q.: The global methane budget 2000 - 2012, Earth System Science Data, 8, 697–751, doi:10.5194/essd-8-697-2016, http://dx.doi.org/10.5194/essd-8-697-2016, 2016.

Turnbull, J. C., Karion, A., Fischer, M. L., Faloona, I., Guilderson, T., Lehman, S. J., Miller, B. R., Miller, J. B., Montzka, S., Sherwood, T., Saripalli, S., Sweeney, C., and Tans, P. P.: Assessment of fossil fuel carbon dioxide and other anthropogenic trace gas emissions from airborne measurements over Sacramento, California in spring 2009, Atmospheric Chemistry and Physics, 11, 705–721, doi:10.5194/acp-11-705-2011, http://dx.doi.org/10.5194/acp-11-705-2011, 2011.

Methane emissions from a Californian landfill, determined from airborne remote sensing and in-situ measurements

Sven Krautwurst[1], Konstantin Gerilowski[1], Haflidi H. Jonsson[2], David R. Thompson[3], Richard W. Kolyer[4], Laura T. Iraci[4], Andrew K. Thorpe[3], Markus Horstjann[1], Michael Eastwood[3], Ira Leifer[5], Sam Vigil[6], Thomas Krings[1], Jakob Borchardt[1], Michael Buchwitz[1], Matthew M. Fladeland[4], John P. Burrows[1], and Heinrich Bovensmann[1]

[1]Institute of Environmental Physics (IUP), University of Bremen, Bremen, Germany
[2]Center for Interdisciplinary Remotely-Piloted Aircraft Studies (CIRPAS), Marina, CA, US
[3]Jet Propulsion Laboratory (JPL), California Institute of Technology (Caltech), Pasadena, CA, US
[4]Earth Science Devision, NASA Ames Research Center (ARC), Mountain View, CA, US
[5]Bubbleology Research International (BRI), Goleta, CA, US
[6]California Polytechnic State University (CalPoly), San Luis Obispo, CA, US

Correspondence to: Sven Krautwurst (krautwurst@iup.physik.uni-bremen.de)

Abstract. Fugitive emissions from waste disposal sites are important anthropogenic sources of the greenhouse gas methane (CH_4). As a result of the growing world population and the recognition of the need to control greenhouse gas emissions, this anthropogenic source of CH_4 has received much recent attention. However, the accurate assessment of the CH_4 emissions from landfills by modeling and existing measurement techniques is challenging. This is because of inaccurate knowledge of the model parameters and the extent of and limited accessibility to landfill sites. This results in a large uncertainty in our knowledge of the emissions of CH_4 from landfills and waste management.

In this study, we present results derived from data collected during the research campaign COMEX (CO_2 and Methane EXperiement) in late summer 2014 in the Los Angeles (LA) Basin. ~~The~~ One objective of COMEX, which comprised aircraft observations of methane by the remote sensing Methane Airborne MAPper (MAMAP) instrument and a Picarro greenhouse gas in-situ analyser, was the quantitative investigation of CH_4 emissions.

Enhanced CH_4 concentrations or „CH_4 plumes“ were detected downwind of landfills by remote sensing aircraft surveys. Subsequent to each remote sensing survey, the detected plume was sampled within the atmospheric boundary layer by in-situ measurements of atmospheric parameters such as wind information and dry gas mixing ratios of CH_4 and carbon dioxide (CO_2) from the same aircraft. This was undertaken to facilitate the independent estimation of the surface fluxes for the validation of the remote sensing estimates.

During the COMEX campaign, four landfills in the LA Basin were surveyed. One landfill ~~has repeatedly shown~~ repeatedly showed a clear emission plume. This landfill, the Olinda Alpha Landfill, was ~~observed~~ investigated on four days during the last week of August and first days of September 2014. Emissions were estimated for all days using a mass balance approach. The derived emissions ~~are between 13.0 and 18.2~~vary between 11.6 and 17.8 $\mathrm{kt\,CH_4\,yr^{-1}}$ with related uncertainties in the range of ~~17~~14 % to ~~46~~45 %. The comparison of the remote sensing and in-situ based CH_4 emission rate estimates reveals good agreement within the error bars with an average ~~absolute difference of around 2.3~~of the absolute differences of

around 2.4 kt CH_4 yr^{-1} ($\pm$2.8 kt CH_4 yr^{-1}). The US Environmental Protection Agency (EPA) reported inventory value is 11.5 kt CH_4 yr^{-1} ~~in~~ for 2014, on average ~~3.0~~2.8 kt CH_4 yr^{-1} ($\pm$ ~~1.5~~1.6 kt CH_4 yr^{-1}) lower than our estimates acquired in the afternoon in late Summer 2014. This difference may in part be explained by a possible leak located on the south-western slope of the landfill, which we identified in the observations of the Airborne Visible / Infrared Imaging Spectrometer - Next Generation (AVIRIS-NG) instrument, flown contemporaneously aboard a second aircraft on one day.

1 Introduction

Methane (CH_4) is one of the most important anthropogenic greenhouse gases modulated by human activity. According to ~~Kirschke et al. (2013)~~Saunois et al. (2016), the methane emissions from landfills and waste management contribute ~~around 20~~with around 15 % to ~~27~~18 % [1] ~~of~~ to the global anthropogenic methane emissions budget. Under anaerobic conditions, bacteria produce CH_4 by consuming biodegradable waste, which has been deposited within the landfill. This is known as landfill gas (LFG), which contains CH_4 as its major component (typically between 50 % to 60 %), carbon dioxide (CO_2) and other gases (e.g., Eklund et al., 1998; Amini et al., 2012).

Modern landfills (NSWMA, 2006) are often covered with special oxidation layers and are also equipped with tubes embedded vertically and / or horizontally within the landfill, through which the LFG is collected. The collected LFG is often used (and converted to CO_2) in small dedicated power plants for electricity and heat generation and, thus, reduces the environmental impact of the landfill emissions. When not used for power generation, collected LFG is sometimes flared, which also oxidises CH_4 to CO_2 having a lower global warming potential (Myhre et al., 2013).

Nevertheless, not all of the CH_4 is captured by the LFG collection system and subsequently converted to CO_2. The amount of the remaining CH_4 escaping into the atmosphere depends on the engineering approaches used to manage the landfill and atmospheric boundary layer conditions. For instance, the type and material of the landfill cover can decrease (Trapani et al., 2013) or increase emissions (Capaccioni et al., 2011). Trapani et al. (2013) have also found that slopes of landfills are areas with an enhanced CH_4 release. Additionally, atmospheric pressure variations (Czepiel et al., 2003; Poulsen et al., 2003; Gebert and Groengroeft, 2006; Trapani et al., 2013; Xu et al., 2014) or surface wind speeds (Poulsen and Moldrup, 2006) can modulate CH_4 emissions into the atmosphere.

Both measurements of CH_4 and models of the processes producing CH_4 in landfill sites can be used to estimate their emissions. Commonly used for reporting and recommended by IPCC (2006) are first-order decay (FOD) waste models. They are based on knowledge of the amount of available degradable waste, which is consumed by the bacteria, how it decays over time, but also consider other parameters such as the type and age of the waste, its temperature, moisture content and oxidation capacity of the landfill cover (Amini et al., 2013). Studies comparing direct measurements to model estimates ~~have~~ found that the modeled outputs can significantly differ from actual measurements (Amini et al., 2012, 2013).

However, measurements are also challenging because landfills typically have a relatively large surface area (up to some square kilometres), an irregular topography and the emissions are not distributed homogeneously across the landfill. Babilotte

[1] ~~, last access: 29.09.2016~~

et al. (2010) compared five different techniques measuring emissions from the same landfill. The study included ground based in-situ (tracer gas method, inverse modeling of direct CH_4 measurements), ground based remote sensing (laser plume mapping, differential absorption light detection and ranging), and an airborne based method (helicopter-borne infrared laser spectroscopy at around 1.65 µm). The CH_4 emission rate estimates of the landfill under consideration and of a controlled release experiment performed in that study ~~disagreed~~ disagree by a factor of 5 to 10.

Several other studies used airborne based in-situ measurements to characterize the total emissions of landfills (e.g., Peischl et al., 2013; Lavoie et al., 2015, and references therein). In these studies different flight strategies and mass balance approaches were used. Emission uncertainties are typically estimated to be between approximately 20 % and 30 %. However, airborne in-situ measurements are often restricted by Air Traffic Control (ATC) regulations such as minimum safe altitude and ATC control zones.

Recently, airborne thermal-infrared (TIR, 7.5 to 13.5 µm) imaging spectrometry measurements ~~have been~~ were tested to locate CH_4 emissions also from landfills (Tratt et al., 2014). The study succeeded to derive emission rates for two localized on-site emitters - a compressed natural gas (CNG) fueling station and a gas-flaring station - with relative errors of 50 % and 120 %. However, integrated emissions for the entire landfill ~~were~~ are not reported.

In this manuscript, we present a data set collected by two different techniques i.e. passive airborne remote sensing and airborne in-situ cavity ring down spectroscopy (CRDS). They were used to investigate the ability of remote-sensing measurements to determine emission rates and to independently estimate the emission rate of a particular landfill in the Los Angeles (LA) Basin on four different days in late summer 2014. The passive airborne remote sensing method is based on medium spectral resolution (~0.9 nm) solar absorption spectroscopy in the short wave infrared (SWIR) region around 1.65 µm. To assess ~~the~~ total CH_4 landfill emissions, a mass balance approach ~~is~~ was used. The emission estimates, derived by this method, ~~are~~ were compared to emission estimates calculated using airborne in-situ measurements acquired from the same aircraft. Emissions ~~are~~ were estimated using a Kriging method for interpolation of the data in combination with a mass balance approach (in a similar way as described in, e.g., Lavoie et al., 2015, and references therein). In addition, imaging spectroscopy observations from another passive remote sensing instrument installed aboard ~~of~~ a second aircraft were utilized to identify emission hotspots across the landfill by analysing measured spectra in the region around 2.3 µm at low spectral resolution (~5 nm).

This article is structured as follows: ~~After describing the research campaign in which the flights where embedded, the selected target is introduced in Sect. ??. In Sect. ??, the~~ Section 2 introduces the investigated targets, participating instruments and ~~collected data sets are summarized. In Sect. ??, the flight strategy is presented~~the applied flight strategy. The retrieval methods are described in Sect. 3. In Sect. 4, the ~~emission rate results~~ main results of this study are presented. This includes the estimated emission rates, their errors~~and~~ , the retrieval results from the imaging instrument aboard the second aircraft ~~are reported. A comparison of the results from the different instruments is presented in Sect. ??.~~ and also comparisons between the instruments and reported inventory estimates. The manuscript closes with a summary and conclusions (Sect. 5).

2 ~~Campaign and target description~~Measurements

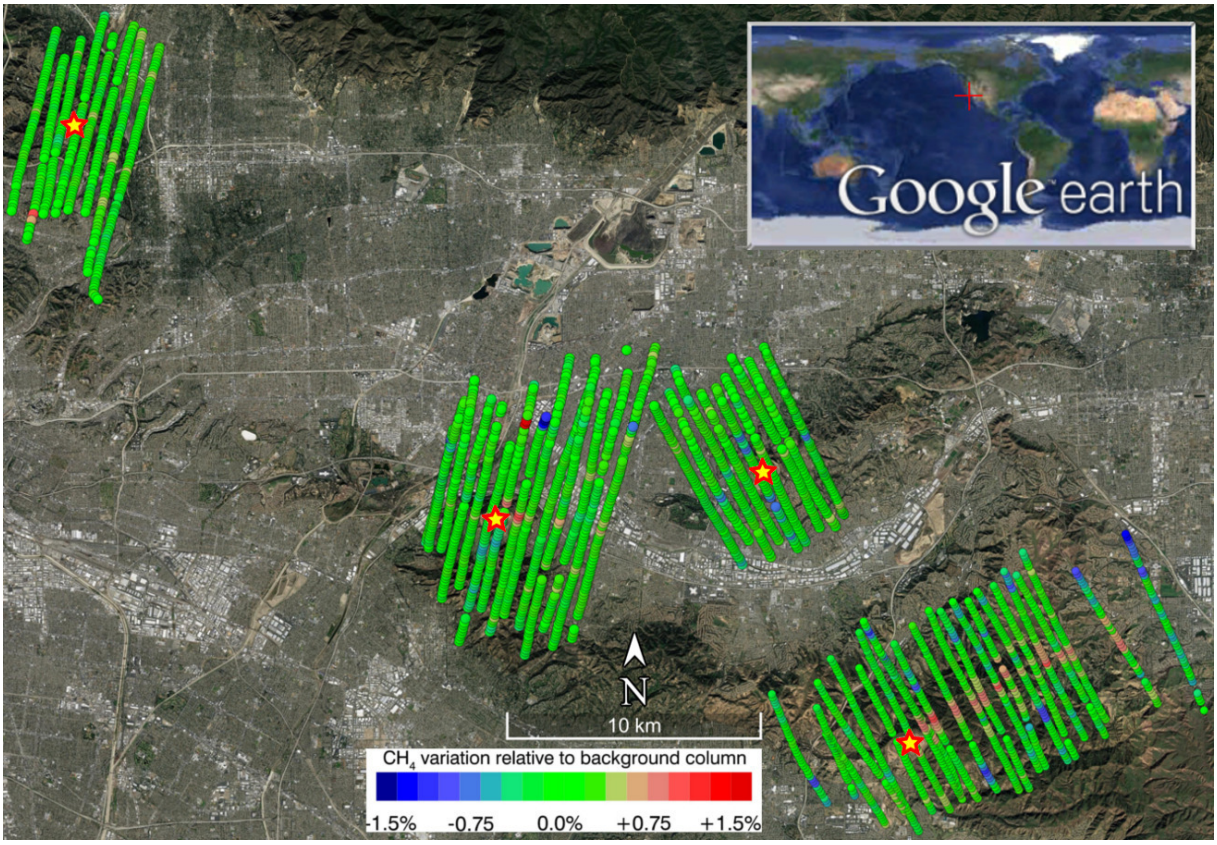

Figure 1. Shown are the MAMAP remote sensing survey flights over the four landfills (from left to right: the Scholl Canyon Landfill (SCL) on 27.08.2014, the Puente Hills Landfill (PHL) on 27.08.~~2017~~.2014, the BKK Corporation Landfill (BKK) on 01.09.2014 and the Olinda Alpha Landfill (OAL) on 01.09.2014) situated in the Los Angeles Basin (red cross in the world map, top right)~~in the main overview plot~~. ~~Their~~ The locations of the landfills are marked by red/yellow stars. The MAMAP measurements are filtered by inclination to remove the turns and the colour code depicts CH_4 variations relative to the background (for details, see Sect. 3.1). Only the Olinda Alpha Landfill shows a clear plume in downwind direction. The wind direction was in general from south-west during the measurements. The map underneath is provided by Google Earth.

This section gives a short description of the research campaign in which the measurement flights were embedded and the examined targets (Sect. 2.1). In Sect. 2.1, the participating instruments and collected data sets are summarized. Section 2.1 presents the flight strategy, which was used surveying the emission sources.

2.1 Campaign and target description

The measurement flights presented in this work were part of the CO_2 and Methane EXperiment (COMEX), which was conducted in the San Joaquin Valley (SJV) and greater Los Angeles in May/June and August/September 2014. COMEX was a collaborative effort between the National Aeronautics and Space Administration (NASA) and the European Space Agency

(ESA), in support of the development of the two satellite concept missions HyspIRI (Lee et al., 2015) and CarbonSat (Bovensmann et al., 2010; Buchwitz et al., 2013; ESA, 2015). ~~The main~~ One focus of the campaign addressed the assessment of anthropogenic CH_4 emissions. In addition to measurements over and in the plumes of landfills, flights were ~~made~~ conducted to determine emissions from oil fields (Thompson et al., 2015; Gerilowski et al., 2014), offshore seep fields and animal husbandry.

In total four different landfills were surveyed in the greater LA area: the Scholl Canyon Landfill (SCL), the Puente Hills Landfill (PHL), the BKK Corporation Landfill (BKK) and the Olinda Alpha Landfill ~~. Only the latter showed continuously~~ (OAL). According to the US Environmental Protection Agency[1] (EPA), the yearly expected CH_4 emissions of these landfills were 5.0 $\mathrm{kt\ CH_4\ yr^{-1}}$ (PHL), 5.9 $\mathrm{kt\ CH_4\ yr^{-1}}$ (SCL), 11.5 $\mathrm{kt\ CH_4\ yr^{-1}}$ (OAL) and 15.1 $\mathrm{kt\ CH_4\ yr^{-1}}$ (BKK) in 2014 (further details on the reported emission rates can be found in Sect. S9 in the supplementary material). During remote sensing surveys only the Olinda Alpha Landfill continuously showed detectable and well-developed plume structures~~during~~, which were well-suited for inversion of emission rates. The other landfills exhibited either much less pronounced measured enhancements (PHL) or no detectable enhancements in the remote sensing ~~surveys (~~data at all (SCL and BKK, compare to Fig. 1).

~~In this manuscript, we therefore~~ As this study investigates the use and ability of remote-sensing measurements in the SWIR region to determine emission rates, we focus on the ~~datasets~~ data sets collected over the Olinda Alpha ~~Municipal Landfill . All~~ Landfill in the remaining manuscript. The OAL data sets were also the most comprehensive ones allowing for comparisons of emission rates on four different days. A discussion regarding the three other landfills is given in Sect. 4.4.

Concerning the Olinda Alpha Landfill, all measurements showed a pronounced CH_4 plume over the investigated time period. The landfill is located in Orange County, Los Angeles Basin, CA, USA (at 33.939° N, 117.836° W; Fig. 2). Measurements were acquired on four different days in the middle of the afternoon, during the last week of August and the first days of September 2014. On flight days, skies were clear and winds were from south-west to west at around 4 to 8 $\mathrm{m\ s^{-1}}$.

The Olinda Alpha Landfill started operation in 1960 and is expected to close by 2030. It accepts a maximum of 8,000 tons of municipal solid waste daily and occupies an area of around 2.3 $\mathrm{km^2}$, whereas 1.7 $\mathrm{km^2}$ are used for waste disposal. Since 2012, a 32.5 MW combined cycle power plant has been using the LFG to generate electricity for around 22,000 homes[2]. According to ~~the US Environmental Protection Agency[3] (EPA)~~EPA, the estimated CH_4 amount released into the atmosphere was 11.5$\mathrm{kt\ CH_4\ yr^{-1}}$ in 2014 dropping from a peak value of 15.4 $\mathrm{kt\ CH_4\ yr^{-1}}$ in 2011 to 14.3 $\mathrm{kt\ CH_4\ yr^{-1}}$ in 2013.

3 ~~Aircraft instrumentation and collected data sets~~

2.1 Aircraft instrumentation and collected data sets

All instruments used for a quantitative analysis were flown aboard a DHC-6 Twin Otter (TO) aircraft operated by the Center for Interdisciplinary Remotely-Piloted Aircraft Studies (CIRPAS[3]). These comprise: the Methane Airborne MAPper (MAMAP),

[1] https://ghgdata.epa.gov/ghgp/main.do#/facility/, last access: 10.05.2017

[2] http://oclandfills.com/landfill/active/olindalandfill, last access: 21.06.2016

[3] ~~, last access: 07.07.2016~~

[3] http://www.cirpas.org/, last access: 17.10~~.2017~~.2016

a Picarro ~~CDRS~~ CRDS greenhouse gas in-situ analyser, and the CIRPAS aircraft standard research instrumentation suite including different positioning and attitude, meteorological, aerosol, cloud and precipitation sensors.

The remote sensing instrument MAMAP (Gerilowski et al., 2011) was developed by the Institute of Environmental Physics (IUP), University of Bremen, in cooperation with the German Research Centre for Geoscience (GFZ) in Potsdam. It measures reflected and scattered solar radiation from the surface in the spectral region between 1.59 and 1.69 µm at medium spectral resolution of around 0.9 nm to retrieve total column concentration information of CH_4 and CO_2. In case of CH_4, the precision of the retrieved columns has been estimated to be better than 0.4 % over land surfaces (Krings et al., 2013). For the current flights, a fibre coupled entrance telescope (connecting the telescope via a 5 m glass fibre bundle to the spectrometer) was installed on a gyro stabilized platform (SOMAG, type: CSM-130[4]) to ensure nadir viewing geometry. The column information derived from MAMAP ~~is~~ was used in combination with knowledge of the wind fields for the calculation of emission rates.

The Picarro fast greenhouse gas in-situ analyser (type: G-2301f) was provided by the NASA's Ames Research Center (ARC) and operated by IUP during the flights. The instrument uses the CRDS technique (Crosson, 2008) to measure CH_4, CO_2 and water vapour (H_2O) in-situ concentrations at flight altitude at a frequency of around ~~1.7~~0.5 Hz. The flow rate of the installed external pump was around 165 standard cubic centimetres per minute (sccm) for altitudes between 600 and 1400 m above sea level (m asl). In combination with a cavity volume of around 4.7 cm^3 at standard temperature and pressure (STP, $T = 0$ °C, $p = 1013.15$ hPa), this led to a flushing time and refilling time, respectively, of the cell of around 1.8 s. This value is close to the actual measurement frequency of the instrument. The air samples entered the aircraft through an atmospheric in-situ sampling boom and then were transported via a PTFE tubing system to the measurement cavity of the CRDS instrument. This process ~~induces~~ induced a time delay (in the following referred to as time lag) between the position where the air samples ~~are~~ were acquired in the atmosphere and the time of measurement in the ~~ring down~~ ring-down cavity of the instrument ~~onboard~~ aboard the aircraft. This time lag was estimated from measurements in the laboratory to be around 21 s with an associated uncertainty ~~conservatively~~ estimated to be ±5 s. Dry gas mixing ratios of CH_4 and CO_2 were calculated by the software of the analyser via the synchronously measured water vapour ~~(Rella, 2010). These measurements are~~ (Rella et al., 2013, and references therein). The uncertainties of the dry gas mixing ratios of CH_4 and CO_2 have been estimated to be 2.3 ppb and 0.15 ppm, respectively, from laboratory experiments. The dry gas mixing ratios have also been assessed against known National Oceanic and Atmospheric Administrations (NOAA) standards. The resulting calibration factors for CH_4 (1.002275041) and CO_2 (1.004664623) were applied to correct the dry gas mixing ratios in advance to further analysis. These measurements were used for an independent in-situ based emission estimate. This ~~enables~~ enabled a comparison to be made with the emission estimated by the MAMAP remote sensing data.

The CIRPAS aircraft standard research instrumentation suite delivers auxiliary data. These comprise, for example, 3D position information (attitude, heading), wind information (speed and direction derived from a 5-hole turbulence probe), and information for the characterization of the atmosphere (e.g., potential temperature, aerosol load, ambient temperature, pressure) at a frequency of 10 or 1 Hz depending on the measured parameter.

[4]http://www.somag-ag.de/csm-130/, last access: 02.08.2016

On one flight day, the CIRPAS TO was accompanied by a second Twin Otter aircraft flying the Airborne Visible / Infrared Imaging Spectrometer - Next Generation ~~(AVIRIS-NG - Hamlin et al., 2011; Green et al., 1998)~~ (AVIRIS-NG; Green et al., 1998; Hamlin by the Jet Propulsion Laboratory (JPL). AVIRIS-NG also measures backscattered solar radiation from the surface to infer column information on CH_4. In contrast to MAMAP, AVIRIS-NG is an imaging instrument with a high spatial sampling but relatively low spectral resolution of 5 nm and a wide spectral range from 0.38 to 2.51 µm. Typical CH_4 retrievals use the spectral region from 2.1 to 2.4 µm. In this study, we ~~use~~ used the AVIRIS-NG instrument's imaging capabilities to identify potential source position(s) of CH_4 emitted by the landfill, which was not possible with the non-imaging MAMAP instrument (Thompson et al., 2015).

3 ~~Flight strategy~~

2.1 Flight strategy

To achieve the goal of estimating the emission rate of an areal source like a landfill (here: around ~~2.3~~1.7 km^2) using combined aircraft remote sensing and in-situ observations by the MAMAP and Picarro instruments, an appropriate flight pattern ~~needs~~ needed to be flown by the aircraft. The measurements during the flights were divided into two parts: 1) remote sensing measurements of the CH_4 plume from above the atmospheric boundary layer covering the entire area by a dense pattern and 2) in-situ measurements intersecting the entire plume within the atmospheric boundary layer.

The remote sensing and in-situ flight patterns implemented during the campaign were developed and optimized during preflight planning on the basis of the above requirements as well as taking into account the weather forecast, restrictions due to Air Traffic Control (ATC), and available flight time. Each acquisition started with remote sensing measurements and was followed by in-situ measurements.

Performing the remote sensing measurements first ~~has~~ had a significant advantage as a CH_4 real-time retrieval utilizing the MAMAP data ~~has~~ had been implemented for the COMEX campaign. ~~If~~ In case the real wind direction ~~deviates~~ deviated from the forecast, this approach ~~allows~~ allowed the operator to dynamically adjust the flight pattern accordingly to match the plume location obtained from the remote sensing total column information. The latter ~~is~~ was dynamically superimposed on Google Earth map data.

The remote sensing tracks ~~are flown typically~~ were typically flown above the atmospheric boundary layer in a dense pattern perpendicular to the wind direction covering the entire measurement area. In-situ CH_4 and CO_2 data were also acquired during these measurements providing information on CH_4 and CO_2 concentration distributions in the measurement area above the boundary layer.

To ensure a good coverage of the vertical extent of the plume during the second part of the flight focusing on in-situ measurements, the aircraft typically flew at a fixed distance from the source for several plume transects perpendicular to the prevailing wind direction at different altitudes trying to best cover the entire boundary layer. The number of legs for such a "wall" of measurements ~~varies~~ varied depending on the available flight time, between 3 and 6. Additionally, depending on available flight time such a wall was typically flown upwind and downwind characterizing the inflow and outflow to the

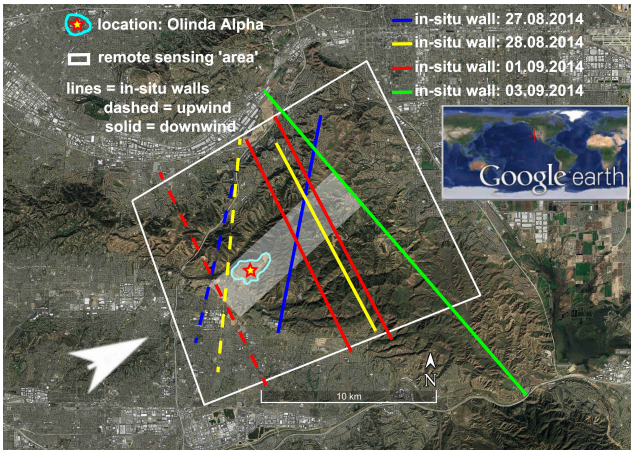

Figure 2. The Olinda Alpha Landfill is located at the position of the red/yellow star encircled by the cyan solid line. Additionally, the approximate positions of the flown in-situ upwind (dashed lines) and downwind (solid lines) walls (see Sect. ~~??~~ 2.1 for details) and the area which were surveyed by the MAMAP remote sensing instrument (white box) are shown. The colours of the in-situ walls represent the different flight days at the Olinda Alpha Landfill: Blue: 27.08.2014. Yellow: 28.08.2014. Red: 01.09.2014. Green: 03.09.2014. The white arrow indicates the approximate prevailing wind direction for measurement flights over the Olinda Alpha Landfill .The transparent white area aligned in the approximate wind direction shows one example flight track of the AVIRIS-NG imaging instrument abroad the second Twin Otter aircraft for illustration purposes. The map underneath is provided by Google Earth.

area. On one day, one additional downwind wall of measurements was located at a distance further away from the source to better characterize occurrent errors on the estimated fluxes. The maximum altitude extent of the plume ~~is~~ was generally well documented, as on all four flight days, there ~~is~~ was at least one leg, which shows no plume structures or signals at higher altitudes and therefore confines the upper limit of the plume. Due to ATC restrictions over congested areas like the Los Angeles Basin, flying below 1000 ft above ground level (ft agl, equals around 300 m agl) was not permitted. Therefore, the lowest measured track was typically extrapolated down to the surface following the terrain (more details are given in Sect. 4.2). Altitude changes were made not faster than 150 metres per minute to minimise the effect of pressure changes on the in-situ sampling. This rate of change maintained the sampling cavity conditions well within acceptable tolerances: i.e. Cavity pressure within 140.0 ± 0.04 Torr and cavity temperature within 45.0 ± 0.002 °C (deviations are given in ± 1-σ). Figure 2 shows the approximate position of the three upwind (dashed lines) and five downwind (solid lines) walls flown on all four days.

The flight pattern performed by the second aircraft with the imaging AVIRIS-NG instrument aboard was different. Due to its relatively wide swath, it needed only one flight line to cover the entire landfill. Measurements were acquired while flying well above the boundary layer approximately parallel to the prevailing wind direction.

3 Retrieval algorithms and calculation of emission rates

~~The following sections present~~ This section presents the steps necessary to obtain the emission rates from the measurements collected by the different instruments. Section 3.1 describes the MAMAP retrieval algorithm and the assessment of the emission rate estimates ~~.~~ including discussions of associated uncertainties (Sect. 3.1.1) and possible dependencies of the retrieved columns on the detector filling (Sect. 3.1.2). Section 3.2 explains how the in-situ data collected by the Picarro ~~instrument is~~ greenhouse gas in-situ analyser was used to determine emission rate estimates ~~.~~ and related uncertainties (Sect. 3.2.1). In addition, the retrieval of the CH_4 anomaly maps from the AVIRIS-NG imaging data is described in Sect. 3.3.

3.1 MAMAP retrieval algorithm and emission rate estimates

In order to retrieve the column amounts of CH_4 and CO_2 from the measured spectra, we used the Weighting Function Modified Differential Optical Absorption Spectroscopy (WFM-DOAS) method (for details, see Buchwitz et al., 2000; Krings et al., 2011, 2013). In general, the algorithm minimizes the differences between the logarithm of the measured spectra and a spectrum computed by a ~~linearised~~ Radiative Transfer Model (RTM), which describes the general or mean state of the atmosphere during the flight. The differences between the modelled and measured ~~parameters~~ spectra are minimized by varying selected parameters or fit factors on, e.g., the methane profile and atmospheric parameters. The CH_4 in the plume from landfill emissions is then seen to be enhanced relative to the surrounding air.

The WFM-DOAS algorithm has successfully been applied to aircraft MAMAP measurements and used to investigate the emissions of point sources at known locations having flue gas or ventilation stacks / chimneys with diameters of below 50 m, such as those from CO_2 emitting power plants (Krings et al., 2011, 2016) and CH_4 emitting ventilation shafts of coal mines (Krings et al., 2013). In contrast to the previous studies, we ~~apply~~ have applied the approach to an areal source i.e. a landfill (with a size of around ~~2.3~~1.7 km^2), where the exact locations of the emission(s) are not known but limited by the approximate area of the landfill. As a result of the larger area of this source and the resulting wider plume, the expected column enhancements within the plume are typically lower in comparison to enhancements produced by point sources with diameters smaller than 50 m having the same source magnitude for similar atmospheric conditions.

For each flight a dedicated set of RTM computations were calculated to account for the varying atmospheric conditions on the different days. Additionally, a change in the solar zenith angle (SZA) and surface elevation along the flight track ~~are~~ were taken into account by performing RTM simulations to generate a 2-dimensional look-up table, which ~~is~~ was then used in the retrieval. The surface elevation is based on data from the Shuttle Radar Topography Mission (SRTM) digital elevation model version 2.1[5] which has a spatial resolution of one arc second (around 30 m at the equator) in the U.S.A. Additionally, the remaining parameters flight altitude, surface albedo and atmospheric background profiles were also adapted to the current flight conditions:

- The surface ~~is~~ was assumed to have a Lambertian reflectance and for the spectral band of CH_4 and CO_2 to have no spectral dependency. The surface spectral reflectance or surface albedo values used ~~are~~ were taken from Chen et al. (2006). They ~~use~~ used clear-sky radiances measured by the Moderate Resolution Imaging Spectrometer (MODIS) onboard the

[5]http://dds.cr.usgs.gov/srtm/version2_1/, last access: 15.06.2016

Terra satellite and the Visible Infrared Scanner (VIRS) onboard the Tropical Rainfall Measuring Mission (TRMM) spacecraft to retrieve the surface albedo in different spectral channels for different surface type categories defined by the International Geosphere Biosphere Programme (IGBP). As the MAMAP instrument operates in the SWIR region around 1.65 µm, we ~~use~~ used the surface albedo derived from the 1.6 µm channel of MODIS and VIRS. Assuming that the surface type at and around the landfill can be described as a composite of approximately 50 % 'urban' and 50 % 'open shrubland' (corresponding to a retrieved surface ~~spectral reflectance or surface~~ albedo of around 0.22 and 0.40 (Chen et al., 2006, their Table 1), respectively), this yields a mean surface albedo of 0.31.

– For the background profiles of CH_4 and CO_2 (compare to Fig. S19 in the supplementary material), which describe the mean background concentrations of these gases in the measurement area (and are not influenced by, for example, the landfill emissions) the vertical profiles from the U.S. standard atmosphere were used and adapted to current concentrations by using data collected by the Picarro greenhouse gas in-situ analyser. The profiles of CH_4 and CO_2 in the lower part of the troposphere were replaced by a polynomial fitted to the measured profile corresponding to ~~the first descent from remote sensing altitude to the lowest possible~~ in-situ ~~flight leg~~measurements collected at the respective site. In-situ measurements gathered at remote sensing altitude ~~are~~ were assumed to belong to the free troposphere and, thus, were used to scale the entire upper part of the U.S. standard profiles.

The HITRAN 2012 spectroscopic database for line parameters (Rothman et al., 2013) and a standard OPAC (Optical Properties of Aerosols and Clouds) urban aerosol scenario (Krings et al., 2011, 2013, 2016) were used in the RTM calculations, as the landfill is located within Los Angeles Basin.

The column-averaged dry air mole fractions XCH_4, which ~~are later~~ were used in the estimation of the CH_4 emission rate, were retrieved utilising the $XCH_4(CO_2)$ proxy method. This assumes a spatially and temporally constant CO_2 background concentration in the measurement area during the time remote sensing measurements are taken. In contrast to Krings et al. (2013), where coal mine ventilation shafts emitted only CH_4 and no significant amounts of CO_2, this assumption is violated for the Olinda Alpha Landfill. For landfills, it is expected that the co-emitted CO_2 may have an influence on the obtained $XCH_4(CO_2)$ (or short XCH_4) columns when this proxy method is used. The impact is further investigated in Sect. 3.1.1.

The procedure to estimate the CH_4 emissions from the retrieved MAMAP XCH_4 data ~~comprises~~ comprised the following steps. The data ~~is~~ was first filtered by a signal filter to remove spectra with very low ~~signal~~ detector filling (less than 3000 counts) or spectra in saturation (as in Krings et al., 2011). Additionally, an inclination filter of $\pm 5°$ ~~is~~ was applied to eliminate measurements during aircraft turns or insufficient gyro stabilization by the CSM-130. Furthermore, the data obtained for each flight track ~~is~~ was normalised by data obtained at its edges / flanks outside the plume ~~(Krings et al., 2016)~~(similar to Krings et al., 2016). This step ~~is~~ was necessary to remove a possible constant offset from the data (see also Krings et al., 2011) and to account for potential horizontal CH_4 or CO_2 concentration gradients.

Based on these measured column-averaged dry air mole fractions, XCH_4 (or CH_4 variations relative to the background column), a flux corresponding to each track ~~is~~ was estimated by applying a mass balance approach (similar to that used in Krings et al., 2011, 2013, 2016):

$$F_{\mathrm{RS}} = f_{\mathrm{RS}} \cdot \frac{1}{n} \sum_{i}^{n} u_{\mathrm{perp},i} \sum_{j}^{k_i} V_{i,j} \cdot \Delta x_{i,j} \tag{1}$$

where n is the total number of flight tracks downwind of the landfill flown on a certain day, k_i is number of measurements of a certain flight track i, V is the retrieved CH_4 variation relative to the background column in $\mathrm{molec\,m^{-2}}$ of measurement j for track number i, $\Delta x_{i,j}$ is the length segment in m of a certain measurement j of track number i, $u_{\mathrm{perp},i}$ is the wind speed component perpendicular to the flight track i in $\mathrm{m\,s^{-1}}$, f_{RS} is a conversion factor including the mass per CH_4 molecule and the time conversion from s to yr ($8.398 \cdot 10^{-25}\,\mathrm{kt\,s\,molec^{-1}}$) in order to calculate the emission rate F_{RS} in $\mathrm{kt\,CH_4\,yr^{-1}}$ based on the MAMAP remote sensing measurements. The emission rate is given in $\mathrm{kt\,CH_4\,yr^{-1}}$ but is strictly speaking only valid for the time of the overflight.

As in previous studies, the required wind direction ~~is~~ was directly estimated from the measurements (observed plumes) themselves. The wind speed ~~is~~ was provided by the 5-hole turbulence probe of the CIRPAS instrumentation, whereas only wind measurements collected in the area of the plume are used. Further details of the definition of the plume area for the wind estimates are given in Sect. 4.2.

3.1.1 Uncertainties of estimated MAMAP remote sensing emission rates

The largest errors or uncertainties for the remote sensing based emission estimates originate from uncertainties of the wind parameters used (wind speed and direction), the chosen concentration background normalisation area, the track-to-track variability, the influence of CO_2 variations in terms of the applied $XCH_4(CO_2)$ proxy method and the used surface albedo in the RTM simulations. In the following, the methodology of how these uncertainties were quantified is discussed. The resulting uncertainties are then given in Sect. 4.1 together with the estimated emission rate estimates for the single days.

A wind speed error linearly propagates into the emission estimate (compare to Eq. 1). As the in-situ measurements of the 5-hole turbulence probe were utilized for the wind speed estimates, the accuracy of the probe was used as a first order approximation for an uncertainty estimate. The uncertainty of the turbulence probe wind speed data has been estimated to be $0.5\,\mathrm{m\,s^{-1}}$.

The wind direction enters the flux estimate via a cosine term by modifying the used perpendicular wind speed to each flight track. An error on the wind direction of $\pm 10°$ was assumed for the case when wind direction is derived from the measurements themselves.

The lateral positions used for the background normalisation area may also have an influence on the result. In order to test their impact on the final emission estimate, the limits were shifted towards or away from the center line by a certain distance. For this type of test, one needs to keep in mind that if the limits are too close to the plume, part of the plume signal may enter the area used for the background normalization leading to an underestimate of the emission. On the other hand, if the limits

are set too far away, there might be not sufficient measurements left to calculate a reliable concentration background. Thus, the limits were varied by ± 250 and ± 500 m and, additionally, the defined plume area was shifted as a whole by 250 and 500 m to the right and left with respect to the center line.

Additionally, we computed the statistical error contribution. This error source is referred to as track-to-track variability in the following. Based on the used downwind tracks, a standard deviation σ and from that the uncertainty of the mean, was calculated (for further details, see also Farrance and Frenkel, 2012).

For the remote sensing emission rate estimate, the $XCH_4(CO_2)$ columns, determined using the proxy method, were used. The proxy method assumes that CO_2 is equally distributed and did not change in the measured area during the flight. In general, any CO_2 enhancement would lead to a decline in the derived $XCH_4(CO_2)$. The influence of such a CO_2 anomaly on the emission rate estimate depends on its location. On the one hand, the CO_2 enhancements can be co-located to the CH_4 landfill plume for the case when the CO_2 is co-emitted. This will lead to an underestimation of the emission rate. On the other hand, if the CO_2 originates from outside the measurement area, the enhancement is not co-located to the CH_4 plume. This results in an under- or overestimation of the emission rate depending on the location and distribution of the CO_2 variations. To estimate the influence of a variable CO_2 concentration in the measurement area on the remote sensing emission rate estimates, integrated in-situ columns (IISCs, compare to Fig. 8) were derived for the measured in-situ walls (compare to Fig. 5, b). The in-situ CH_4 and CO_2 measurements were vertically integrated from the surface to the highest altitude of the in-situ wall. Subsequently, the two obtained IISCs for CH_4 and CO_2 were similarly treated as they would be in the MAMAP proxy approach. First, the CH_4 column was divided by the CO_2 column and then the track was background normalized by its edges. This results on the one hand in an $IISC_{CH_4}$ from the CH_4 enhancement only, which is not influenced by CO_2 variations, and on the other in an $IISC_{CH_4/CO_2}$ which considers CO_2 variations. To quantitatively estimate the influence of this offset on the final emission rate estimate, the emission through each in-situ based cross-section $IISC_{CH_4}$ and $IISC_{CH_4/CO_2}$ was calculated by using Eq. 1. The column enhancement V and the length segment Δx are given by Fig. 8, whereby the remaining parameters, especially the perpendicular wind speed, cancel out, because we are only investigating in the relative difference.

An error of a wrongly assumed surface albedo in the simulated RTM, which is used during the fit procedure, is expected to have only a small influence on the estimated emission rate because it is captured by a low order polynomial, which is used during the retrieval process (also compare to Krings et al., 2011). To investigate the influence of a wrongly assumed surface albedo, emission rates were also determined based on RTM simulations using albedos of 0.22 and 0.40 representing the pure 'urban' and 'open shrubland' scenarios, respectively.

The total uncertainties were calculated by root-sum-squaring the single uncertainties for each day with the underlying assumption that the error sources were not correlated. The resulting total uncertainties including the uncertainties in wind information, normalization area, track-to-track variability, CO_2 variations, and surface albedo of the remote sensing measurements are stated in Sect. 4.1.

3.1.2 Non-linearity and associated negative XCH_4 anomalies

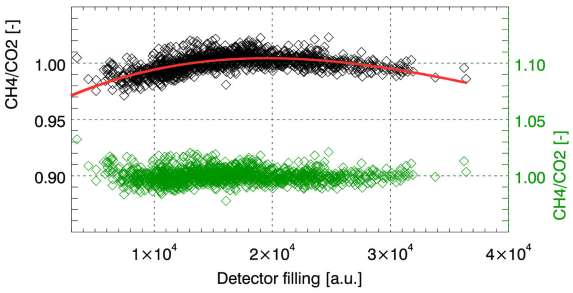

Figure 3. Scatter plot of the ratio of the retrieved CH_4 and CO_2 column over the maximum detector filling on the 01.09.2014. Black diamonds: Non-corrected data, left scale. Red solid line: Fitted 3^{rd} order polynomial. Green diamonds: Corrected data, right scale.

When investigating the retrieved normalised column-averaged dry air mole of CH_4 from the MAMAP remote sensing measurements on the 01.09.2014 (Fig. 6, a), they also show, besides a clear plume structure downwind of the landfill, some blue spots. First investigations have revealed some column dependencies on the detector filling. The scatter plot in Fig. 3 shows the ratio of the retrieved CH_4 and CO_2 profile scaling factors as a function of detector filling. It (black diamonds) clearly shows a decrease in the ratio for lower signals and also a less pronounced decrease for higher detector fillings. The cause of this dependency is still under investigation. The effect is most pronounced on the 01.09.2014 flight having the most measurements at lower detector fillings (e.g., 32 % below 13000 counts) with respect to the three other days (5 % on 27.08.2014, 12 % on 28.08.2014 and 2 % of the measurements on 27.08.2014). Therefore, the effect was further investigated exemplarily for the 01.09.2014.

In order to test the assumption that the negative $XCH_4(CO_2)$ anomalies originate from this signal dependency on the 01.09.2014, a 3^{rd} order polynomial (Fig. 3, red solid line) was fitted to the scattered data and subsequently used for correction. The new data set exhibits nearly no dependency on the detector filling (Fig. 3, green diamonds). Furthermore, the blue spots in Fig. 6 (b) are reduced compared to Fig. 6 (a). The 1-σ track-to-track variability has also been reduced by 26 %.

It is expected that this effect was less relevant for measurements from previous campaigns because the measured radiance signals and column enhancements were significantly higher than in this study. The mean estimated emission rate has furthermore changed by less than 2 % for the investigated Olinda Alpha Landfill measurements on the 01.09.2014 due to this effect and can therefore be neglected.

3.2 In-situ emission rate estimates by Picarro data

Fluxes from the Picarro data were estimated separately for each downwind wall by the procedure described below. An in-situ wall of measurements ~~comprises~~ comprised several flight legs flown at different altitudes. Usually these flight legs ~~are~~ were not aligned perfectly parallel to each other and separated by around 150 m in altitude. For interpretation and estimation of reliable emission rates, the in-situ measurements were projected on a well-defined plane and perpendicular surface and the

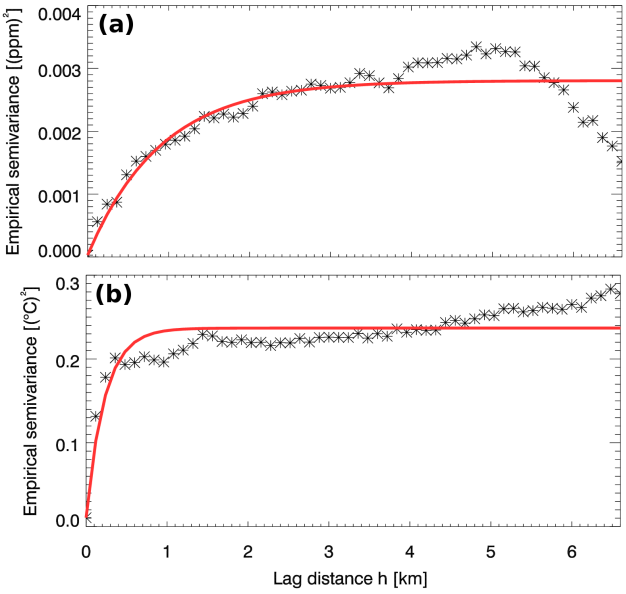

Figure 4. Example experimental semivariograms of (a) the in-situ dry gas mixing ratio of CH_4 and (b) the ambient temperature for the second downwind wall of the Olinda Alpha Landfill measurements on 01.09.2014. The black crosses depict the values of the empirical semivariance at certain lag distances h_j and the solid red line is the fitted exponential function. The fitted parameters of the exponential model are: Range: (a) ~~2.9~~2.7 km, (b) ~~0.9~~0.7 km; partial sill: (a) $2.8 \cdot 10^{-3}$ ppm^2, (b) ~~$2.4 \cdot 10^{-1}$~~$2.3 \cdot 10^{-1}$ °C^2; nugget: (a) ~~$4.9 \cdot 10^{-6}$~~$3.0 \cdot 10^{-5}$ ppm^2, (b) ~~$5.7 \cdot 10^{-3}$~~$1.1 \cdot 10^{-2}$ °C^2.

gaps between different tracks were filled by inter- and extrapolating, respectively, the measurements to a regular 2D grid on that plane.

Before the measurements from the flight legs of each wall were projected onto the plane surface, which is called ~~the~~ in-situ wall in the following, they were first corrected for the time lag of 21 s resulting from the tubing system (Sect. ~~??~~2.1). The approximate positions of those in-situ walls are drawn in Fig. 2. The projection of the CH_4 measurements is shown in Fig. 5 (a) for the first downwind wall on the 01.09.2014. Figure 5 further comprises (b) the interpolated CH_4 mixing ratios, (c) the background CH_4 mixing ratios and (d) the enhanced CH_4 mixing ratios attributed to the plume of the landfill resulting from the next processing steps described in the following.

For the inter- and extrapolation, the statistical Kriging method (Krige, 1951) was chosen. A similar approach ~~has also been~~ was also used in, e.g., Mays et al. (2009), Cambaliza et al. (2014) and Lavoie et al. (2015), to determine the outflow of cities and emissions of landfills. It is used to estimate values at locations, where no sample ~~had been~~ was measured (in our case, mostly between the projected flight legs), with the aid of statistical methods. This method is described by the three parameters nugget, sill and range, which describe the statistics of the data set. The nugget stands for the small scale variability, the sill is the variance and the range gives the distance at which the samples are not correlated any more.

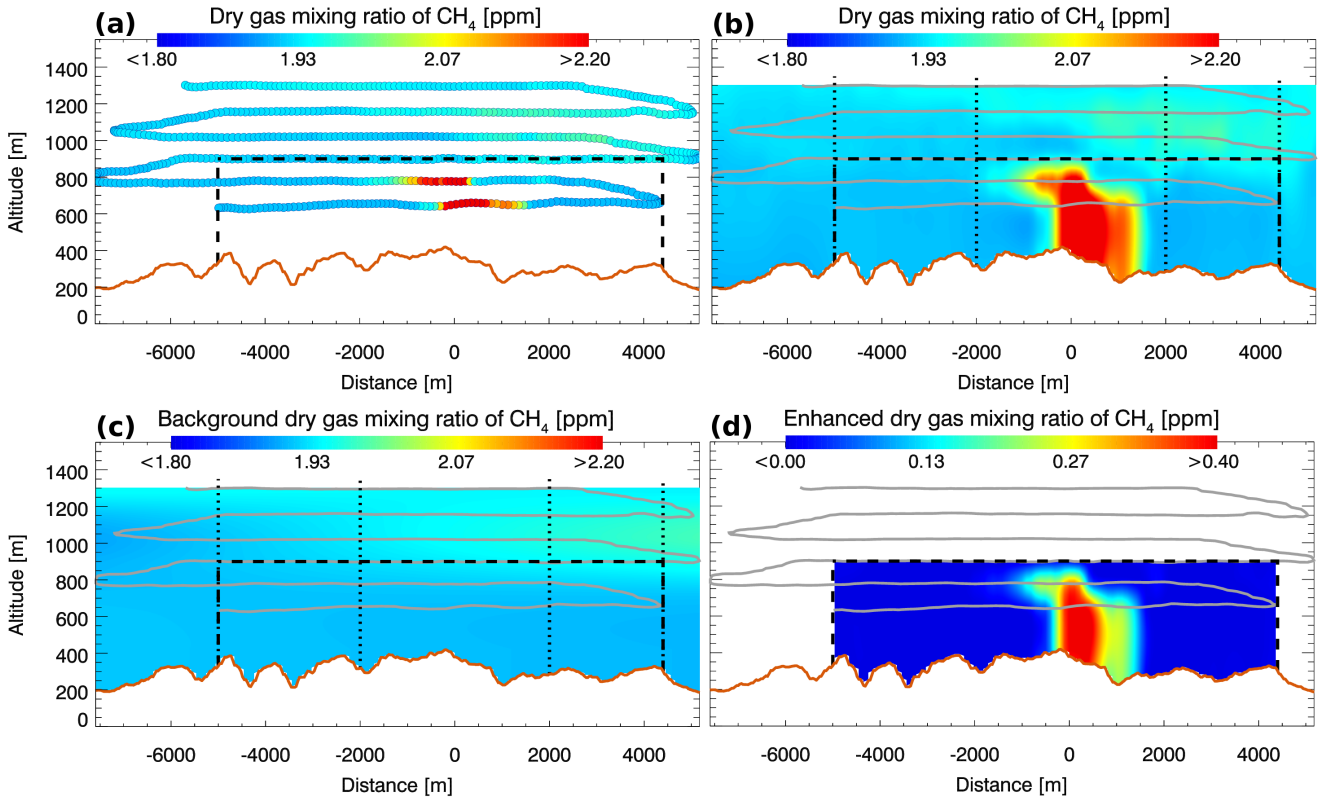

Figure 5. Example dry gas mixing ratios of CH_4 for the first downwind wall measured on the 01.09.2014 (middle in-situ wall in Fig. 6, solid red line). (a) Projected and time lag corrected mixing ratios acquired along the flight track onto the wall. (b) Kriged mixing ratios based on the measurements in (a) and an additionally added pseudo-track at the surface (not shown, see Sect. 4.2 for details). (c) Derived background mixing ratios from (b). (d) Derived CH_4 enhancement (kriged mixing ratios in (b) minus background mixing ratios in (c)). X-axis gives the distance from the approximate plume centre in m and y-axis gives the altitude in m above sea level (m asl). Solid orange lines depict the surface elevation (based on SRTM) and solid grey lines the projected flight track. Vertical dotted black lines show horizontal limits, which were used to define the background area (here: from -5.0 to -2.0 km and from +2.0 to +4.4 km). The area, which was used in the mass balance approach for estimating the emission rate, is enclosed by the dashed black lines.

All three parameters can be inferred from an experimental semivariogram (Fig. 4) calculated by the following equation (e.g., after Isaaks and Srivastave, 1989; Cressie, 1993; Caers, 2011):

$$y(h_j) = \frac{1}{2N(h_j)} \sum_{N(h_j)} \left[V(s_i) - V(s_i + h_j)\right]^2 \tag{2}$$

where h_j's are equidistant lag distances (e.g., ...360 m, ~~160~~480 m, ~~200~~600 m, ...) which are separated by a constant lag separation distance or bin width h_{sep} (e.g., ~~40~~120 m). The lag distance h_j describes the distance of the position between two measurements for which the semivariogram value $y(h_j)$ is calculated (Fig. 4, black crosses), whereby $N(h_j)$ is the number of data pairs for the respective lag distance h_j and the sum denotes the summation over all data pairs i which are separated by

a certain lag distance h_j. $V(s_i)$ and $V(s_i + h_j)$ are the parameter values at the positions (s_i) and $(s_i + h_j)$ separated by one specific lag distance h_j. For an irregularly spaced sample ~~also~~ either a lag tolerance is introduced ~~. That is, for a certain lag distance not only measurementsat exactly the distance~~ to consider also measurements, which are located in the approximate position of h_j ~~but at~~ , or the bin width itself is used meaning all measurements between h_j ~~± half the lag separation distance h_{sep}~~ and h_{j+1} are considered.

The experimental semivariogram was calculated for each wall and for each parameter by an IDL routine written by James McCreight from the University of Colorado in 2008[6] after the projected measurements of the corresponding parameter were detrended. In general, the semivariogram describes the correlation between different points at different distances.

To this experimental semivariogram, a commonly used exponential model function (e.g., after Isaaks and Srivastave, 1989) was fitted (Fig. 4, red solid line) which yields the necessary parameters range, nugget and (partial) sill:

$$model = nugget + partial\ sill \cdot \left[1 - e^{-\frac{3h}{range}}\right] \tag{3}$$

In this model, the value of the nugget is given by the value of the experimental semivariogram at the origin, the value of the sill corresponds to the sum of the nugget and the fitted parameter partial sill, and the range is defined as the lag distance h at which 95 % of the sill is achieved (Journel and Huijbregts, 1978).

The parameters from the exponential model ~~are~~ were used to estimate the value $V(s_0)$ of the paramters, e.g., the dry gas mixing ratio of CH_4, at a position s_0 where no measurement ~~was~~ had been acquired based on the measured surrounding values $V(s_i)$ at the positions s_i:

$$V(s_0) = \sum_{i=1}^{n} w_i \cdot V(s_i) \tag{4}$$

The influence of measured values $V(s_i)$ on the result is described by the respective weights w_i, whereas n is the total number of measurements. The weights are determined on basis of the above calculated parameters for the exponential model and the distances between the measured values and the unknown value, respectively (for further details, see Isaaks and Srivastave, 1989). Equation 4 ~~is~~ was evaluated for each grid point on the plane surface.

For computation, the Kriging procedure 'Krig_2D' from IDL 8.2.3 was used[7]. An example of such a kriged in-situ wall is shown in Fig. 5 (b) for CH_4 measurements of the first downwind wall on the 01.09.2014.

Subsequently, the mass transport of CH_4 through each wall ~~is~~ was estimated by a mass balance approach:

$$F_{IS} = \Delta z \cdot \Delta x \cdot f_{IS} \sum_i (c_i - c_{0,i}) \cdot \frac{p_i}{T_i \cdot k_B} \cdot u_{eff,i} \tag{5}$$

where i is the index representing the i^{th} grid box, c is the measured CH_4 concentration in $\mu mol\ mol^{-1}$ or ppm, c_0 is the CH_4 background concentration in $\mu mol\ mol^{-1}$ or ppm, p is the pressure in Pa, T the ambient temperature in K, k_B the Boltzmann constant, Δz and Δx are the vertical ~~(in altitude)~~ and horizontal extents of the grid boxes in m, respectively, f_{IS} is a conversion

[6] https://github.com/mccreigh/idl_variogram, last access: 06.07.2016

[7] http://www.harrisgeospatial.com/docs/krig2d.html, last access: 04.03.2016

factor having the same value and units as f_{RS} in Eq. 1 in order to retrieve the emission rate F_{IS} in $kt\,CH_4\,yr^{-1}$, and u_{eff} is the effective wind speed in $m\,s^{-1}$. The effective wind speed accounts for the wind speed normal to the plane surface and a geometry factor which considers the orientation of the wall relative to the orientation and flight direction of the aircraft, respectively, while a single measurement is recorded, and the wind direction. If the fitted wall is parallel to the measurement or perpendicular to the wind direction, the geometry factors becomes 1. The concentration c, the temperature T and the effective wind speed u_{eff} are based on Kriging, whereas the pressure $p = p(z)$ only depends on the altitude of the grid box i. The functional dependency $p(z)$ has been determined beforehand by fitting a linear function to the projected pressure measurements.

As indicated by Eq. 5, only the CH_4 enhancement above the background is needed. In order to separate the plume signal from the background, the plane surface of the CH_4 measurements ~~is~~ was segmented into a plume area and a background area (Fig. 5, ~~(b)~~b). For each altitude level, a linear function ~~is~~ was fitted to the CH_4 measurements in the background area by a least-squares approach. This yields a 2D-distribution of the CH_4 background for the specific in-situ wall (Fig. 5, ~~(c)~~c). Subtracting the achieved CH_4 background from the plane surface of the CH_4 measurements results in the pure CH_4 signal (Fig. 5, ~~(d)~~ d) originating from the source under consideration. This method accounts for possible concentration gradients in the CH_4 background in the horizontal and vertical direction.

3.2.1 Uncertainties of estimated Picarro in-situ emission rates

For the error budget of the in-situ based emission rates, two groups of error sources were identified: a) measurement related uncertainties and b) method related uncertainties. In the following, the main error sources are shortly discussed. A summary of all resulting errors for the different downwind walls is given in Table 2.

One main contributor to group a) is the wind information, which enters Eq. 5. It is based on measurements taken by the 5-hole turbulence probe of the CIRPAS instrumentation. Any error in the wind speed linearly propagates to the emission estimate. In a first order approximation, the accuracy of $0.5\,m\,s^{-1}$ of the turbulence probe was related to the averaged absolute wind speed of a downwind wall for estimating its influence on the estimated emission rate.

Another important error originates from the lack of measurements down to the surface. As baseline, it was assumed that the plume had been well-mixed in the lower part of the atmospheric boundary layer. On the one hand, CH_4 concentration might increase towards the surface because landfills are surface sources (Gordon et al., 2015). On the other hand, the in-situ walls were acquired some kilometres downwind of the landfill so that it is expected that some vertical mixing had occurred suppressing very high accumulations of CH_4 at the surface. To quantify these effects, it was assumed in a first order approximation that the pseudo-surface track used for extrapolation contains 50 or 150 % of the CH_4 enhancements with respect to the lowest observed flight track.

A third error source originates from the time lag, which was around 21 s. The estimated uncertainty of the time lag was 5 s. In order to assess the sensitivity of final emissions to a variation of the time lag, fluxes were estimated with time lags varying between 16 and 26 s.

Group b) consists of errors which originate e.g. from the chosen interpolation technique "Kriging" and how these data were used in the mass balance approach.

As discussed in the previous section, the Kriging method requires the three parameters nugget, (partial) sill and range, which were derived beforehand by fitting an exponential function to the experimental semivariogram for each quantity used in the mass balance approach. To quantify the influence of the Kriging parameters on the estimated emission and how sensitive it responds, the range was varied by a factor of 4 (i.e., -75 % and +300 %). Additionally, six configurations for the parameters nugget and partial sill (bearing in mind that the sill is the sum of partial sill and nugget) were investigated. On the one hand, the nugget was set to zero so that the partial sill equalled the sill and on the other hand, the nugget was increased to half of the sill and the partial sill was decreased to half of the sill. This was done for three different sills: the standard derived sill, two times the standard derived sill and half the standard derived sill. Furthermore, the effect of a varying lag separation distance, which also slightly influences the fitted parameters, is covered.

A further error source originates from the limits for the background area. To test its sensitivity, the limits were varied till their size had only 50 % of the original size.

The above mentioned error sources were combined for calculating a total uncertainty of the estimated emission rate for each downwind wall. For that, the errors were assumed to be independent and root-sum squared. The uncertainties for the four flight days are listed in Table 2.

3.3 Retrieval of CH_4 anomaly maps by AVIRIS-NG data

AVIRIS-NG methane retrievals use a matched filter approach previously demonstrated in campaigns at Kern River (Thompson et al., 2015), Four Corners (Frankenberg et al., 2016), and Aliso Canyon (Thompson et al., 2016). We treat AVIRIS-NG spectra $\boldsymbol{x}$ as Independent Identically Distributed (IID) instantiations of a multivariate Gaussian distribution with mean $\boldsymbol{\mu}$ and covariance matrix $\boldsymbol{\Sigma}$, written $\boldsymbol{x} \sim \mathcal{N}(\boldsymbol{\mu}, \boldsymbol{\Sigma})$. To account for the independent noise properties of each detector element, we model the spectra from each pushbroom element separately. This produces a slightly different distribution for every cross-track position. The covariance matrices are regularized to ensure accuracy and numerical stability for the limited number of samples. For each new spectrum, the matched filter estimates the magnitude α of a linear perturbation of this Gaussian distribution in the direction of the target signal. The estimate $\hat{\alpha}(\boldsymbol{x})$ is written:

$$\hat{\alpha}(\boldsymbol{x}) = \frac{(\boldsymbol{x} - \boldsymbol{\mu})^T \boldsymbol{\Sigma}^{-1} \boldsymbol{t}}{\boldsymbol{t}^T \boldsymbol{\Sigma}^{-1} \boldsymbol{t}} \tag{6}$$

Here the target is the radiance Jacobian with respect to a change in CH_4 absorption above background. The magnitude of the resulting estimate indicates the enhancement of CH_4 absorption above the local background in units of ppm $\times$ meters. After detection, the resulting maps ~~are~~ were georectified to permit direct comparison with MAMAP retrievals using synchronized IMU/GPS data and a local digital elevation model.

Table 1. Flight conditions and MAMAP remote sensing parameters for the four flights.

Flight day	27.08.2014	28.08.2014	01.09.2014	03.09~~.2114~~.2014
Flight time (local time)				
start [hh:mm]	14:11	14:21	14:55	13:27
end [hh:mm]	14:55	15:07	16:05	14:14
Solar zenith angle (SZA)				
min [°]	29.9	31.7	38.3	27.6
max [°]	37.0	39.3	51.3	32.6
Flight altitude [m]	1971	1627	1794	1945
Surface elevation along flight track				
min [m]	80	81	109	114
max [m]	437	435	483	496
Mean column mixing ratios				
CH_4 [ppb]	~~1744.5~~ 1748.4	~~1750.1~~ 1754.1	~~1807.3~~ 1811.4	~~1795.6~~1799.7
CO_2 [ppm]	~~396.8~~ 398.7	~~396.0~~ 397.8	~~391.7~~ 393.5	~~393.1~~394.9
Aerosol scenario [−]	urban	urban	urban	urban
Albedo [−]	0.31	0.31	0.31	0.31
Wind speed [$\mathrm{m\,s^{-1}}$]	6.3	~~8.2~~ 8.1	4.4	~~5.6~~5.5
Wind direction				
empirical (center line) [°]	236	240	241	240
in-situ [°]	~~238~~ 237	247	238	~~259~~249

4 Results and discussion

4.1 Emission rates from MAMAP remote sensing data

Remote sensing measurements over the Olinda Alpha Landfill were collected on four different days (27.08.2014, 28.08.2014, 01.09.2014, 03.09.2014) by the MAMAP remote sensing instrument. A detailed list of flight parameters, which were used for the radiative transfer model simulations using SCIATRAN (Rozanov et al., 2014) to generate the look-up table, are found in Table 1 for each day. For the emission rate estimates, only flight tracks located downwind of the landfill were used. The estimated emission rates as well as the corresponding uncertainties are summarised in Table 2. A detailed error discussion is given in Sects. 3.1.1 and 4.1.1.

~~For the emission rate estimates, only flight tracks located downwind of the landfill were used. A detailed error discussion is given in Sect. 3.1.1.~~

The flight altitude on the four days varied between 1630 and 1970 m asl, the surface elevation was around 300 m asl, the flight speed was around 60 $\mathrm{m\,s^{-1}}$ and the total measurement time per ground sample was around 0.8 s. The ground scene size

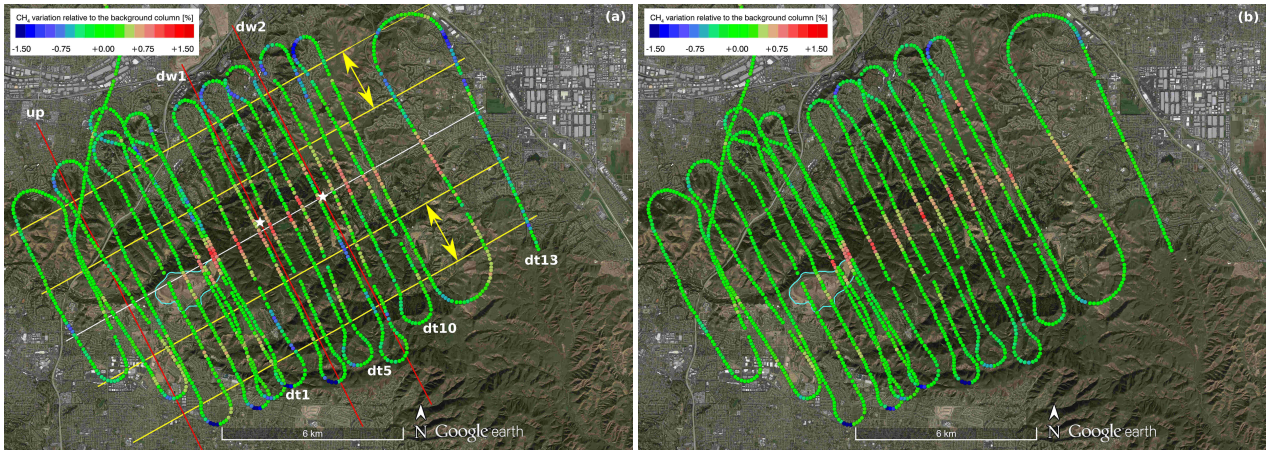

Figure 6. The complete MAMAP remote sensing flight pattern without the inclination filter over the Olinda Alpha Landfill (encircled by the cyan solid line) on 01.09.2014 is shown. The $XCH_4(CO_2)$ data is smoothed by a 3-point moving average and normalized by a 300-point moving average for visualisation purpose only. (a) For references, the positions of the center line (solid white line), the normalisation areas (area between the solid yellow lines emphasized by the yellow arrows), the three flown in-situ walls (solid red lines; upwind wall, up; first downwind wall, dw1; second downwind wall, dw2) and labels for the thirteen remote sensing downwind tracks (dt1 to dt13) are also depicted. The white stars emphasize the location of the approximate in-situ plume location, which corresponds to the origin used in Figs. 5, S7 (c-f) and S9 (c,d). (b) ~~Signal strength~~ Detector filling dependency corrected measurements (for details, see Sect. 3.1.2). The map underneath is provided by Google Earth.

for a general flight altitude of around 1800 m asl and this speed in combination with the surface elevation is approximately $69 \times 60\,\mathrm{m}^2$ (cross track $\times$ along track) for a focal length of the installed front optics of $f = 100\,mm$.

For the remote sensing measurements on the 01.09.2014, the wind direction was estimated to be 241° which is in good agreement with the in-situ based wind direction of 238° derived from in-situ measurements at the plume location of the second downwind wall (dw2 in Fig. 6, a, solid red line; for details of the definition of the plume location, see Sect. 4.2), which was flown directly after the remote sensing pattern. The wind speed was around $4.4\,\mathrm{m\,s^{-1}}$ determined over the same area as for the wind direction. An overview of the flight pattern and the measured CH_4 column enhancements is given in Fig. 6 (a). In addition to a clear plume signal observed up to 8 km downwind of the landfill, some CH_4 depletions are visible in the collected data. The origin of these negative CH_4 anomalies ~~will be further discussed~~ were investigated in Sect. 3.1.2.

For the emission retrieval, the area between -1750 and -4000 m (measurements south of the plume between the yellow lines in Fig. 6, ~~left~~a) and +1750 and +4000 m (measurements north of the plume between the yellow lines in Fig. 6, ~~left~~a) was used for background concentration normalization (also compare to Fig. 7, a). The mean emission rate estimate derived from Eq. 1 applied to the 13 downwind tracks (Fig. 7, a) is ~~13.9~~13.6 kt CH_4 yr^{-1}. The corresponding uncertainty is estimated to be 3.8 kt CH_4 yr^{-1} (or ±28 % of 13.6 kt CH_4 yr^{-1}).

The MAMAP measurements on 03.09.2014 were treated in a similar way as for the 01.09.2014 flight. The wind direction was 240° based on the empirical center line of the plume (measured in-situ wind direction is ~~259~~249°). The wind speed was ~~5.6~~5.5 $\mathrm{m\,s^{-1}}$. Figure S3 in the supplementary material shows the flight pattern and the CH_4 column enhancements.

In order to estimate the emission rate, the data was again filtered by the basic ~~signal strength~~ detector filling filter and by inclination. In contrast to the 01.09.2014, the area used for background normalization was set empirically for each track because the flight tracks were quite short near the source and longer further away. This was done on basis of the observed plume signal seen in the cross sections (Fig. S4, right column), whereby a broadening of the plume, while moving away from the source, was also considered. Additionally, the maximal width of the plume area of the latter remote sensing tracks was further constrained by the approximate plume width observed in the in-situ measurements. The mean emission based on the 8 downwind tracks is ~~16.4~~16.2 $\mathrm{kt\ CH_4\ yr^{-1}}$ (±23 %).

The 27.08.2014 and 28.08.2014 flights ~~are~~ were more challenging with respect to the flux inversion because of the not optimal flight patterns. This resulted in there being few measurements for concentration background normalisation and a non-optimal orientation of the flight tracks with respect to the prevailing wind direction. Additionally, higher wind speeds potentially ~~lead~~ led to smaller column enhancements. The flight parameters are listed in Table 1, Figs. S1 and S2 show the flight pattern and Fig. S4 (left and middle column) the downwind tracks.

On the 27.08.2014, the area used for background normalization was empirically set and also additionally constrained by the approximate plume width estimated from the in-situ measurements. In contrast to the remaining flights, the inclination filter was relaxed to 6° to increase the number of measurements north of the observed plume. Analysis using the 5 downwind tracks yields a mean emission of 13.0 $\mathrm{kt\ CH_4\ yr^{-1}}$ (±45 %).

The 28.08.2014 flight was treated in a similar manner to the flights before using again the standard inclination filter of 5°. The resultant mean emission rate from the 6 downwind tracks is ~~13.7~~13.6 $\mathrm{kt\ CH_4\ yr^{-1}}$ ~~. A detailed error discussion is given in Sect. 3.1.1.~~ (±39 %).

4.1.1 ~~Uncertainty of estimated MAMAP~~ Uncertainties related to remote sensing based emission rates

~~The largest errors or uncertainties for~~

The uncertainties of the remote sensing based emission ~~estimates originate from uncertainties of the wind parameters used (wind speed and direction), the chosen concentration background normalisation area, the track-to-track variability and the influence of variations in terms of the applied proxy method. Uncertainty estimates for these error sources~~ rate estimates are based on the methodology described in Sect. 3.1.1 and are listed in Table 2. ~~A detailed error discussion of the different error sources is given in the following.~~ In the following, a short discussion of the estimated errors for the four measurement flights is given.

~~A wind speed error linearly propagates into the emission estimate. As the in-situ measurements of the 5-hole turbulence probe were utilized for the wind speed estimates, the accuracy of the probe is used as a first order approximation for an uncertainty estimate. The uncertainty of the turbulence probe wind speed data is 0.5.~~ **Wind speed (0.5 $\mathrm{m\,s^{-1}}$):** The resulting uncertainty on the estimated flux is around ±~~11~~12 % and ±9 % for the 01.09.2016 and 03.09.2016 flight. respectively. The

uncertainty is slightly smaller on the 27.08.2014 ($\pm 8\,\%$) and on the 27.08.2014 ($\pm 6\,\%$) (compare to Table 1) as a ~~results~~ result of the higher wind speeds.

~~The wind direction enters the flux estimate via a cosine term by modifying the used perpendicular wind speed to each flight track, provided that the track orientation is not perpendicular to the mean wind direction. An error on the wind direction of ± 10has been assumed for the case when wind direction is derived from the measurements themselves.~~

Wind direction (10°): On the 01.09.2014, the remote sensing tracks were flown nearly perpendicular to the estimated prevailing wind direction with an average deviation of only 3°. The assumed error in the wind direction of 10° leads to an uncertainty in the emission estimate of up to 2 %. For the 03.09.2014 flight, the mean deviation from the perpendicular wind direction was around 13° leading to a maximum emission uncertainty of 6 %. The largest mean deviation from the perpendicular wind direction of around 60° is observed on the 27.08.2014. For a $\pm 10°$ wind direction uncertainty, this leads to an uncertainty in the emission rate of maximal 22 %. On the 28.09.2014, the deviation of around 35° with respect to the perpendicular wind direction was smaller in comparison to the 27.08.2014 flight leading to a ~~maximal~~ maximum uncertainty in the emission rate of 14 %.

~~When inspecting the downwind tracks used for the emission estimates in, e.g., Figs. 6 and 7 for the 01.09.2014, it becomes obvious that the limits for~~ **Background normalization area (shifting limits):** Varying and shifting the limits of the background normalisation area ~~also have an influence on the final results. In order to test their impact on the final emission estimate, the limits were shifted towards or away from the center line by a certain distance. For this type of test, one needs to keep in mind that if the limits are too close to the plume, part of the plume signal enters the area used for the background normalization leading to an underestimate of the emission. On the other hand, if the limits are too far away, there might be not sufficient measurements left to calculate a reliable concentration background. Thus, the limits were varied by ± 250 and $\pm 500$and, additionally, the defined plume area was shifted as a whole by 250 and 500to the right and left with respect to the center line. This yields a maximal~~ yield a maximum change in the emission of around 19 % and 18 % for the 01.09.2014 and the 03.09.2014, respectively. For the 27.08.2914 and 28.08.2914, the ~~maximal~~ maximum uncertainty in the emission rate is around 34 % and 29 %, respectively.

~~Additionally, we computed the statistical error contribution. This error source is referred to as track-to-track variability in the following. Based on the used downwind tracks, a standard deviation σ and from that the uncertainty of the mean, is calculated. This yields a~~ **Track-to-track variability (statistics):** The 1-σ ~~uncertainty of~~ track-to-track variability is $\pm$~~6.9~~6.8 kt CH_4 yr^{-1}, or $\pm 50\,\%$ of the derived mean emission rate, for a single track and ~~an~~ the resulting error on the averaged emission ~~of~~ is around $\pm 14\,\%$ when using the 13 downwind tracks ~~(for further details, see Farrance and Frenkel, 2012)~~ on the 01.09.2014. On the 03.09.2014, the observed 1-σ ~~track-to-track variability~~ uncertainty is $\pm$~~5.3~~5.2 kt CH_4 yr^{-1} (or $\pm 32\,\%$) based on eight tracks yielding an error of around $\pm 11\,\%$ on the mean emission rate. The track-to-track variability is $\pm$~~4.6~~4.5 kt CH_4 yr^{-1} (or $\pm 35\,\%$) on the 27.08.2014 leading to an error on the average of around $\pm 16\,\%$ considering the five downwind tracks. On the 28.08.2014, the track-to-track variability of the six downwind tracks is $\pm$~~6.3~~6.2 kt CH_4 yr^{-1} (or $\pm 46\,\%$) causing an error on the ~~average~~ averaged emission rate of around $\pm 19\,\%$~~in the emission rate estimate~~.

~~For the remote sensing emission rate estimate, the columns, determined using the proxy method, are used. The proxy method assumes that was equally distributed and did not change in the measured area during the flight. In general, any enhancement would lead to a decline in the derived . The influence of such a anomaly on the emission rate estimate depends on its location. On the one hand, the enhancements can be co-located to the landfill plume for the case when the is co-emitted. This will lead to an underestimation of the emission rate. On the other hand, if the originates from outside the measurement area, the enhancement is not co-located to the plume. This results in an under- or overestimation of the emission rate depending on the location and distribution of the variations.~~

~~Cross-sections of the relative column enhancements determined from the integrated in-situ columns (IISCs) of the first (a) and second (b) downwind wall of the Olinda Alpha Landfill measurements on 01.09.2014. The blue solid lines ($IISC_{CH_4/CO_2}$) represent the cases which are influenced by the co-emitted , whereas the red solid lines ($IISC_{CH_4}$) are not. The measurements enclosed by the black dotted lines and located at the flanks / edges of the plume are used for normalization and determination of the background.~~

~~To estimate the influence of a variable concentration in the measurement area on the remote sensing emission rate estimates, integrated in-situ columns (IISCs) were derived for the measured in-situ walls. The in-situ and measurements were vertically integrated from the surface to highest altitude of the in-situ wall. Subsequently, the two obtained IISCs for and were similarly treated as they would be in the MAMAP proxy approach. First, the column was divided by the column and then the track was background normalized by its edges. This results on the one hand in an $IISC_{CH_4}$ from the enhancement only, which is not influenced by variations, and on the other in an $IISC_{CH_4/CO_2}$ which considers variations.~~

Background CO_2 variation (proxy method): Figure 8 shows exemplarily the background normalized IISCs of the two downwind walls on the 01.09.2014 for the background normalized $IISC_{CH_4}$ (red solid line) and $IISC_{CH_4/CO_2}$ (blue solid line). On that day, the CO_2 plume ~~is~~ was co-located to the CH_4 plume and causes a reduction of the CH_4 plume signal. This finding is consistent with the kriged CH_4 and CO_2 in-situ measurements in Figs. S7 (d, f for CH_4) and S12 (d, f for CO_2), which show a well-defined CO_2 enhancement at the position of the methane plume.

~~To quantitatively estimate the influence of this offset on the final emission rate estimate, the emission through each in-situ based cross-section $IISC_{CH_4}$ and $IISC_{CH_4/CO_2}$ is calculated by using Eq. 1. The column enhancement V and the length segment Δx are given by Fig. 8, whereby the remaining parameters, especially the perpendicular wind speed, cancel out, because we are only investigating in the relative difference.~~

On the 01.09.2014, the derived emission rates are by around ~~5.0~~4.6 % (first downwind wall) to ~~11.7~~11.9 % (second downwind wall) higher if the influence of the CO_2 on the emission rate is neglected.

Assuming that this in-situ based derived bias is valid for the entire measurement area, which is covered by the remote sensing instruments, indicates that the emission rate estimates based on the remote sensing data are also underestimated by around ~~5.0~~4.6 % to ~~11.7~~11.9 % due to the co-located CO_2 on the 01.09.2014.

Applying this method to the other downwind walls yields around +~~1.7~~0.6 % (27.08.2014), -~~15.8~~14.9 % (28.08.2014) and +~~3.6~~3.3 % (03.09.2014). The IISCs of these walls are found in the supplement (Figs. S14, S15 and S16). Strictly speaking, due to the potential temporal and spatial variability of the CO_2 variations, these calculated biases estimated from the downwind

walls are not assumed to be valid for the remote sensing tracks of the associated flight day, which were recorded at a different time and location. Therefore, we used the 1-σ deviation of the derived biases to estimate one uncertainty of around $\pm 10\,\%$ for the entire remote sensing data set.

Surface albedo (0.22 and 0.40): The influence of a wrongly assumed surface albedo used in the RTM simulations has only a minor effect on the estimated emission rates. For the four flights, the relative error is well below 1 %.

Total uncertainties: The ~~total uncertainties were calculated by root-sum-squaring the single uncertainties for each day with the underlying assumption that the error sources are not correlated. The~~ resulting total uncertainties including the uncertainties in wind information, normalization area, track-to-track variability~~and ,~~ CO_2 variations and surface albedo, of the remote sensing measurements for the 01.09.2014, 03.09.2014, 27.06.2014 and 28.06.2014 are 28 % (or ~~3.9~~3.8 kt CH_4 yr^{-1}), 26 % (or ~~4.3~~4.2 kt CH_4 yr^{-1}), ~~46~~45 % (or 5.9 kt CH_4 yr^{-1}) and 39 % (or 5.3 kt CH_4 yr^{-1}), respectively.

4.1.2 ~~Non-linearity and associated negative anomalies~~

~~When investigating the MAMAP remote sensing measurements on the 01.09.2014 (Fig. 6, a), they also show, besides a clear plume structure downwind of the landfill, some blue spots. First investigations have revealed some column dependencies on the signal strength. The scatter plot in Fig. 3 shows the ratio of the retrieved and profile scaling factors as a function of signal strength. It (black diamonds) clearly shows a decrease in the ratio for lower signals and also a less pronounced decrease for higher signal strengths. The cause of this dependency is still under investigation. The effect is most pronounced on the 01.09.2014 flight having the most measurements at lower signal strengths (e.g., 32below 13000) with respect to the three other days (5on 27.08.2014, 12on 28.08.2014 and 2of the measurements on 27.08.2014). Therefore, the effect is further investigated exemplarily for the 01.09.2014.~~

~~Scatter plot of the ratio of the retrieved and column over the maximum signal strength on the 01.09.2014. Black diamonds: Non-corrected data, left scale. Red solid line: Fitted 3^{rd} order polynomial. Green diamonds: Corrected data, right scale.~~

~~In order to test the hypothesis that the negative anomalies originate from this signal dependency on the 01.09.2014, a 3^{rd} order polynomial (Fig. 3, red solid line) was fitted to the scattered data and subsequently used for correction. The new data set exhibits nearly no signal strength dependency (Fig. 3, green diamonds). Furthermore, the blue spots in Fig. 6 (b) are reduced compared to Fig. 6 (a). The 1-σ track-to-track variability of $\pm$6.9has also been reduced by 26to about $\pm$5.1(or $\pm$37).~~

~~It is expected that this effect was less relevant for measurements from previous campaigns because the measured radiance signals and column enhancements were significantly higher than here. The mean emission changes furthermore by less than 2for the investigated Olinda Alpha Landfill measurements on the 01.09.2014 due to this effect and can therefore be neglected.~~

4.2 Emission rates from Picarro in-situ data

For comparison with the MAMAP remote sensing estimates, CH_4 emission rates from the Olinda Alpha Landfill were also derived from consecutive in-situ measurements made by the Picarro instrument performed with the same aircraft for each of the four days, where MAMAP remote sensing data was acquired. In total, five in-situ walls were flown downwind of the landfill during the period. The emission rate estimates for each wall ~~have been~~ were calculated using the Kriging and mass balance

Table 2. Summary of the derived emission rates denoted as 'retrieved baseline' and their related relative errors from the remote sensing (RS) and in-situ (IS) data set of the Olinda Alpha Landfill measurements.

Error type		27.08.2014	28.08.2014	01.09.2014		03.09.2114 2014
RS	Retrieved baseline [kt CH_4 yr^{-1}]	13.0	13.7 13.6	13.6		16.4 16.2
	Wind speed [%]	7.9	6.1 6.2	11.5		9.0 9.1
	Wind direction [%]	22.2	13.7	2.4		5.5
	Background normalization area [%]	34.1	29.0	18.6		18.1
	Track-to-track variability [%]	15.7	18.7	13.9		11.4
	Background CO_2 variation[a)] [%]	10.3 9.9	10.3 9.9	9.9		10.3 9.9
	Surface albedo [%]	≤ 1	≤ 1	< 1		≤ 1
	Total uncertainty [%]	45.5 45.4	39.0 38.9	27.9		26.0 25.9
IS [b)]		dw1[b)]	dw1	dw1	dw2	dw1
	Retrieved baseline [kt CH_4 yr^{-1}]	12.0 11.6	16.8 16.6	18.2 17.8	14.8 14.6	13.8 13.9
Group a)	Wind speed [%]	12.4 7.9	6.3 6.2	14.4 12.5	12.6 11.5	10.4 9.1
	Unknown surface concentrations [%]	5.2 6.0	8.1 8.3	15.8 17.0	10.0 9.8	13.1 13.6
	Time lag [%]	10.1 7.9	8.4 4.1	6.6 4.9	1.8 3.1	4.1 2.8
Group b)	Kriging parameters [%]	4.6 4.7	7.7 12.8	16.2 18.0	2.8 7.0	9.1 15.9
	Background concentrations / area [%]	2.6 3.4	6.8 7.0	2.9 2.7	7.3	2.5 2.1
	Total uncertainty [%]	17.6 13.9	16.8 18.4	27.8 28.3	18.0 18.4	19.6 23.1

[a)] based on the CH_4 and CO_2 in-situ measurements
[b)] dw = downwind wall

method as described in Sect. 3.2. The downwind walls of the dry gas mixing ratios of CH_4 and the effective wind speeds obtained by Kriging can be found in the supplement (Sect supplementary material (Sects. S2 and S4).

For the lag separation distance or bin width h_{sep} (see Sect. 3.2), a value of 40 120 m , leading to a lag tolerance of 20, was chosen for calculating the experimental semivariograms. This value is based on the Picarro instrument, which is the „slowest" in-situ instrument in terms of measurement frequency, whose measurements are used in Eq. 5 for the emission rate estimate. The Picarro greenhouse gas sensor acquires measurements at around 1.7 0.5 Hz, corresponding to a measurement every 0.6 2 s. In combination with the flight speed of the aircraft of around 60 m s^{-1}, this leads to a spatial resolution of around $\lesssim$ 40 120 m. To cover at least one pair of measurements per lag distance h_j, a lag separation distance or bin width h_{sep} of around 40 120 m is needed.

For fitting the exponential model to the experimental semivariograms, only half of the maximum possible lag distance (largest distance by which a pair of measurements on the wall is separated) has been was used following the recommendations

in Journel and Huijbregts (1978). Figure 4 shows an example of an experimental semivariogram with the fitted exponential function and the related parameters range, nugget and partial sill.

As mentioned in Sect. ??2.1, to account for the fact that measurements ~~are~~ were not available at the surface, a pseudo-track ~~is~~ was added at the surface. It follows the surface terrain and, in a first order approximation, has the same concentration values of CH_4 and CO_2 as measured at the altitude of the lowest flight track of the according wall. The surface winds for the pseudo-track were estimated from measurements of the weather station MTNRC1[8] located at the north eastern tip of the Olinda Alpha Landfill. The resulting surface wind speeds and directions at the time the downwind walls were acquired ~~are~~ were $5.8\,\mathrm{m\,s^{-1}}$ and 219° (27.08.2014), $5.9\,\mathrm{m\,s^{-1}}$ and 228° (28.08.2014), $4.5\,\mathrm{m\,s^{-1}}$ and 209° (dw1, 01.09.2014), $4.5\,\mathrm{m\,s^{-1}}$ and 209° (dw2, 01.09.2014), and $4.9\,\mathrm{m\,s^{-1}}$ and 220° (03.09.2014). This pseudo-track ~~is~~ was used to extrapolate the measurements and close the gap between the lowest flight leg and the surface.

The ~~mean perpendicular~~ wind speeds for the five downwind walls measured on the four days varied between ~~3.5 and 8.0~~4.0 and 8.1 $\mathrm{m\,s^{-1}}$, retrieved from the measurements by the 5-hole turbulence probe and the surface weather station. These averaged wind speeds were calculated from all grid boxes, which exhibit a CH_4 enhancement larger than three times the standard deviation of the CH_4 signal in the background area. Subsequently, the wind speeds were also weighted by the amount of the enhanced CH_4 molecules in the respective grid boxes. The average area, for which the mean perpendicular wind speeds were calculated over, was around $1.0 \times 1.0\ \mathrm{km^2}$. This method was chosen to select the wind measurements, which belong to the CH_4 plume signal. The 3-σ threshold has also been used previously as limit for identifying and distinguishing plume signals from the surrounding background (e.g,. Hörmann et al., 2013; Zien et al., 2014).

The resulting emission rate estimates calculated by Eq. 5 vary between ~~12.0 and 18.2~~11.6 and 17.8 $\mathrm{kt\,CH_4\,yr^{-1}}$ with corresponding relative uncertainties between 14 % and 28 % during the one week of measurements (see Table 2 for details). When inspecting the three available in-situ upwind walls (Figs. S5~~(b)~~, b, S6~~(b)~~, b and S7~~(b))~~, b), it becomes clear that the calculated emissions are a feature of the emissions from the Olinda Alpha Landfill and are not an artefact of inflow of polluted air masses. The upwind walls do not exhibit any noticeable CH_4 enhancements or structures.

4.2.1 ~~Airborne~~ Uncertainties related to in-situ ~~error analysis~~based emission rate estimates

~~For the error budget of~~ The error budget for the in-situ based emission rates ~~, two groups of error sources have been identified: a) measurement related uncertainties and b) method related uncertainties. In the following, the different error sources are exemplarily discussed for the measurements on 01.09.2014. A summary of all errors for the 5 downwind walls measured on the four different days is given~~ is shortly discussed in the following. The underlying assumption were presented in Sect. 3.2.1 and uncertainties for the single downwind walls are listed in Table 2.

~~The main contributor to group a) is the measurement of the wind speed by the 5-hole turbulence probe of the CIRPAS instrumentation. Any error in the wind speed linearly propagates to the emission estimate (compare to Eq. 5). Using the averaged perpendicular wind speeds of the first (3.5) and second (~~**Wind speed (0.5 $\mathrm{m\,s^{-1}}$):** The averaged absolute wind speeds at the position of the 5 downwind walls varied between 4.0 and 8.1 $\mathrm{m\,s^{-1}}$~~) downwind wall on 01.09.2014, an accuracy~~

[8] https://www.wunderground.com/personal-weather-station/dashboard?ID=MTNRC1#history, last access: 16.11.2016

~~of 0.5~~. This translates into an uncertainty ~~in the emission estimate of around ±14~~of the estimated emissions of around 6 % ~~and ±~~to 13 % ~~, respectively. However, this is a slight overestimation because the error is not related to the larger absolute wind speed in wind direction but to the smaller perpendicular wind calculated relative to the fitted wall~~using the accuracy of 0.5 $\mathrm{m\,s^{-1}}$ of the wind probe.

~~The second largest error originates from the lack of measurements down to the surface . It was assumed as baseline that the plume had been well-mixed in the lower part of the atmospheric boundary layer. Due to the hilly area, accumulation of~~ **Unknown surface concentration (±50 %):** Varying the surface concentrations of CH_4 ~~in the valleys or lifts off could potentially also be possible. To quantify these effects, it was assumed that the pseudo-surface track used for extrapolation contains~~ of the pseudo-track at the surface by ±50~~or 150 % of the enhancements~~ with respect to the ~~lowest observed flight track. This yields emissions which deviate by maximal around ±16~~concentrations measured at the lowest flight track, results in emission rate variations between 6 % ~~for the 01.09.2014.~~

~~A third error source originates from the time lag, which is around 21. The sensitivity of the final emission estimate to a variation of the time lag by ±5is maximal 7~~and 17 %~~for the 01.09.2014~~.

~~Group b) consists of errors which originate e.g. from the chosen interpolation technique "Kriging" and how these data are used in the mass balance approach.~~

~~As discussed in the previous section, the Kriging method requires the three parameters nugget, (partial) sill and range, which were derived beforehand by fitting an exponential function to the experimental semivariogram for each quantity used in the mass balance approach. To quantify the influence of the Kriging parameters on the estimated emission and how sensitive it responds, the range was varied by a factor of 4 (i.e., -75~~**Time lag (5 s):** The maximal sensitive of the flux to a changing time lag is between 3 % and ~~+300~~8 %~~). Additionally, six configurations for the parameters nugget and partial sill (bearing in mind that the sill is the sum of partial sill and nugget) were investigated. On the one hand, the nugget was set to zero so that the partial sill equalled the sill and on the other hand, the nugget was increased to half of the sill and the partial sill was decreased to half of the sill. This was done for three different sills: the standard derived sill, two times the standard derived sill and half the standard derived sill. Furthermore, the effect of a varying lag separation distance, which also slightly influences the fitted parameters, is covered.~~ .

Kriging parameters: Varying Kriging parameters for the two quantities wind speed and CH_4 concentration have the largest influence on the final emission estimate, whereby the effect of temperature is negligible. The Kriging error results in a flux uncertainty of ~~at most 16~~between 5 % ~~for the 01.09.2014~~and 18 %. These tests show, that the influence of the Kriging parameters on the emission is comparable to other error sources but can also be one order of magnitude smaller. It is also important to emphasize, that the chosen values likely reflect the maximum deviations from the derived ones. When inspecting the experimental semivariograms in Fig. 4 it becomes obvious that, e.g., a nugget and partial sill value of 50 % of the sill or, e.g. in case of ~~temperature~~CH_4, a range reduced to ~~0.23~~ 0.7 or increased to ~~3.6~~10.8 km (fitted value is ~~0.9~~2.7 km~~for temperature~~), respectively, is quite unlikely. Therefore, it is expected, that the real uncertainty originating from the Kriging parameters is smaller.

~~A further error source originates from the limits for the background area. To test its sensitivity, the limits have been varied till their size had only 50of the original size.~~ **Background concentrations / area (shifting limits):** The resulting emission deviates by ~~up to~~ around 3 % and 7 %~~for the first and second downwind wall, respectively, on the 01.09.2014~~.

Total uncertainties: Combining the above mentioned error sources ~~and calculating the root sum square error yields a total uncertainty of around~~ yields total uncertainties of around 14 % to 28 % ~~(first downwind wall) and 18(second downwind wall) for the flight on the 01.09.2014. The uncertainties for the three other flight days are listed in Table 2.~~ or on average of around 3.1 kt CH_4 yr^{-1}.

4.3 CH_4 anomaly maps obtained by the AVIRIS-NG instrument

Airborne remote sensing measurements by the AVIRIS-NG imaging spectrometer were performed on the 03.09.2014. The instrument acquired five flight lines over the landfill at an flight altitude of around 3 km agl between 13:30 and 14:10 local time. The flight lines have a length of approximately 9 km and a swath of around 1.8 km resulting in a fine spatial resolution of around $3 \times 3\,m^2$. Figure 9 shows the derived CH_4 anomaly map of one flight line in the near field of the landfill using the algorithm described in ~~See~~Sect. 3.3. ~~The remaining flight lines, observed by the AVIRIS-NG instrument, are found in Fig. S17 in the supplement.~~ It shows a clear plume structure developing at the south-western slope of the landfill. This plume is also visible in the CH_4 anomaly maps for the ~~multiple~~ remaining AVIRIS-NG overpasses (see ~~supplement Fig. S17~~supplementary material Fig. S18). Due to atmospheric variability, its shape and intensity changes from overflight to overflight, but the plume remains visible. However, surface structures / surface albedo effects can cause spurious signals, which in the most cases can be identified as such.

5 ~~Comparison of emissions~~

4.1 Comparison ~~between~~ of MAMAP remote sensing ~~and~~ with Picarro in-situ data

The estimated emission rates of the Olinda Alpha Landfill from the airborne in-situ and remote sensing measurements agree well for the analysed days (see Fig. 10). Due to the time delay between the two surveys performed with both techniques and, thus, for example a possible change in wind direction, it is not expected that the location of the measured plumes is identical. Nevertheless, the positions of the plumes observed by the remote sensing and in-situ instrument are in close vicinity to each other for each of the four days (see Figs. 6~~(a)~~, a, S1, S2 and S3).

On the 01.09.2016, the emissions derived from the two in-situ downwind walls are ~~18.2~~17.8 kt CH_4 yr^{-1} ($\pm$28 %) and ~~14.8~~14.6 kt CH_4 yr^{-1} ($\pm$18 %), respectively. The difference between the two walls is ~~3.4~~3.2 kt CH_4 yr^{-1}, whereas the average emission rate based on the two in-situ walls is around ~~16.5~~16.2 kt CH_4 yr^{-1}. As suggested in Cambaliza et al. (2014), the difference between the walls can be related to the average emission rate and be used as a measure for the precision of this method. For the flight on the 01.09.2014, this results in a difference of around ~~21~~20 %, which is in good agreement with the values derived in Cambaliza et al. (2014) ranging from 12 % to 39 %.

Furthermore, the ~~averaged~~ in-situ based emission ~~rate is~~ rates are in good agreement with the remote sensing based emission ~~of 14.9(±28).~~

rates on all four days. The ~~in-situ and remote sensing based emission rates are also in good agreement on the 27.08.2014 (IS: 12.0±18, RS: 13.0±46) and 03.09.2014 (IS: 13.8±20, RS: 16.4±26).~~

~~The largest difference of around 3.1is observed on the 28.08.2014. On that day, the highest wind speeds were observed potentially leading to smaller measured column enhancements with respect to the measurements performed on the other days. Therefore, the resulting signals are more difficult to detect by MAMAP and part of the plume signal might be obscured due to the statistical measurement noise (precision) of the instrument leading to an underestimate of the emission.~~

~~The average absolute difference~~ average of the absolute differences between the emission rates based on remote sensing and in-situ is 2.4 $\mathrm{kt\,CH_4\,yr^{-1}}$. The corresponding uncertainty[9] is 2.8 $\mathrm{kt\,CH_4\,yr^{-1}}$ pointing out that the in-situ and remote sensing based emission rates are not significantly different.

4.2 Qualitative comparison between MAMAP and AVIRIS-NG data

On 03.09.2014, contemporaneous AVIRIS-NG measurements were performed and made available for a qualitative comparison. Figure 11 shows a comparison of the MAMAP remote sensing data on that day with one flight line acquired by AVIRIS-NG at around 13:33 local time. The MAMAP remote sensing measurements were acquired between 13:30 and 14:15 local time. To better visualize the CH_4 plume(s) detected by the AVIRIS-NG instrument on smaller scales, only measurements above a certain threshold are shown in the plot.

The AVIRIS-NG data shows a clear plume developing on the south-western slope of the landfill (red arrow) and travelling in downwind direction. It is in good agreement with the CH_4 plume seen by the MAMAP instrument.

~~The MAMAP remote sensing (coloured circles) and the AVIRIS-NG (pink shaded areas) measurements on the 03.09.2014 are shown. The RGB map underneath is also based on AVIRIS-NG observations. For better source attribution, only AVIRIS-NG measurements having a methane column enhancement of larger than 200are shown. The non threshold filtered flight track is depicted in the Fig. 9. The blue arrow depicts the approximate wind direction. Map underneath is provided by Google Earth.~~

4.3 Comparisons with the EPA inventory

Compared to the EPA inventory value of 11.5 $\mathrm{kt\,CH_4\,yr^{-1}}$ for 2014, our estimated emission rates are on average around ~~3.0~~2.8 $\mathrm{kt\,CH_4\,yr^{-1}}$ (with an uncertainty[10] of ±~~1.5~~1.6 $\mathrm{kt\,CH_4\,yr^{-1}}$) larger. Due to the scatter of the estimated emission rates and the limited number of measurement days, it is not possible to conclude that EPA is significantly underestimating the Olinda Alpha Landfill CH_4 emissions. It is also important to note that the derived fluxes in this work, expressed in units of $\mathrm{kt\,CH_4\,yr^{-1}}$, are only snapshots and valid for the time of the overflight (here: in the afternoon). In addition, the difference could also arise from the possible leakage identified in the AVIRIS-NG observations, which is not taken into account by EPA,

[9] based on error propagation of the single flux uncertainties given in Table 2 and the statistical error

[10] based on error propagation of the single flux uncertainties given in Table 2 and the statistical error

assuming that it was present on all measurement days. Furthermore, e.g., atmospheric pressure variations could potentially also lead to a deviation of the derived fluxes from the inventory value but are difficult to quantify.

4.4 Assessment of emission rates of the other measured landfills

Three out of four surveyed landfills (Scholl Canyon Landfill, SCL[11], Puente Hills Landfill, PHL[12] and BKK Landfill[13], compare to Sect. 2.1) did not show well-developed plume structures during the remote sensing survey and, therefore, were not further investigated. In order to assess whether their emission strengths were below the MAMAP remote sensing instrument detection limit for the time of the overflight or whether they were lower than reported, Observation System Simulation Experiments (OSSEs, Gerilowski et al., 2015) have been performed and compared to the actual acquired remote sensing data for the four data sets shown in Fig. 1. The OSSEs are based on Gaussian plume forward model simulations, which incorporates atmospheric conditions like wind speed and wind direction but also considers instrumental characteristics like the MAMAP single measurement precision, the ground scene size and the respective flight track. For the OSSE, multiple sources of equal source strength have been homogeneously distributed across the landfill (for details, see the Sect. S8 in the supplementary material). Fig. 12 (a) shows the MAMAP remote sensing data acquired over the Olinda Alpha Landfill on the 01.09.2014 and Fig. 12 (b) shows the corresponding OSSE, whereby simulated grid points were only plotted if the MAMAP instrument had also gathered data at the specific positions. In this case, to allow for a better comparison between measurements and simulation, the used emission strength in the OSSE is based on the mean value of the actual measured emission rates on the four days over the Olinda Alpha Landfill and the data have also been gridded to the same grid. There is a good qualitative agreement between simulation and measurements for the Olinda Alpha Landfill on the 01.09.2014 except some blue spots, which have been discussed in Sect. 3.1.2. More details on the OSSEs and the simulations of the three other landfills can be found in the supplementary material in Sect. S8.

According to EPA, the BKK Landfill is the largest of the four landfills in terms of CH_4 emissions. Although its expected CH_4 emissions for the year 2014 were around 30 % larger than that of the Olinda Alpha Landfill, no enhancements were detected by the MAMAP remote sensing instrument. The measurement flight of the BKK Landfill took place right before the Olinda Alpha Landfill flight on the 01.09.2014. Assuming that the weather conditions were similar for both targets and that BKK was emitting 15.1 $\mathrm{kt\ CH_4\ yr^{-1}}$, as stated by EPA, the plume should have been detected by the MAMAP remote sensing instrument. This is also confirmed by the OSSE simulations (Fig. S20, d), which shows a clear plume downwind of the landfill for that day assuming an emission rate of 15.1 $\mathrm{kt\ CH_4\ yr^{-1}}$ for the time of the overflight. It is also worthwhile to note that the emission rate given for the BKK Landfill by EPA might be to high. In case a landfill is equipped with a gas collection system, which is true for all four landfills, the landfill operator needs to report landfill emissions in two different ways (GPO, 2013), whereas the emissions reported by EPA represent always the larger estimate. The first approach A1 relies on forward calculations, whereas the second approach A2 on backward calculations (for details, see Sect. S9 in the supplementary material). In case of OAL

[11] https://ghgdata.epa.gov/ghgp/service/html/2014?id=1003198&et=undefined, last access: 10.05.2017
[12] https://ghgdata.epa.gov/ghgp/service/html/2014?id=1003199&et=undefined, last access: 10.05.2017
[13] https://ghgdata.epa.gov/ghgp/service/html/2014?id=1011449&et=undefined, last access: 10.05.2017

both approaches provide similar emission rates (also see Table S2). For BKK, A2 results in emission rates which are 14.2 kt lower than for A1. This large discrepancy may also indicate that the emission of the BKK Landfill are lower than reported.

The reported emissions for the Scholl Canyon Landfill and Puente Hills Landfill are similar for both approaches (2.1 to 5.9 kt CH_4 yr^{-1}). The OSSE simulation for SCL (Fig. S21, b, in the supplementary material) indicates that these emissions should likely have been visible in the MAMAP remote sensing measurements for the estimated wind conditions. For the PHL, the OSSE simulation (Fig. S21, d, in the supplementary material) indicates that these emissions are below the detection limit of the MAMAP remote sensing instrument for the given days, atmospheric conditions and instrumental characteristics.

5 Summary and conclusions

During the COMEX campaign, a comprehensive set of measurements over four landfills located in the Los Angeles Basin ~~has been~~ were collected. This study ~~analyses~~ analysed in detail the airborne measurements over the most promising target, the Olinda Alpha Landfill, to investigate the use of remote sensing measurements for estimating emission rates of areal sources of around 2 km^2 like a landfill. This landfill showed well-developed atmospheric CH_4 plume structures on all ~~four measurements~~measurement days, whereas the other three landfills showed no detectable plume structures during the time of the measurements.

The Olinda Alpha Landfill was measured on four days conducted within on week in late summer 2014.

During this time period, measurements of column-averaged dry air mole fractions, XCH_4, were acquired by the MAMAP remote sensing instrument while flying above the atmospheric boundary layer. In addition, after each remote sensing survey, consecutive in-situ measurements of CH_4 and CO_2 and other atmospheric parameters like wind speed and wind direction were gathered while probing the atmospheric boundary layer and crossing the plume emitted by the landfill.

Using the collected data ~~, the~~ set over the Olinda Alpha Landfill, CH_4 emission ~~rate of the landfill has~~ rates have been estimated from the remote sensing data and compared to the emission ~~rate~~ rates derived from the in-situ measurements. For that, an adapted mass balance approach ~~has been~~ was used for the emission rate estimates from the remote sensing data. In order to interpret and analyse the in-situ measurements, a Kriging method ~~has been~~ was applied. The average ~~absolute difference~~ of the absolute differences between the estimates from both data sets is ~~2.3~~2.4 kt CH_4 yr^{-1} ($\pm$2.8 kt CH_4 yr^{-1}) showing that the estimated emission rates agree well within the errors bars.

The resulting emissions have a range from around ~~13.0 to 18.2~~11.6 to 17.8 kt CH_4 yr^{-1} with case dependent relative uncertainties of around ~~17~~14 % to ~~46~~45 %. The contribution of the different error sources to the total uncertainty varies from case to case. For example, the remote sensing based emission rates are rather sensitive to the chosen background normalization area ~~.~~ or number of flight tracks downwind of the landfill. Thus, the uncertainties on the remote sensing based emission rates can be significantly reduced by using better adapted flight patterns for future activities. Additionally, the uncertainty of the remote sensing based emission rates, which is caused by a not constant CO_2 background concentration or by co-emitted CO_2 from the landfill, has been estimated by utilizing the CH_4 and CO_2 in-situ measurements.

In terms of the in-situ measurements, concentration measurements of CH_4 at the surface would significantly lower the error in most cases. The error related to the Kriging method used for interpolation between the different flight legs has maximally the same size as other errors but is generally only a minor contributor to the budget~~whereas~~. Additionally, it is also based on conservative assumptions.

There is also a good agreement in plume position between the CH_4 column enhancements observed by the non-imaging MAMAP instrument and the imaging AVIRIS-NG instrument for data obtained on 03.09.2014. The AVIRIS-NG observations make it possible to identify a CH_4 emission hot spot at the slope of the landfill, which could be a potential leakage, e.g., a leak in the cover layer.

Compared to the EPA inventory value, our estimates are on average ~~3.0~~2.8 $\mathrm{kt\ CH_4\ yr^{-1}}$ ($\pm$ ~~1.5~~1.6 $\mathrm{kt\ CH_4\ yr^{-1}}$) higher. This difference might be related to the identified potential leakage not considered by the EPA inventory value or by other reasons e.g., atmospheric pressure variations.

Our study shows for the first time, that medium resolution (~~Full Width at Half Maximum,~~ FWHM$\approx 0.9nm$) airborne based remote sensing measurements in the SWIR region at around 1.65 µm are ~~well suited to estimate the~~ well-suited to estimate total CH_4 ~~emission from a large landfill.~~ emissions from landfills at favourable conditions. Observation System Simulation Experiments (OSSEs) have been used to quantitatively investigate the detection limit of the MAMAP remote sensing instrument. The detection limit depends on the prevailing atmospheric conditions as well as on instrumental and flight specific parameters. The reported emission rate of, e.g., the Puente Hills Landfill (5.0 $\mathrm{kt\ CH_4\ yr^{-1}}$) were likely below the MAMAP detection limit at the time of the overflight for the given conditions. For the other landfills, Scholl Canyon (5.9 $\mathrm{kt\ CH_4\ yr^{-1}}$) and BKK Landfill (15.1 $\mathrm{kt\ CH_4\ yr^{-1}}$), the reported emission rates should likely have been visible in the MAMAP remote sensing measurements and, thus, the emission rates might have been smaller than reported.

Acknowledgements. The authors declare that they have no conflict of interest. Development of MAMAP was jointly funded by the University and State of Bremen and the Helmholtz Center Potsdam - GFZ German research Centre for Geosciences.

The MAMAP activities within the CO_2 and Methane EXperiment (COMEX) were funded in parts by the University and the State of Bremen, the European Space Agency (ESA) and the National Aeronautics and Space Administration (NASA).

Part of the research was carried out at the Jet Propulsion Laboratory, California Institute of Technology, under a contract with the National Aeronautics and Space Administration.

We would like to thank NASA AMES for the support regarding campaign coordination. Especially, we would also like to thank the CIRPAS team for the support during the entire campaign.

References

Amini, H. R., Reinhart, D. R., and Mackie, K. R.: Determination of first-order landfill gas modeling parameters and uncertainties, Waste Management, 32, 305 – 316, doi:http://dx.doi.org/10.1016/j.wasman.2011.09.021, 2012.

Amini, H. R., Reinhart, D. R., and Niskanen, A.: Comparison of first-order-decay modeled and actual field measured municipal solid waste landfill methane data, Waste Management, 33, 2720 – 2728, doi:http://dx.doi.org/10.1016/j.wasman.2013.07.025, 2013.

Babilotte, A., Lagier, T., Fiani, E., and Taramini, V.: Fugitive Methane Emissions from Landfills: Field Comparison of Five Methods on a French Landfill, Journal of Environmental Engineering, 136, 777–784, doi:10.1061/(ASCE)EE.1943-7870.0000260, 2010.

Bovensmann, H., Buchwitz, M., Burrows, J. P., Reuter, M., Krings, T., Gerilowski, K., Schneising, O., Heymann, J., Tretner, A., and Erzinger, J.: A remote sensing technique for global monitoring of power plant CO_2 emissions from space and related applications, Atmospheric Measurement Techniques, 3, 781–811, doi:10.5194/amt-3-781-2010, 2010.

Buchwitz, M., Rozanov, V. V., and Burrows, J. P.: A near-infrared optimized DOAS method for the fast global retrieval of atmospheric CH_4, CO, CO_2, H_2O, and N_2O total column amounts from SCIAMACHY Envisat-1 nadir radiances, Journal of Geophysical Research: Atmospheres, 105, 15 231–15 245, doi:10.1029/2000JD900191, 2000.

Buchwitz, M., Reuter, M., Bovensmann, H., Pillai, D., Heymann, J., Schneising, O., Rozanov, V., Krings, T., Burrows, J. P., Boesch, H., Gerbig, C., Meijer, Y., and Löscher, A.: Carbon Monitoring Satellite (CarbonSat): assessment of atmospheric CO_2 and CH_4 retrieval errors by error parameterization, Atmospheric Measurement Techniques, 6, 3477–3500, doi:10.5194/amt-6-3477-2013, 2013.

Caers, J.: Modeling uncertainty in the earth sciences, Wiley, Hoboken, NJ [u.a.], 2011.

Cambaliza, M. O. L., Shepson, P. B., Caulton, D. R., Stirm, B., Samarov, D., Gurney, K. R., Turnbull, J., Davis, K. J., Possolo, A., Karion, A., Sweeney, C., Moser, B., Hendricks, A., Lauvaux, T., Mays, K., Whetstone, J., Huang, J., Razlivanov, I., Miles, N. L., and Richardson, S. J.: Assessment of uncertainties of an aircraft-based mass balance approach for quantifying urban greenhouse gas emissions, Atmospheric Chemistry and Physics, 14, 9029–9050, doi:10.5194/acp-14-9029-2014, 2014.

Capaccioni, B., Caramiello, C., Tatano, F., and Viscione, A.: Effects of a temporary HDPE cover on landfill gas emissions: Multiyear evaluation with the static chamber approach at an Italian landfill, Waste Management, 31, 956 – 965, doi:http://dx.doi.org/10.1016/j.wasman.2010.10.004, 2011.

Chen, Y., Sun-Mack, S., Arduini, R. F., and Minnis, P.: Clear-sky and surface narrowband albedo variations derived from VIRS and MODIS Data, in: CONFERENCE ON CLOUD PHYSICS, CD ROM EDITION, 5.6 Atmospheric radiation 12th, Conference, Atmospheric radiation, vol. 12, Atmospheric radiation, Boston, Mass., USA, 2006.

Cressie, N.: Statistics for spatial data, Wiley series in probability and mathematical statistics: Applied probability and statistics, J. Wiley, https://books.google.de/books?id=4SdRAAAAMAAJ, 1993.

Crosson, E.: A cavity ring-down analyzer for measuring atmospheric levels of methane, carbon dioxide, and water vapor, Applied Physics B, 92, 403–408, doi:10.1007/s00340-008-3135-y, 2008.

Czepiel, P., Shorter, J., Mosher, B., Allwine, E., McManus, J., Harriss, R., Kolb, C., and Lamb, B.: The influence of atmospheric pressure on landfill methane emissions, Waste Management, 23, 593 – 598, doi:http://dx.doi.org/10.1016/S0956-053X(03)00103-X, second Intercontinental Landfill Resarch Symposium, 2003.

Eklund, B., Anderson, E. P., Walker, B. L., and Burrows, D. B.: Characterization of Landfill Gas Composition at the Fresh Kills Municipal Solid-Waste Landfill, Environmental Science & Technology, 32, 2233–2237, doi:10.1021/es980004s, 1998.

ESA: Report for Mission Selection: CarbonSat, ESA SP-133/1 (2 volume series), European Space Agency, Noordwijk, The Netherlands, 2015.

Farrance, I. and Frenkel, R.: Uncertainty of Measurement: A Review of the Rules for Calculating Uncertainty Components through Functional Relationships, The Clinical Biochemical Reviews, 33, 49–75, 2012.

Frankenberg, C., Thorpe, A. K., Thompson, D. R., Hulley, G., Kort, E. A., Vance, N., Borchardt, J., Krings, T., Gerilowski, K., Sweeney, C., Conley, S., Bue, B. D., Aubrey, A. D., Hook, S., and Green, R. O.: Airborne methane remote measurements reveal heavy-tail flux distribution in Four Corners region, Proceedings of the National Academy of Sciences, 113, 9734–9739, doi:10.1073/pnas.1605617113, 2016.

Gebert, J. and Groengroeft, A.: Passive landfill gas emission - Influence of atmospheric pressure and implications for the operation of methane-oxidising biofilters, Waste Management, 26, 245 – 251, doi:http://dx.doi.org/10.1016/j.wasman.2005.01.022, 2006.

Gerilowski, K., Tretner, A., Krings, T., Buchwitz, M., Bertagnolio, P. P., Belemezov, F., Erzinger, J., Burrows, J. P., and Bovensmann, H.: MAMAP - a new spectrometer system for column-averaged methane and carbon dioxide observations from aircraft: instrument description and performance analysis, Atmospheric Measurement Techniques, 4, 215–243, doi:10.5194/amt-4-215-2011, 2011.

Gerilowski, K., Krautwurst, S., Koyler, R., Jonsson, H., Krings, T., Horstjann, M., Leifer, I., Schuettemeyer, D., Fladeland, M., Burrows, J. P., Bovensmann, H. Buchwitz, M., Hartmann, J., Sachs, T., Erzinger, J., Burrows, J. P., and Bovensmann, H.: Remote sensing of large scale methane emission sources with the Methane Airborne MAPper (MAMAP) instrument over the Kern River and Kern Front Oil fields and validation through airborne in-situ measurements - Initial results from COMEX, in: American Geophysical Union AGU, https://agu.confex.com/data/handout/agu/fm14/Paper_21807_handout_1014_0.pdf, 2014.

Gerilowski, K., Krings, T., Hartmann, J., Buchwitz, M., Sachs, T., Erzinger, J., Burrows, J. P., and Bovensmann, H.: Atmospheric remote sensing constraints on direct sea-air methane flux from the 22/4b North Sea massive blowout bubble plume, Marine and Petroleum Geology, 68, 824–835, doi:10.1016/j.marpetgeo.2015.07.011, 2015.

Gordon, M., Li, S.-M., Staebler, R., Darlington, A., Hayden, K., O'Brien, J., and Wolde, M.: Determining air pollutant emission rates based on mass balance using airborne measurement data over the Alberta oil sands operations, Atmospheric Measurement Techniques, 8, 3745–3765, doi:10.5194/amt-8-3745-2015, http://www.atmos-meas-tech.net/8/3745/2015/, 2015.

GPO: U.S. Government Publishing Office; U.S. Environmental Protection Agency: Rules and Regulations; Federal Register; Vol. 78; No. 230, available at http://www.gpo.gov/fdsys/pkg/FR-2013-11-29/pdf/2013-27996.pdf, last access: 15.05.2017, 2013.

Green, R. O., Eastwood, M. L., Sarture, C. M., Chrien, T. G., Aronsson, M., Chippendale, B. J., Faust, J. A., Pavri, B. E., Chovit, C. J., Solis, M., Olah, M. R., and Williams, O.: Imaging Spectroscopy and the Airborne Visible/Infrared Imaging Spectrometer (AVIRIS), Remote Sensing of Environment, 65, 227 – 248, doi:10.1016/s0034-4257(98)00064-9, 1998.

Hamlin, L., Green, R. O., Mouroulis, P., Eastwood, M., Wilson, D., Dudik, M., and Paine, C.: Imaging spectrometer science measurements for Terrestrial Ecology: AVIRIS and new developments, in: Aerospace Conference, 2011 IEEE, pp. 1–7, doi:10.1109/AERO.2011.5747395, 2011.

Hörmann, C., Sihler, H., Bobrowski, N., Beirle, S., Penning de Vries, M., Platt, U., and Wagner, T.: Systematic investigation of bromine monoxide in volcanic plumes from space by using the GOME-2 instrument, Atmospheric Chemistry and Physics, 13, 4749–4781, doi:10.5194/acp-13-4749-2013, 2013.

IPCC: 2006 IPCC Guidelines for National Greenhouse Gas Inventories, 2006.

Isaaks, E. H. and Srivastave, R.: Applied geostatistics, Oxford Univ. Press, New York, NY [u.a.], 1989.

Journel, A. and Huijbregts, C.: Mining geostatistics, Academic P., http://katalog.suub.uni-bremen.de/DB=1/LNG=DU/CMD?ACT=SRCHA&IKT=8000&TRM=17378616, 1978.

Kirschke, S., Bousquet, P., Ciais, P., Saunois, M., Canadell, J., Dlugokencky, E., Bergamaschi, P., Bergmann, D., Blake, D., Bruhwiler, L., Cameron-Smith, P., Castaldi, S., Chevallier, F., Feng, L., Fraser, A., Heimann, M., Hodson, E., Houweling, S., Josse, B., Fraser, P., Krummel, P., Lamarque, J.-F., Langenfelds, R., Le Quere, C., Naik, V., O'Doherty, S., Palmer, P., Pison, I., Plummer, D., Poulter, B., Prinn, R., Rigby, M., Ringeval, B., Santini, M., Schmidt, M., Shindell, D., Simpson, I., Spahni, R., Steele, L., Strode, S., Sudo, K., Szopa, S., Van Der Werf, G., Voulgarakis, A., Van Weele, M., Weiss, R., Williams, J., and Zeng, G.: Three decades of global methane sources and sinks, Nature Geoscience, 6, 813–823, doi:10.1038/ngeo1955, 2013.

Krige, D. G.: A Statistical Approach to Some Basic Mine Valuation Problems on the Witwatersrand, Journal of the Chemical, Metallurgical and Mining Society of South Africa, 52, 119–139, doi:10.2307/3006914, 1951.

Krings, T., Gerilowski, K., Buchwitz, M., Reuter, M., Tretner, A., Erzinger, J., Heinze, D., Pflüger, U., Burrows, J. P., and Bovensmann, H.: MAMAP - a new spectrometer system for column-averaged methane and carbon dioxide observations from aircraft: retrieval algorithm and first inversions for point source emission rates, Atmospheric Measurement Techniques, 4, 1735–1758, doi:10.5194/amt-4-1735-2011, 2011.

Krings, T., Gerilowski, K., Buchwitz, M., Hartmann, J., Sachs, T., Erzinger, J., Burrows, J. P., and Bovensmann, H.: Quantification of methane emission rates from coal mine ventilation shafts using airborne remote sensing data, Atmospheric Measurement Techniques, 6, 151–166, doi:10.5194/amt-6-151-2013, 2013.

Krings, T., Neininger, B., Gerilowski, K., Krautwurst, S., Buchwitz, M., Burrows, J. P., Lindemann, C., Ruhtz, T., Schüttemeyer, D., and Bovensmann, H.: Airborne remote sensing and in-situ measurements of atmospheric CO_2 to quantify point source emissions, Atmospheric Measurement Techniques Discussions, 2016, 1–30, doi:10.5194/amt-2016-362, 2016.

Lavoie, T. N., Shepson, P. B., Cambaliza, M. O. L., Stirm, B. H., Karion, A., Sweeney, C., Yacovitch, T. I., Herndon, S. C., Lan, X., and Lyon, D.: Aircraft-Based Measurements of Point Source Methane Emissions in the Barnett Shale Basin, Environmental Science & Technology, 49, 7904–7913, doi:10.1021/acs.est.5b00410, 2015.

Lee, C. M., Cable, M. L., Hook, S. J., Green, R. O., Ustin, S. L., Mandl, D. J., and Middleton, E. M.: An introduction to the NASA Hyperspectral InfraRed Imager (HyspIRI) mission and preparatory activities, Remote Sensing of Environment, 167, 6 – 19, doi:http://dx.doi.org/10.1016/j.rse.2015.06.012, 2015.

Mays, K. L., Shepson, P. B., Stirm, B. H., Karion, A., Sweeney, C., and Gurney, K. R.: Aircraft-Based Measurements of the Carbon Footprint of Indianapolis, Environmental Science & Technology, 43, 7816–7823, doi:10.1021/es901326b, 2009.

Myhre, G., Shindell, D., Breon, F.-M., Collins, W., Fuglestvedt, J., Huang, J., Koch, D., Lamarque, J.-F., Lee, D., Mendoza, B., Nakajima, T., Robock, A., Stephens, G., Takemura, T., and Zhang, H.: Anthropogenic and Natural Radiative Forcing, book section 8, pp. 659–740, Cambridge University Press, Cambridge, United Kingdom and New York, NY, USA, doi:10.1017/CBO9781107415324.018, www.climatechange2013.org, 2013.

NSWMA: Modern landfills: A far cry from the past, National Solid Wastes Management Association, https://books.google.de/books?id=u77ZNwAACAAJ, 2006.

Peischl, J., Ryerson, T. B., Brioude, J., Aikin, K. C., Andrews, A. E., Atlas, E., Blake, D., Daube, B. C., de Gouw, J. A., Dlugokencky, E., Frost, G. J., Gentner, D. R., Gilman, J. B., Goldstein, A. H., Harley, R. A., Holloway, J. S., Kofler, J., Kuster, W. C., Lang, P. M., Novelli, P. C., Santoni, G. W., Trainer, M., Wofsy, S. C., and Parrish, D. D.: Quantifying sources of methane using light alkanes in the Los Angeles basin, California, Journal of Geophysical Research: Atmospheres, 118, 4974–4990, doi:10.1002/jgrd.50413, 2013.

Poulsen, T. G. and Moldrup, P.: Evaluating effects of wind-induced pressure fluctuations on soil-atmosphere gas exchange at a landfill using stochastic modelling, Waste Management & Research, 24, 473–481, doi:10.1177/0734242X06066363, 2006.

Poulsen, T. G., Christophersen, M., Moldrup, P., and Kjeldsen, P.: Relating landfill gas emissions to atmospheric pressure using numerical modelling and state-space analysis, Waste Management & Research, 21, 356–366, doi:10.1177/0734242X0302100408, 2003.

Rella, C.: Accurate Greenhouse Gas Measurement: in Humid Gas Streams Using the Picarro G1301 Carbon Dioxide / Methane / Water Vapour Gas Analyzer, Tech. rep., Picarro Inc., http://www.picarro.com/products_solutions/trace_gas_analyzers/co_co2_ch4_h2o, 2010.

Rella, C. W., Chen, H., Andrews, A. E., Filges, A., Gerbig, C., Hatakka, J., Karion, A., Miles, N. L., Richardson, S. J., Steinbacher, M., Sweeney, C., Wastine, B., and Zellweger, C.: High accuracy measurements of dry mole fractions of carbon dioxide and methane in humid air, Atmospheric Measurement Techniques, 6, 837–860, doi:10.5194/amt-6-837-2013, http://www.atmos-meas-tech.net/6/837/2013/, 2013.

Rothman, L., Gordon, I., Babikov, Y., Barbe, A., Benner, D. C., Bernath, P., Birk, M., Bizzocchi, L., Boudon, V., Brown, L., Campargue, A., Chance, K., Cohen, E., Coudert, L., Devi, V., Drouin, B., Fayt, A., Flaud, J.-M., Gamache, R., Harrison, J., Hartmann, J.-M., Hill, C., Hodges, J., Jacquemart, D., Jolly, A., Lamouroux, J., Roy, R. L., Li, G., Long, D., Lyulin, O., Mackie, C., Massie, S., Mikhailenko, S., Müller, H., Naumenko, O., Nikitin, A., Orphal, J., Perevalov, V., Perrin, A., Polovtseva, E., Richard, C., Smith, M., Starikova, E., Sung, K., Tashkun, S., Tennyson, J., Toon, G., Tyuterev, V., and Wagner, G.: The HITRAN2012 molecular spectroscopic database, Journal of Quantitative Spectroscopy and Radiative Transfer, 130, 4 – 50, doi:http://dx.doi.org/10.1016/j.jqsrt.2013.07.002, 2013.

Rozanov, V., Rozanov, A., Kokhanovsky, A., and Burrows, J.: Radiative transfer through terrestrial atmosphere and ocean: Software package SCIATRAN, Journal of Quantitative Spectroscopy and Radiative Transfer, 133, 13 – 71, doi:http://dx.doi.org/10.1016/j.jqsrt.2013.07.004, 2014.

Saunois, M., Bousquet, P., Poulter, B., Peregon, A., Ciais, P., Canadell, J. G., Dlugokencky, E. J., Etiope, G., Bastviken, D., Houweling, S., Janssens-Maenhout, G., Tubiello, F. N., Castaldi, S., Jackson, R. B., Alexe, M., Arora, V. K., Beerling, D. J., Bergamaschi, P., Blake, D. R., Brailsford, G., Brovkin, V., Bruhwiler, L., Crevoisier, C., Crill, P., Covey, K., Curry, C., Frankenberg, C., Gedney, N., Hoeglund-Isaksson, L., Ishizawa, M., Ito, A., Joos, F., Kim, H.-S., Kleinen, T., Krummel, P., Lamarque, J.-F., Langenfelds, R., Locatelli, R., Machida, T., Maksyutov, S., McDonald, K. C., Marshall, J., Melton, J. R., Morino, I., Naik, V., O'Doherty, S., Parmentier, F.-J. W., Patra, P. K., Peng, C., Peng, S., Peters, G. P., Pison, I., Prigent, C., Prinn, R., Ramonet, M., Riley, W. J., Saito, M., Santini, M., Schroeder, R., Simpson, I. J., Spahni, R., Steele, P., Takizawa, A., Thornton, B. F., Tian, H., Tohjima, Y., Viovy, N., Voulgarakis, A., van Weele, M., van der Werf, G. R., Weiss, R., Wiedinmyer, C., Wilton, D. J., Wiltshire, A., Worthy, D., Wunch, D., Xu, X., Yoshida, Y., Zhang, B., Zhang, Z., and Zhu, Q.: The global methane budget 2000 - 2012, Earth System Science Data, 8, 697–751, doi:10.5194/essd-8-697-2016, http://dx.doi.org/10.5194/essd-8-697-2016, 2016.

Thompson, D. R., Leifer, I., Bovensmann, H., Eastwood, M., Fladeland, M., Frankenberg, C., Gerilowski, K., Green, R. O., Krautwurst, S., Krings, T., Luna, B., and Thorpe, A. K.: Real-time remote detection and measurement for airborne imaging spectroscopy: a case study with methane, Atmospheric Measurement Techniques, 8, 4383–4397, doi:10.5194/amt-8-4383-2015, 2015.

Thompson, D. R., Thorpe, A. K., Frankenberg, C., Green, R. O., Duren, R., Guanter, L., Hollstein, A., Middleton, E., Ong, L., and Ungar, S.: Space-based remote imaging spectroscopy of the Aliso Canyon CH_4 superemitter, Geophysical Research Letters, 43, 6571–6578, doi:10.1002/2016GL069079, 2016.

Trapani, D. D., Bella, G. D., and Viviani, G.: Uncontrolled methane emissions from a MSW landfill surface: Influence of landfill features and side slopes, Waste Management, 33, 2108 – 2115, doi:http://dx.doi.org/10.1016/j.wasman.2013.01.032, 2013.

Tratt, D. M., Buckland, K. N., Hall, J. L., Johnson, P. D., Keim, E. R., Leifer, I., Westberg, K., and Young, S. J.: Airborne visualization and quantification of discrete methane sources in the environment, Remote Sensing of Environment, 154, 74 – 88, doi:http://dx.doi.org/10.1016/j.rse.2014.08.011, 2014.

Xu, L., Lin, X., Amen, J., Welding, K., and McDermitt, D.: Impact of changes in barometric pressure on landfill methane emission, Global Biogeochemical Cycles, 28, 679–695, doi:10.1002/2013GB004571, 2014.

Zien, A. W., Richter, A., Hilboll, A., Blechschmidt, A.-M., and Burrows, J. P.: Systematic analysis of tropospheric NO_2 long-range transport events detected in GOME-2 satellite data, Atmospheric Chemistry and Physics, 14, 7367–7396, doi:10.5194/acp-14-7367-2014, 2014.

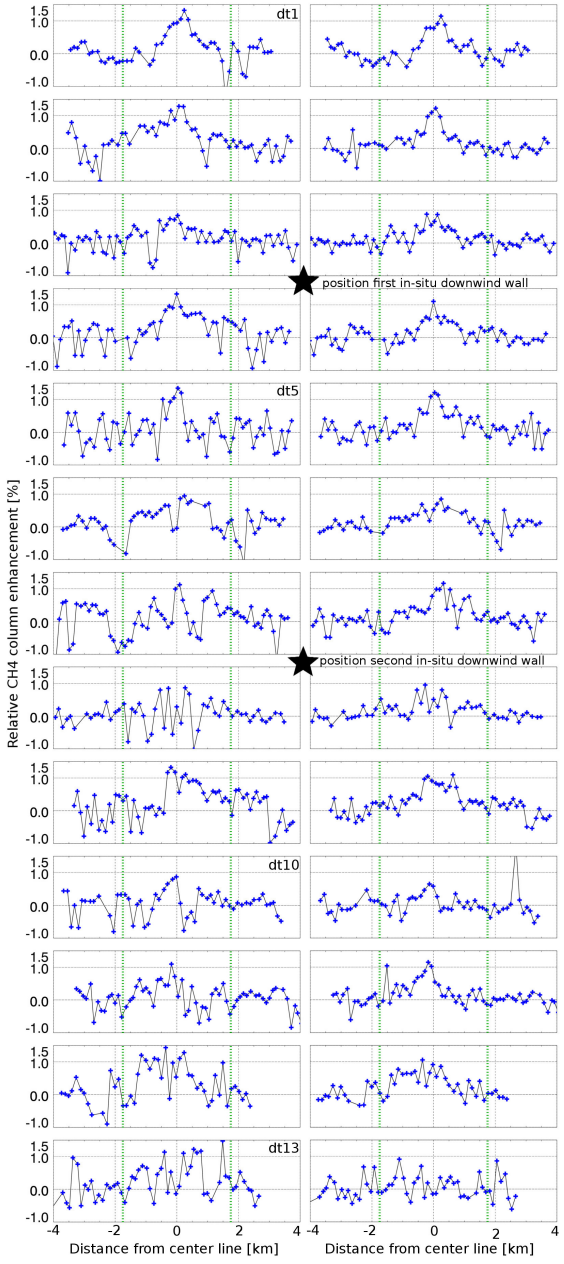

Figure 7. Shown are the 13 downwind tracks (filtered for ~~signal strength~~ detector filling and inclination, dt1 to dt13) from the MAMAP remote survey over the Olinda Alpha Landfill on 01.09.2014, which were used for the emission rate estimate using Eq. 1. The x-axis depicts the distance from the centre line in km (see also Fig. 6, white solid line) and the y-axis gives the CH_4 column enhancement relative to the background column. The area on the left (-4.0 to -1.75 km) and right (+1.75 to +4.0 km) side of the dotted green line was used for background normalisation. Left column: Non-corrected measurements. Right column: ~~Signal strength~~ Detector filling dependency corrected measurements (see Sect. 3.1.2 for details).

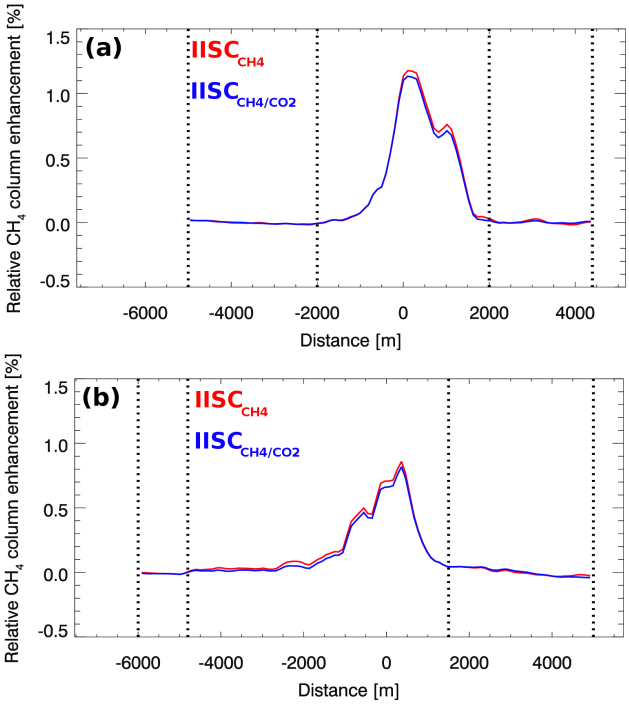

Figure 8. Cross-sections of the relative CH_4 column enhancements determined from the integrated in-situ columns (IISCs) as discussed in Sect. 3.1.1 of the first (a) and second (b) downwind wall of the Olinda Alpha Landfill measurements on 01.09.2014. The blue solid lines ($IISC_{CH_4/CO_2}$) represent the cases which are influenced by the co-emitted CO_2, whereas the red solid lines ($IISC_{CH_4}$) are not. The measurements enclosed by the black dotted lines and located at the flanks / edges of the plume are used for normalization and determination of the background.

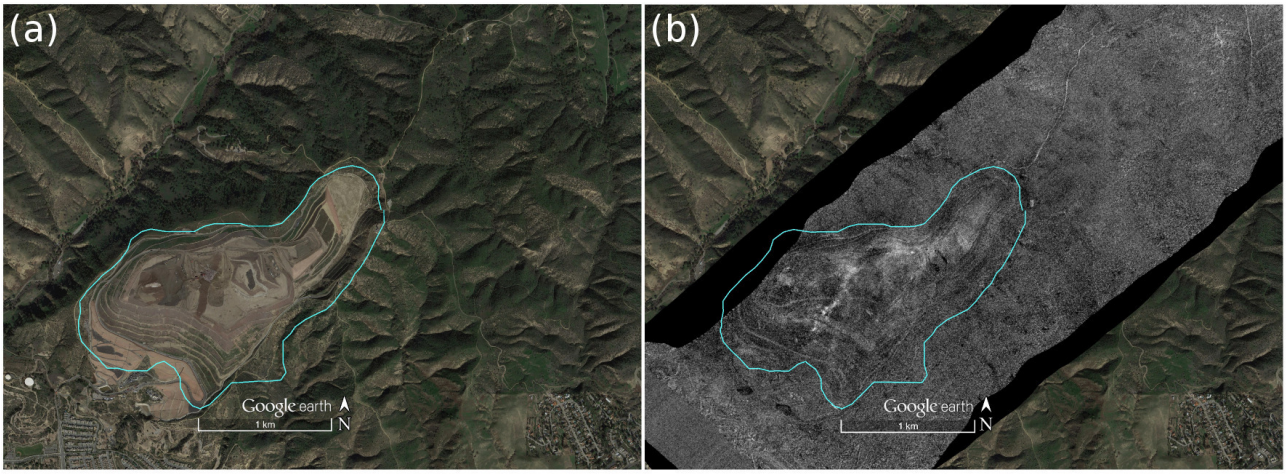

Figure 9. (a) Google Earth map showing the Olinda Alpha Landfill encircled by the cyan solid line. (b) CH_4 anomaly map derived from AVIRIS-NG data and superimposed on the Google Earth map. Shown is the near field around the landfill acquired at around 13:33 local time. White pixel corresponds to a detected CH_4 enhancement. Wind direction was approximately south-west. An enhanced version of the same flight line and view is shown in Fig. 11.

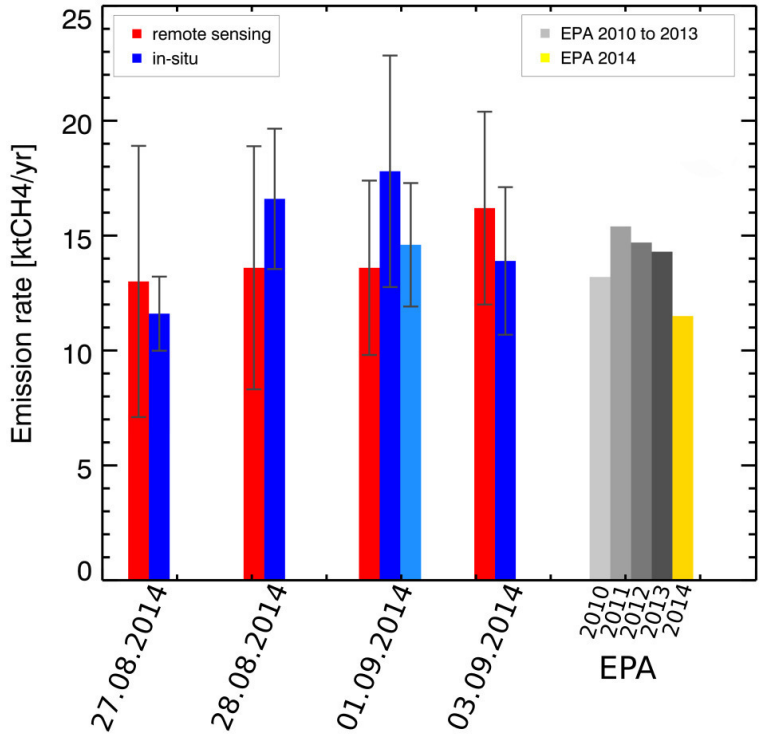

Figure 10. The bar charts show the derived emissions and inventory values. The first four sets of bars depict the derived emissions from this study based on the remote sensing (red), in-situ (blue; on the 01.09.2014: Dark blue: Downwind wall 1, bright blue: Downwind wall 2) measurements and their related errors (vertical bars). The fifth set shows the EPA inventory values for the years 2010 to 2013 (grey shaded) and 2014 (yellow).

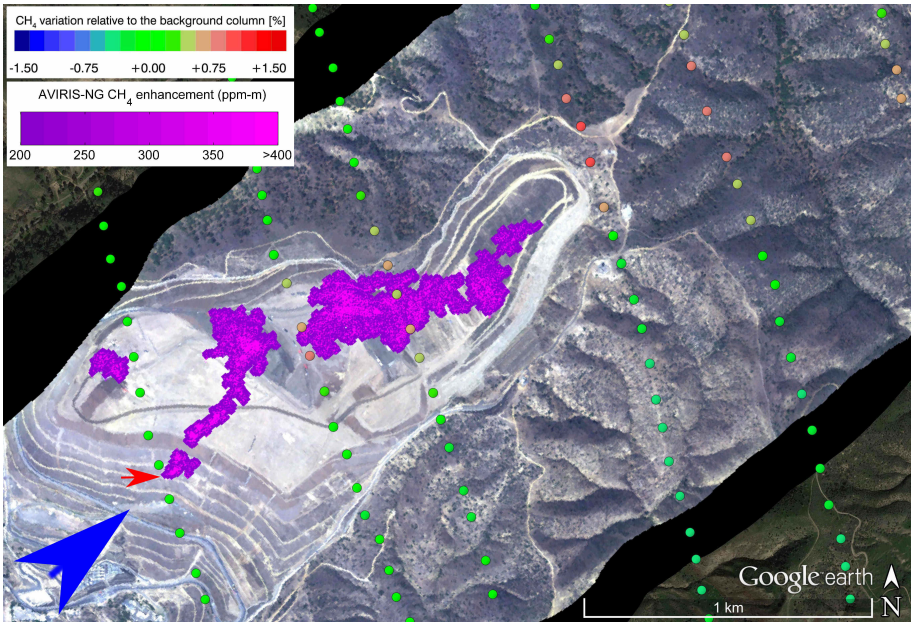

Figure 11. The MAMAP remote sensing (coloured circles) and the AVIRIS-NG (pink shaded areas) measurements on the 03.09.2014 are shown. The RGB map underneath is also based on AVIRIS-NG observations. For better source attribution, only AVIRIS-NG measurements having a methane column enhancement of larger than 200 $\mathrm{ppm} \cdot \mathrm{m}$ are shown. The non threshold filtered flight track is depicted in the Fig. 9 (b). The blue arrow depicts the approximate wind direction. Map underneath visible in the upper left and bottom right corner is provided by Google Earth.

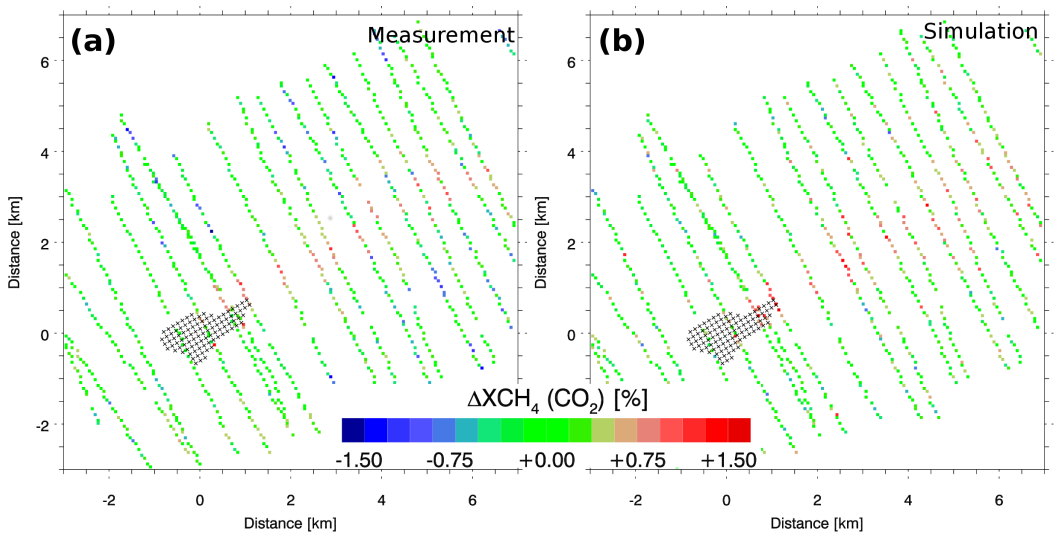

Figure 12. Shown are CH_4 variations relative to the background column for the Olinda Alpha Landfill in the 01.09.2014. (a) Shows the actual acquired data set similar to that show in Fig. 1 and (b) shows the results from the OSSE. Both data sets are gridded. The crosses represent the sources which were used in the OSSE and are homogeneously distributed across the landfill. The wind direction was south-west. For further details see text and supplementary material Sect. S8.

S1 MAMAP remote sensing measurments (Google Earth overlays and single tracks)

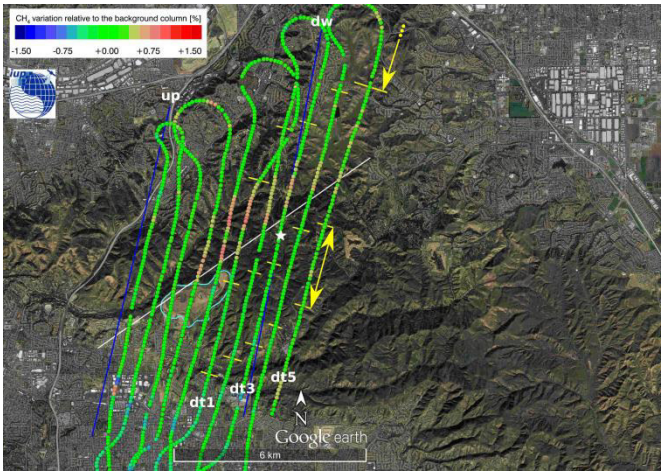

Figure S 1. As Fig. 6 (a) but for the 27.08.2014 and the star corresponds to the origin used in Figs. S5 (c,d) and S9 (a).

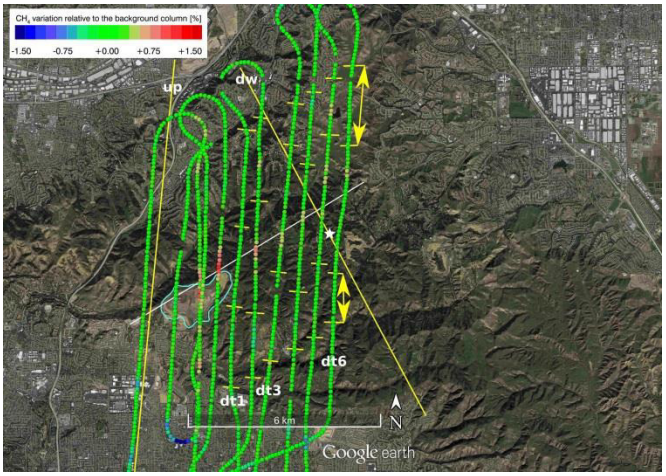

Figure S 2. As Fig. 6 (a) but for the 28.08.2014 and the star correspond to the origin used in Figs. S6 (c,d) and S9 (b).

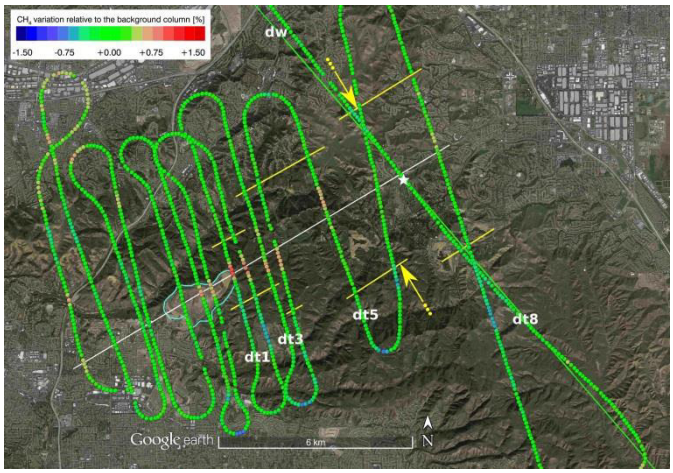

Figure S 3. As Fig. 6 (a) but for the 03.09.2014 and the star correspond to the origin used in Figs. S8, S9 (c).

27.08.2014 28.08.2014 03.09.2014

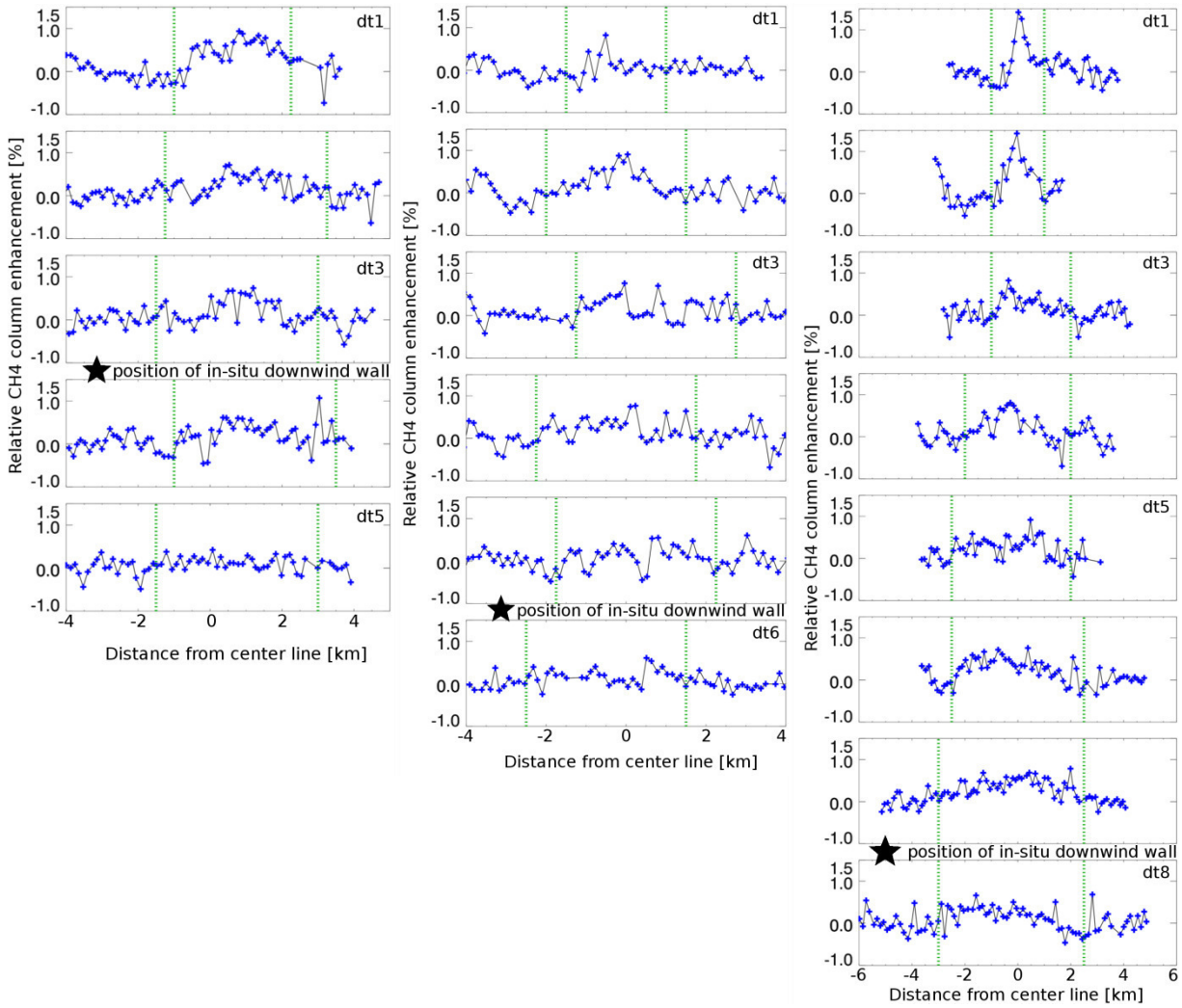

Figure S 4. As Fig. 7 (left column) but for the three other days (from left to right): 27.08.2014, 28.08.2014 and 03.09.2014.

S2 Picarro in-situ dry gas mixing ratis of CH_4

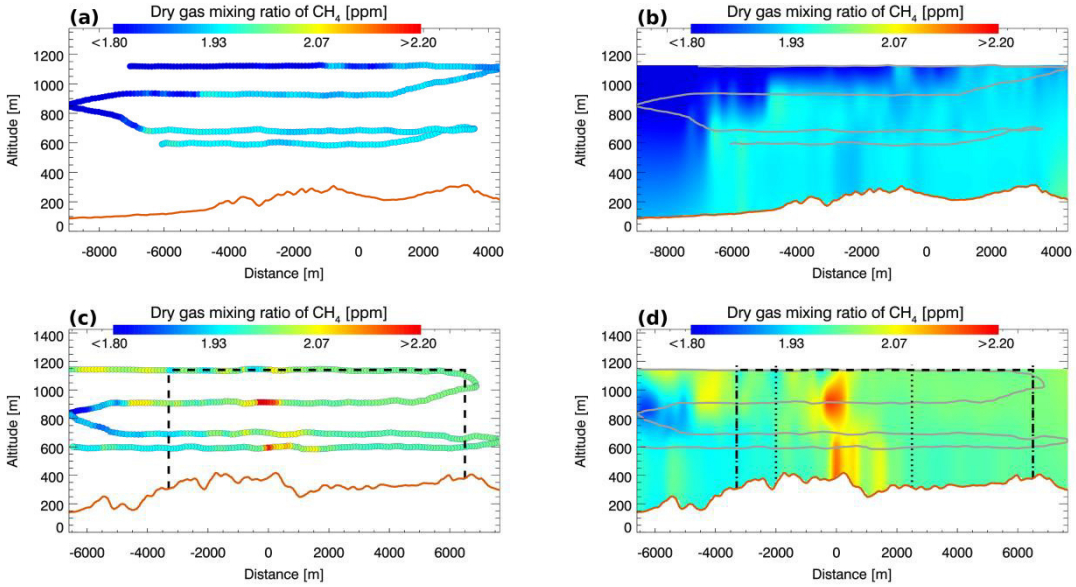

Figure S 5. Dry gas mixing ratios of CH_4 for the upwind (a,b) and downwind (c,d) wall on 27.08.2014. X-axis gives the distance from the approximate plume centre in m (only for bottom panels) and y-axis gives the altitude in m above mean sea level (m amsl). Solid orange line depicts the surface elevation at the position of the wall (based on SRTM). Dashed black line depicts the area, which was used in the mass balance approach for estimating the emission rate. Dotted black line shows limits, which were used to define the background area (here: from - 3300 to - 2000 m and 2500 to 6500 m). Solid grey line depicts the flight track. (a,c) Measured dry gas mixing ratios of CH_4 along the flight track. Each circle represents one measurement. (b,d) Kriged dry gas mixing ratios of CH_4 based on the measurements shown in (a) and (b) and an additionally added pseudo surface track (not shown).

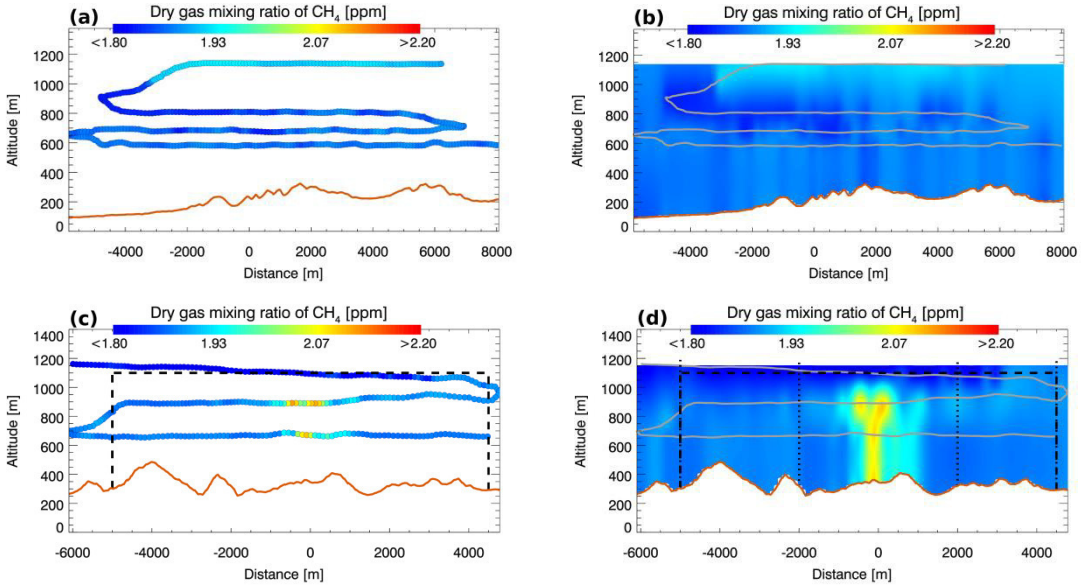

Figure S 6. As for Fig. S5 but for the 28.08.2014. (a,b) Upwind wall. (c,d) Downwind wall.

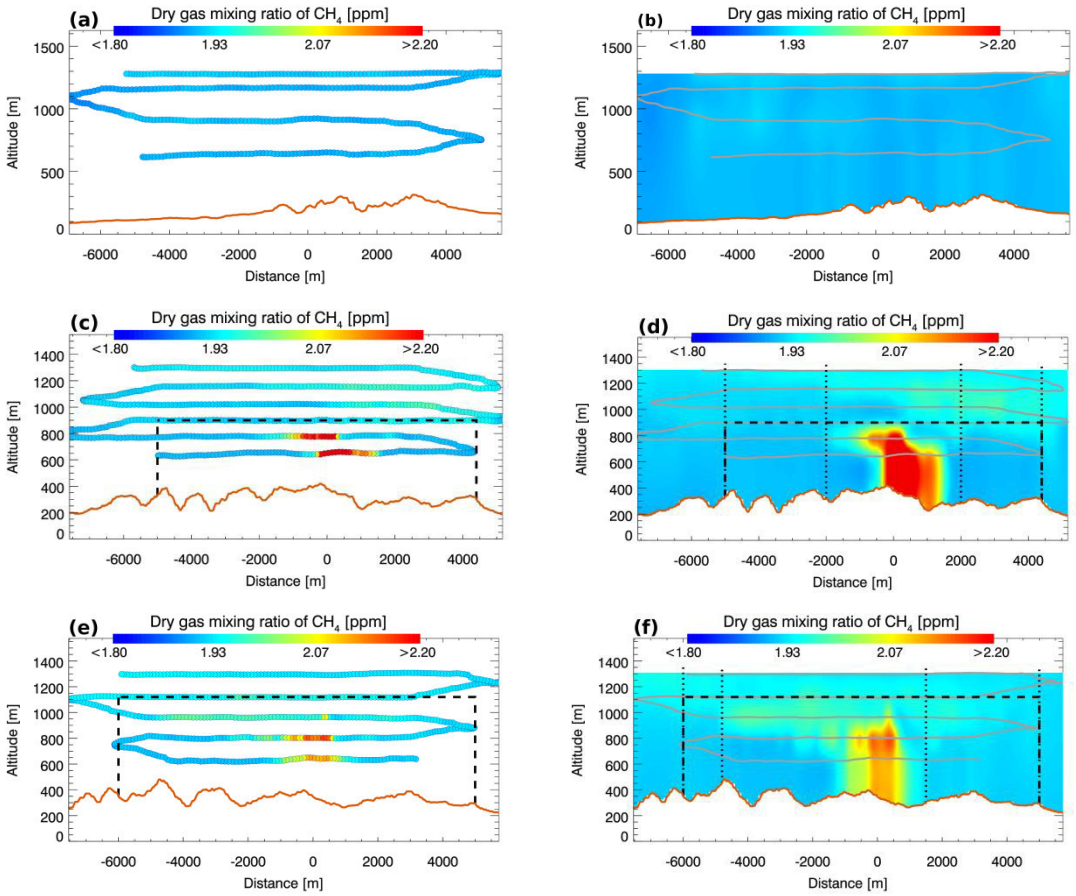

Figure S 7. As for Fig. S5 but for the 01.09.2014. (a,b) Upwind wall. (c,d) First downwind wall. (e,f) Second downwind wall.

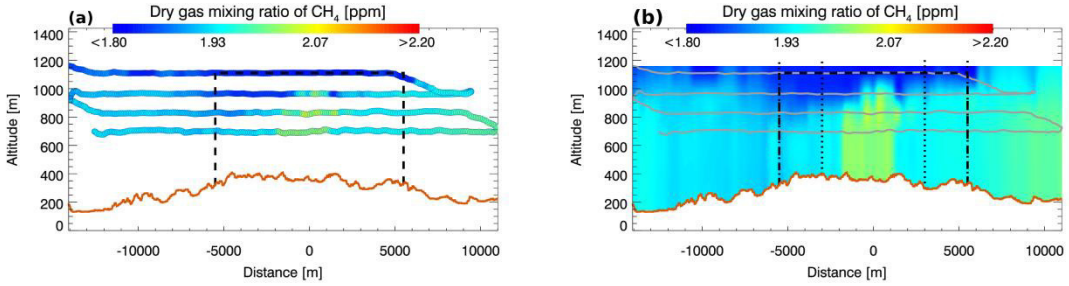

Figure S 8. As for Fig. S5 but for the 03.01.2014. (a,b) Downwind wall.

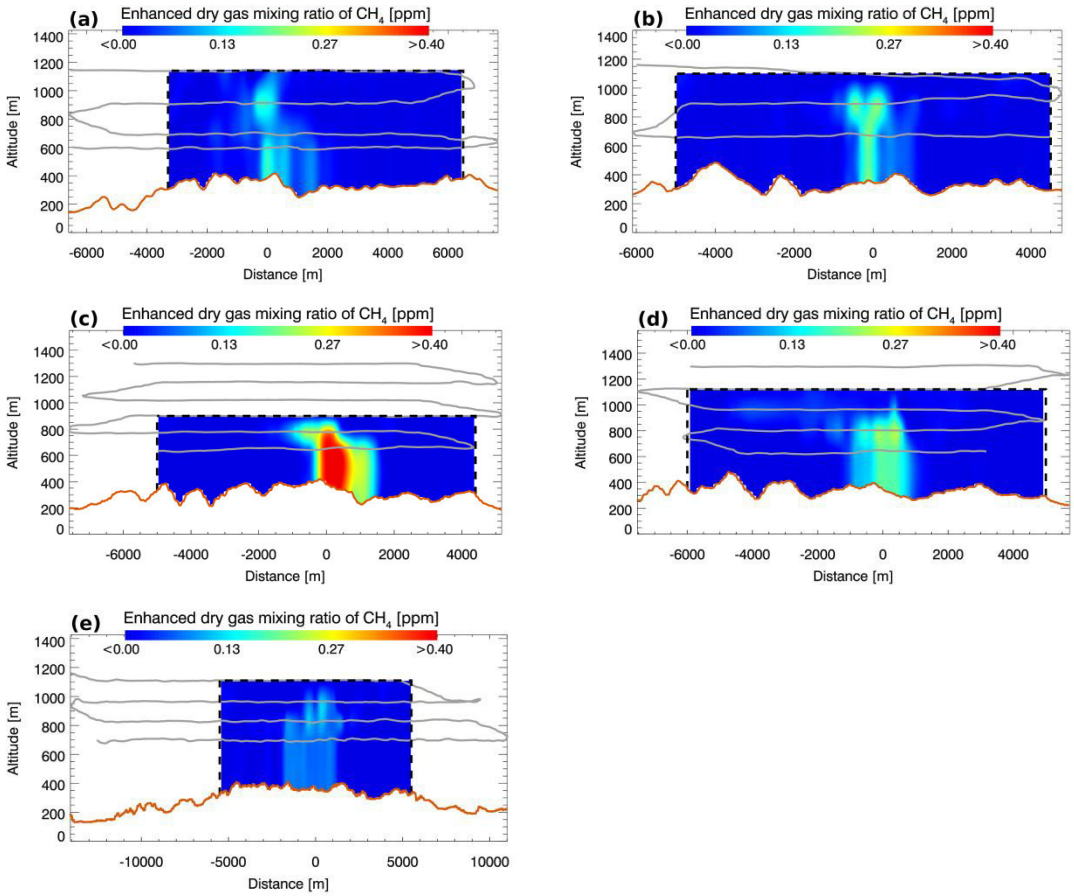

Figure S 9. Shown are enhanced dry gas mixing ratios of CH_4 of the five downwind walls acquired on the four different flight days 27.08.2014 (a), 28.08.2014 (b), 01.09.2014 (c, first downwind wall; d, second downwind wall) and 03.09.2014 (e). Only the area, which was used in the mass balance approach, is shown (dashed black line). Solid orange line depicts the surface elevation at the position of the wall (based on SRTM). Solid grey line shows the flight track.

S3 Picarro in-situ dry gas mixing ratios of CO_2

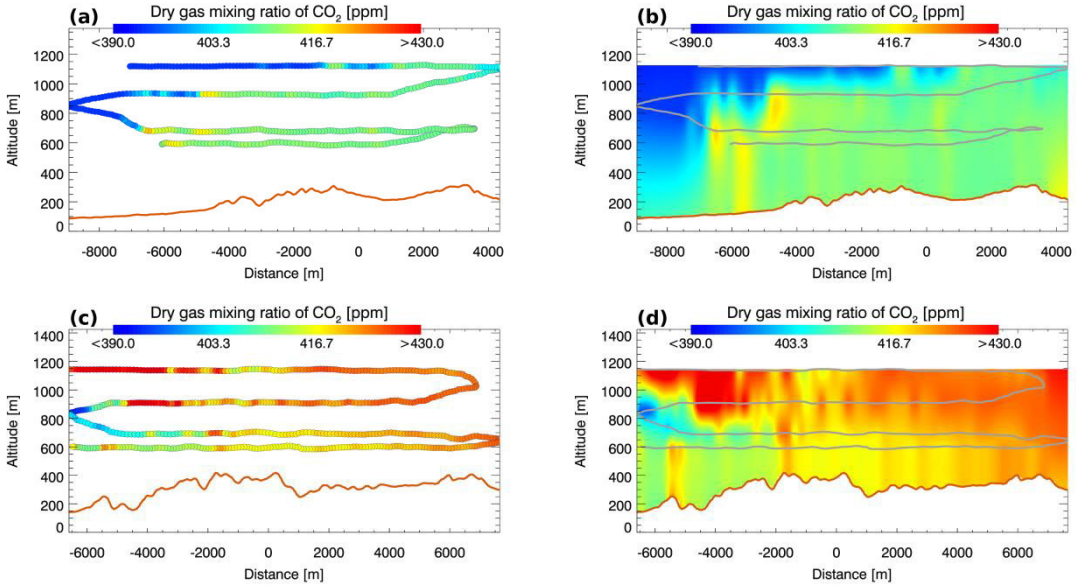

Figure S 10. As Fig. S5 but for the dry gas mixing ratios of CO_2 on 27.08.2014 and without dashed and dotted lines. (a,b) Upwind wall. (c,d) Downwind wall.

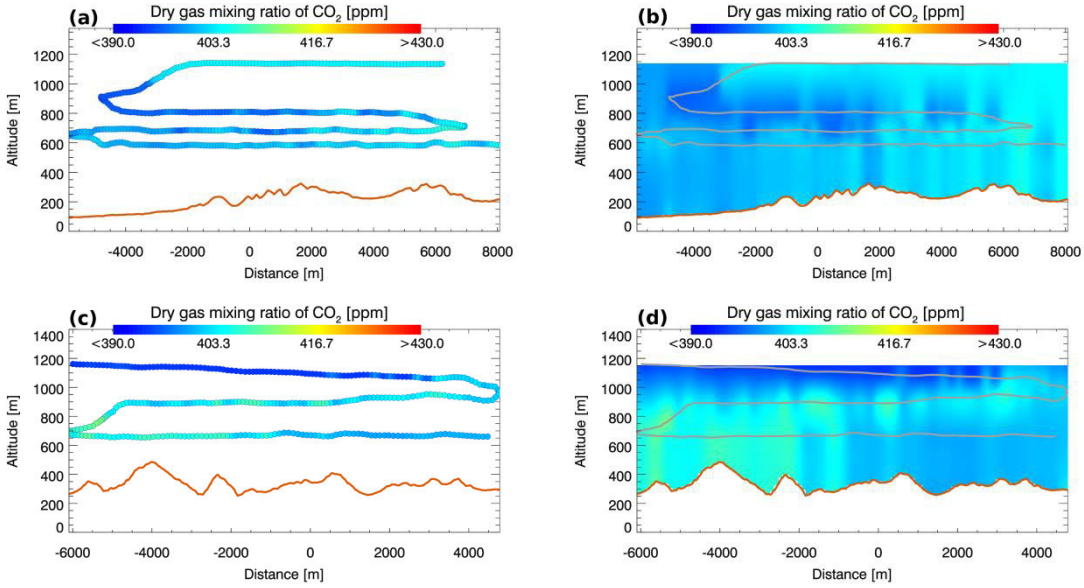

Figure S 11. As for Fig. S10 but for the 28.08.2014. (a,b) Upwind wall. (c,d) Downwind wall.

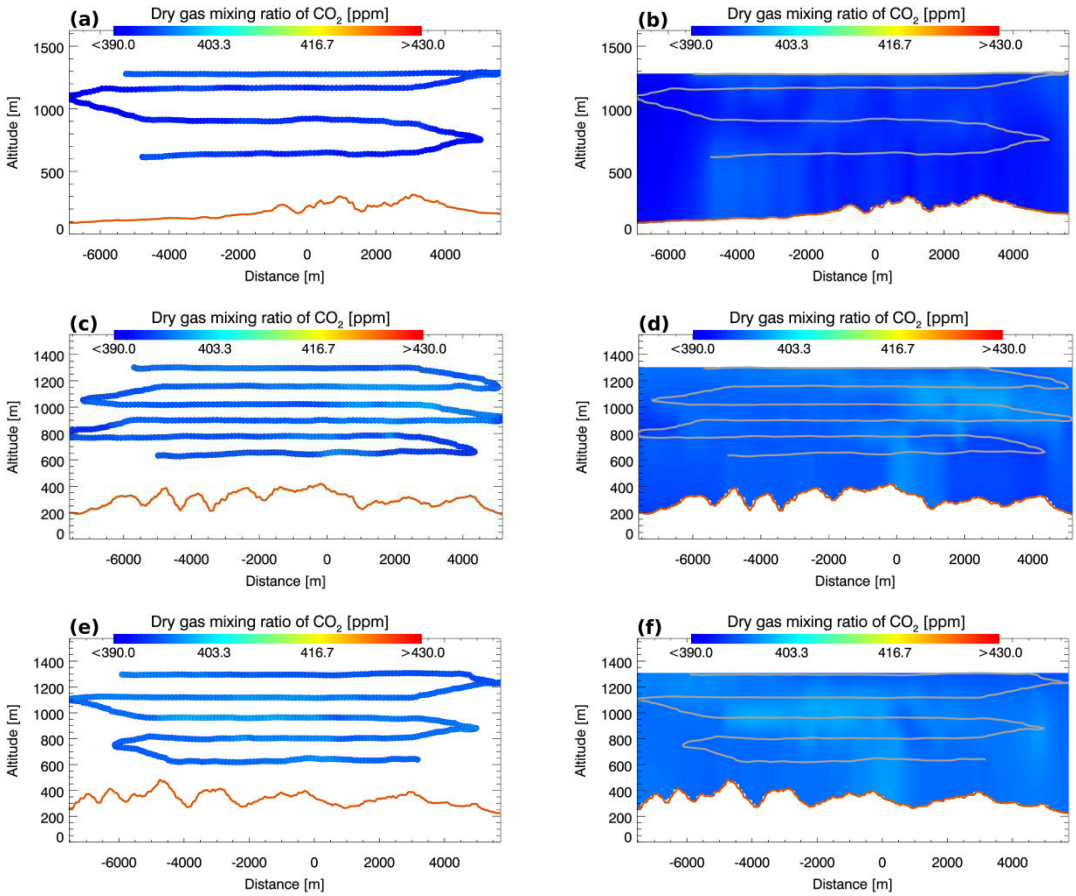

Figure S 12. As for Fig. S10 but for the 01.09.2014. (a,b) Upwind wall. (c,d) First downwind wall. (e,f) Second downwind wall.

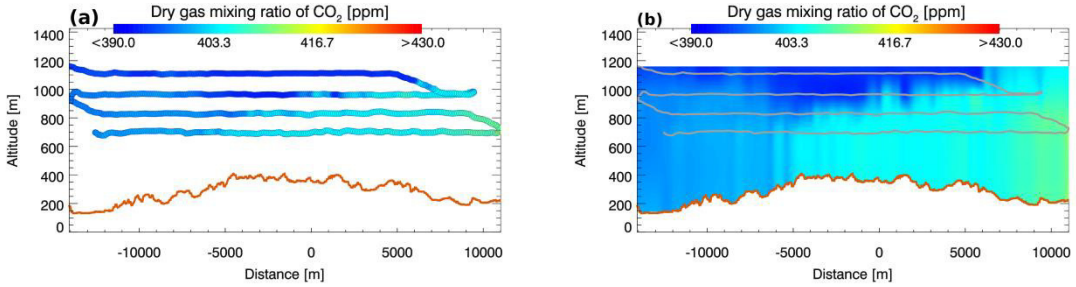

Figure S 13. As for Fig. S10 but for the 03.01.2014. (a,b) Downwind wall.

S4 Horizontal wind fields u_{eff} used in the mass balance approach

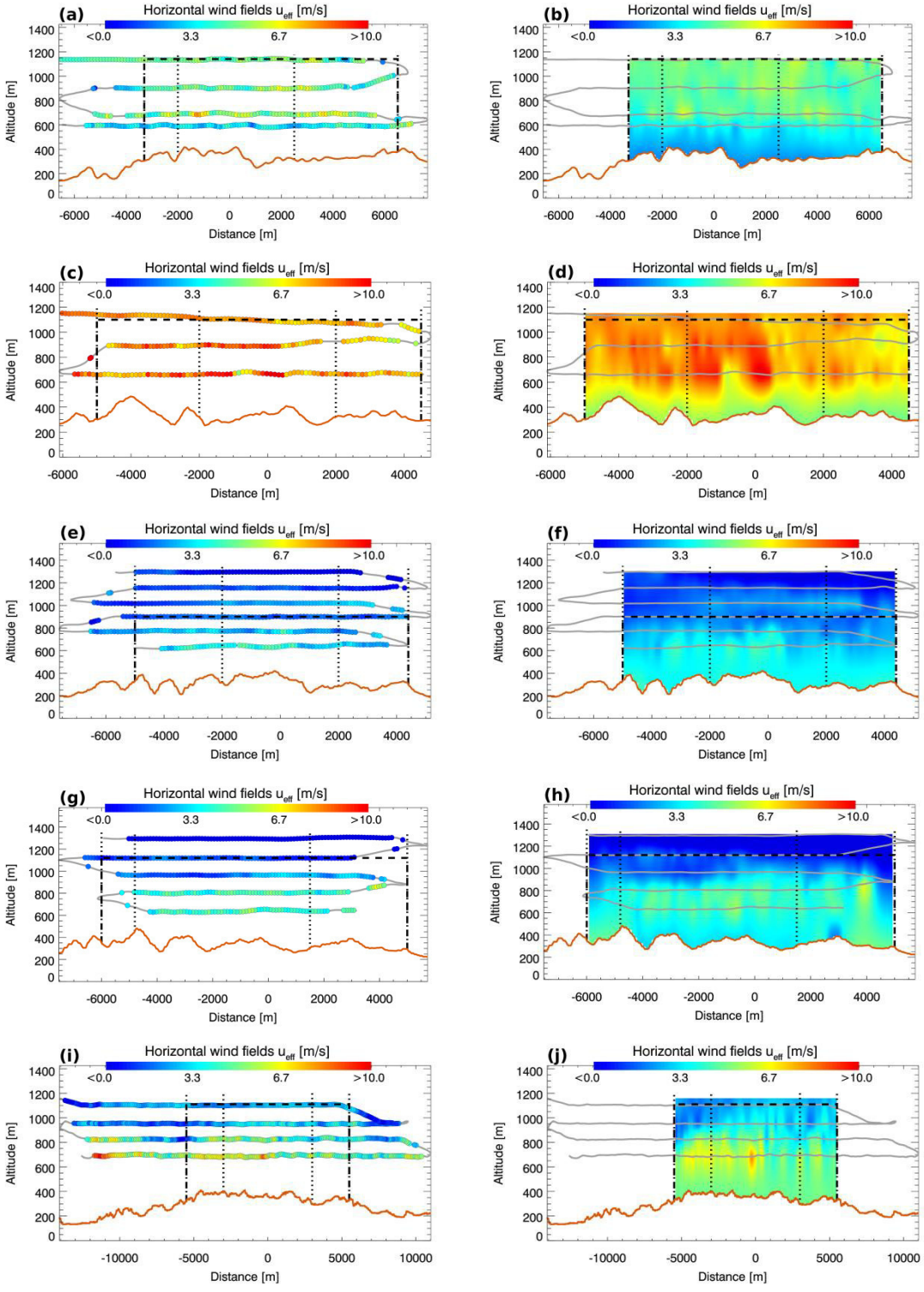

Figure S 14. Shown are the horizontal wind fields u_{eff} of the five downwind walls used in the mass balance approach acquired on the four flight days 27.08.2014 (a,b), 28.08.2014 (c,d), 01.09.2014 (e,f, first downwind wall; g,h, second downwind wall) and 03.09.2014 (i,j). Measurements are filtered by an inclination of 5° (see also main text). The area used in the mass balance approach is bordered by a dashed black line. Dotted black line shows limits, which were used to define the CH_4 background area. Solid orange line depicts the surface elevation at the position of the wall (based on SRTM). Solid grey line shows the flight track.

S5 Integrated in-situ columns (IISC)

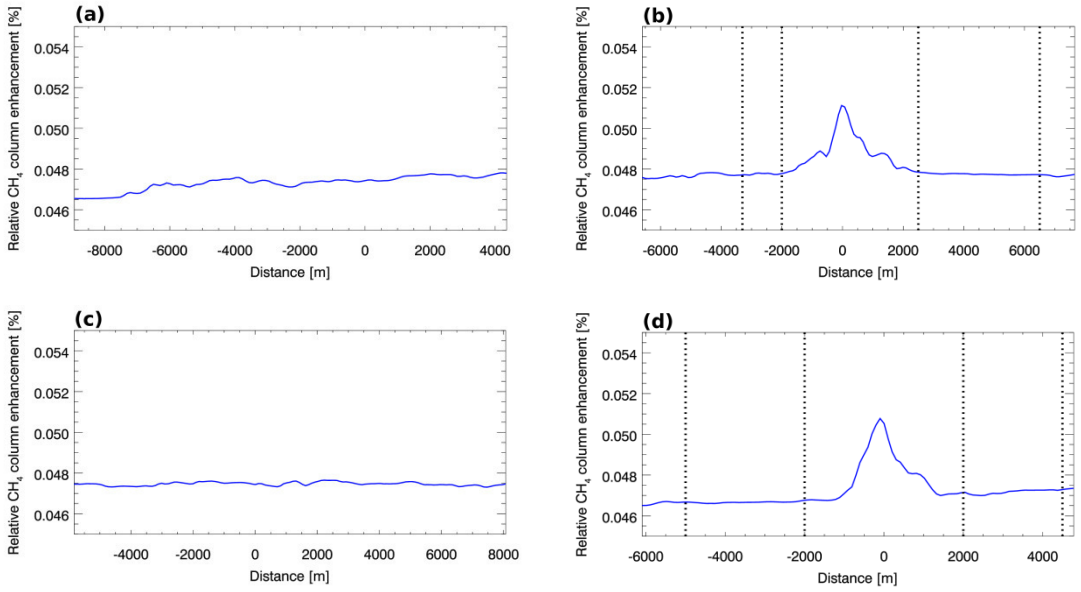

Figure S 15. Ratios of the integrated in-situ columns of CH_4 and CO_2 for the upwind walls (a,c) and downwind walls (b,d) on the 27.08.2014 (a,b) and 28.08.2014 (c,d). The measurements enclosed by the black dotted lines and located at the flanks / edges of the plume are used for normalization (compare to Fig. S17).

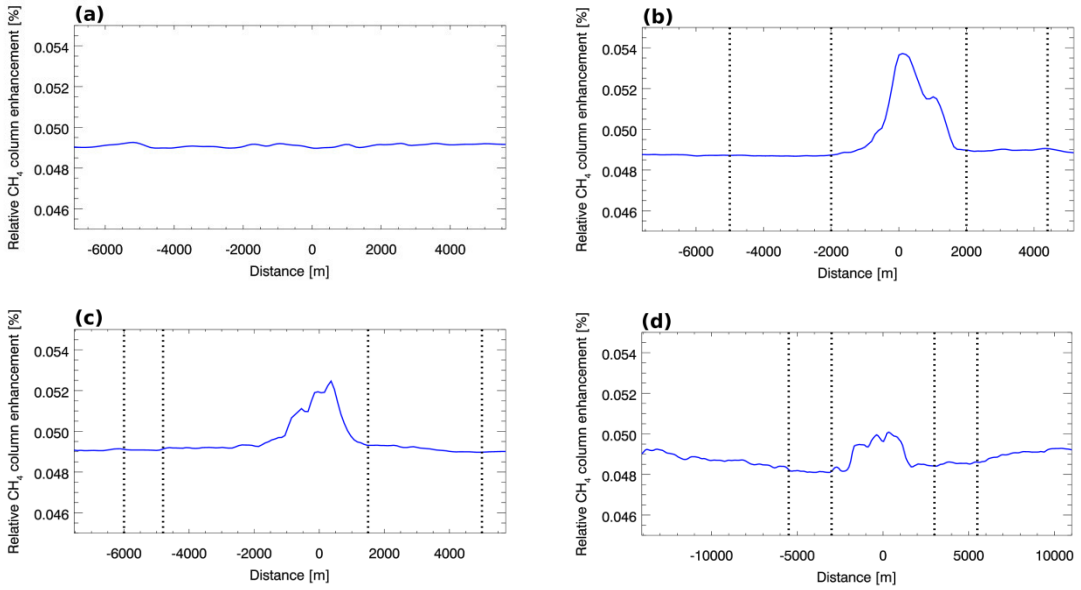

Figure S 16. As Fig. S15 but for the upwind wall (a), first downwind wall (b) and second downwind wall (c) on the 01.09.2014 and the downwind wall (d) on the 03.09.2014 (also compare to Fig. S17).

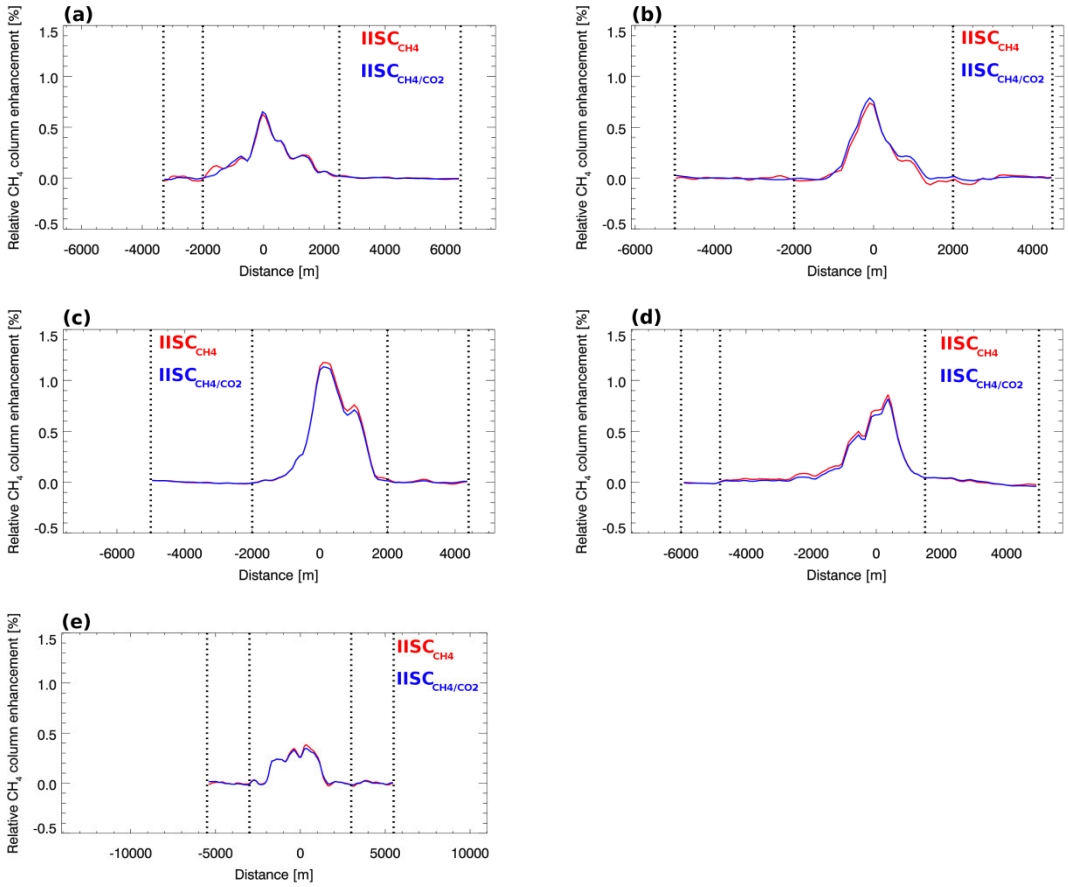

Figure S 17. As Fig . 7 but for all downwind walls. (a) 27.08.2014. (b) 28.08.2014. (c) 01.09.2014, first downwind wall (as in Fig. 7, a). (d) 03.09.2014, second downwind wall (as in Fig. 7, b). (e) 03.09.2014.

S6 AVIRIS-NG CH_4 retrieval results (Google Earth overlays)

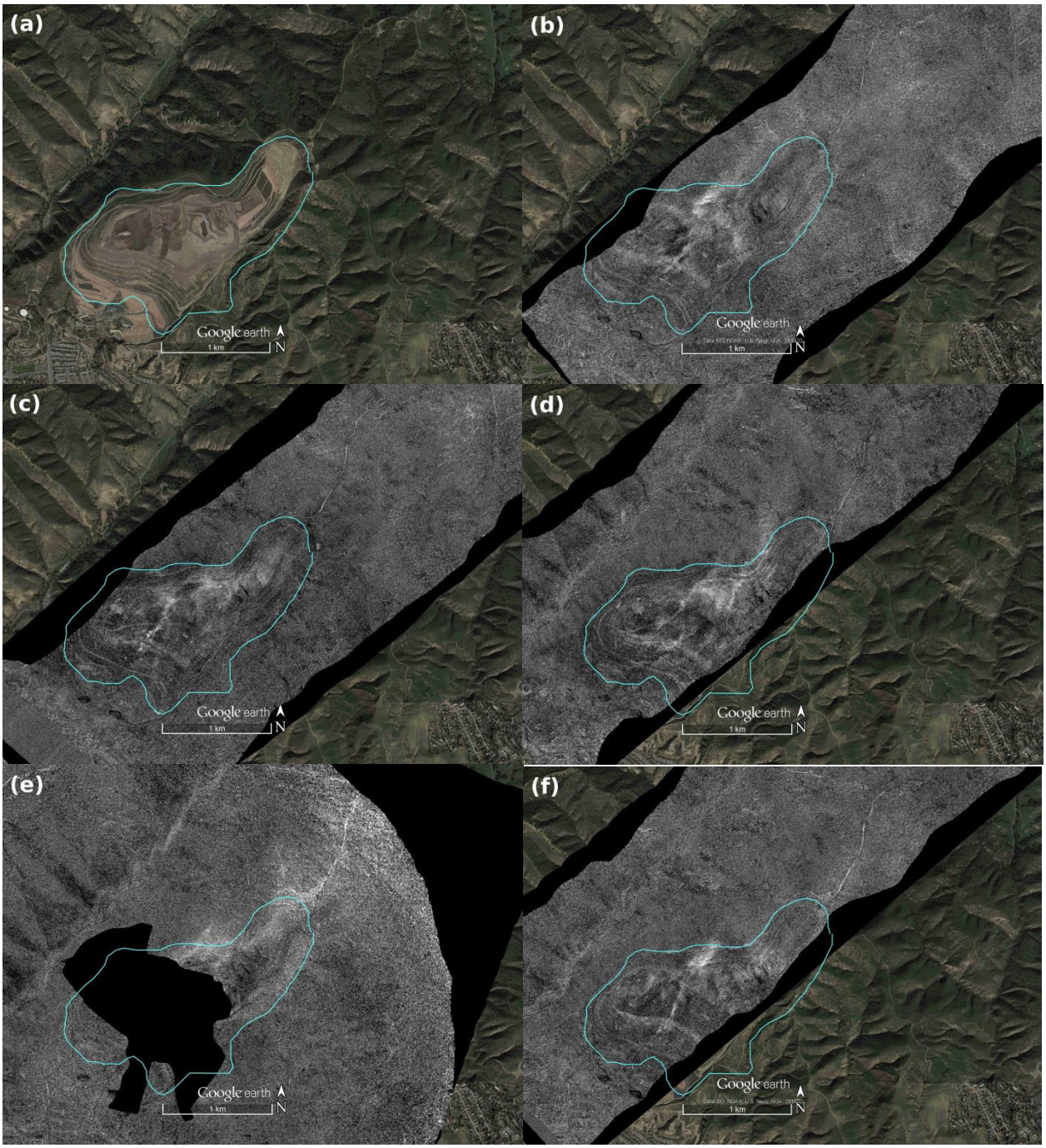

Figure S 18. Overview of the methane retrieval results from the AVIRIS-NG observations from different overflight times [local time]: a) Underlying Google Earth Map of the Olinda Alpha Landfill which is emphasized by the cyan solid line. (b) 13:31. (c) 13:33, same overflight as shown in Fig. 9 in the main part. (d) 13:38. (e) 13:48. (f) 14:06.

S7 Vertical background profiles of CO_2 and CH_4

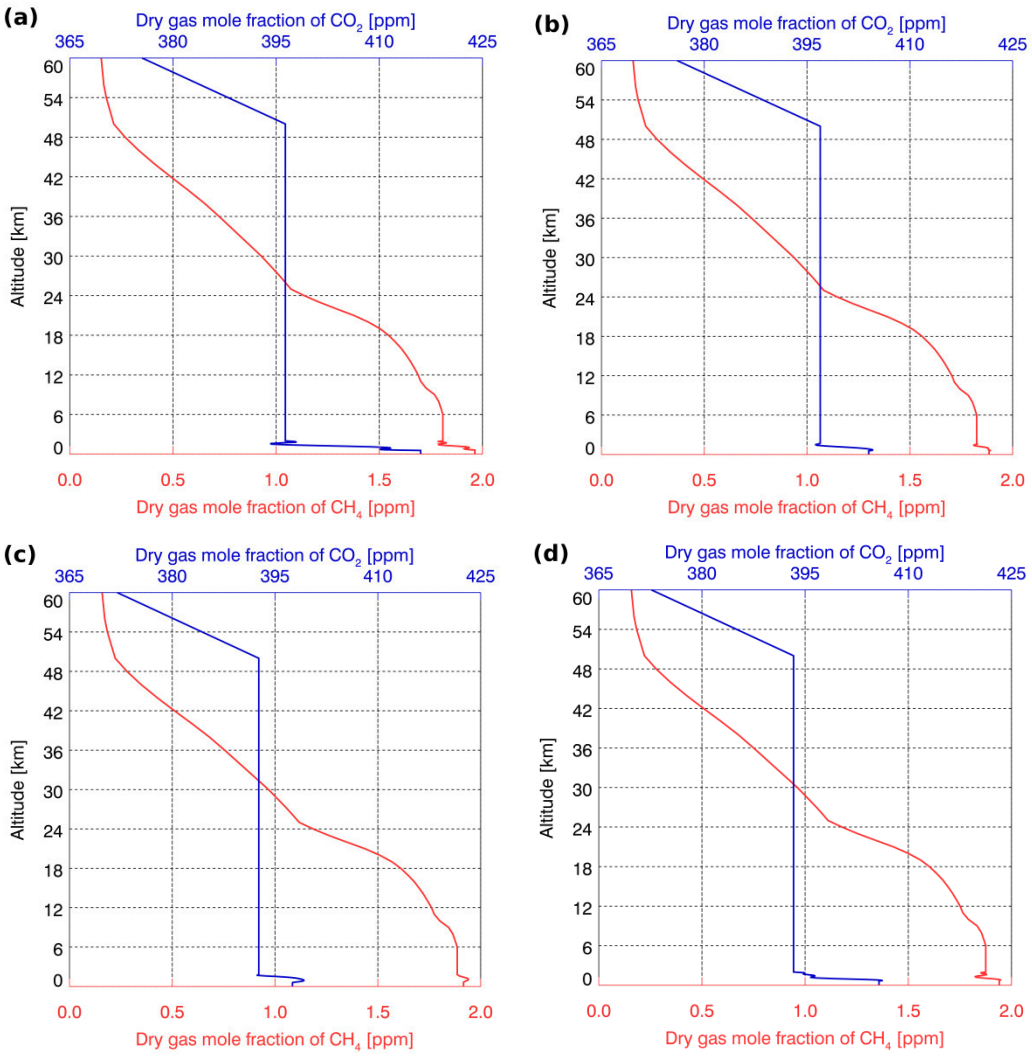

Figure S 19. Shown are the scaled background profiles (as described in Sect. 3.1 of the main manuscript), which were used in the MAMAP remote sensing retrieval: (a) 27.08.2014. (b) 28.08.2014. (c) 01.09.2014. (d) 03.09.2014

S8 Observation System Simulation Experiment (OSSE)

Observation System Simulation Experiments (OSSEs) can be used to simulate the propagation of plumes in the atmosphere originating from various source types and how these plumes would look like if they were measured by, e.g., the MAMAP remote sensing instrument. That means they can be used to qualitatively estimate whether an emission source is observable with the MAMAP remote sensing instrument considering prevailing atmospheric conditions as well as instrumental and flight specific characteristics. The method discussed in the following has been used to estimate, for example, upper-limit emission rates of CH_4 for a blowout site located in the North Sea (Gerilowski et. al., 2015) and is based on vertically integrated Gaussian plume forward model simulations (for details, see Krings et. al., 2011 and Gerilowski et al., 2015):

$$V(x,y) = \sum_{i=1}^{N} \frac{F_i}{\sqrt{2\pi}\,\sigma_y(a,x_i)u}\ \exp\left(-\frac{1}{2}\left(\frac{y_i}{\sigma_y(a,x_i)}\right)\right) \qquad \text{Eq. S1}$$

where $V(x,y)$ is the vertically integrated column, which is subsequently normalized by the background column to achieve, e.g., the desired CH_4 variation relative to the background column, as a result of one or more emission sources i having emission rates F_i, u is the prevailing wind speed which is assumed to be constant across the entire simulation and measurement area, respectively, $\sigma_y(a,x_i)$ is the horizontal dispersion coefficient in across wind direction with the parameter a which depends, in a first order approximation, on wind speed and solar insolation, x_i is the along wind coordinate and y_i the across wind coordinate of source i. The sigma sign indicates the summation over all possible sources i.

In order to simulate emissions from the landfills under investigation, it was assumed that CH_4 emissions took place homogenously distributed across the entire landfill. Therefore, depending on the shape and size of the landfill 90 to 100 single sources were homogenously distributed across the landfill area. Table S1 summarises the parameters necessary for the simulations of the four landfills shown in Fig. 1 in the main manuscript. As these simulations are compared to the actual MAMAP remote sensing measurements, all parameters were derived from the corresponding measurement flights. In order to estimate the wind directions and wind speeds at the BKK Landfill (BKK), Puente Hills Landfill (PHL) and Scholl Canyon Landfill (SCL) sites, we assumed the same vertical wind profile as measured for the Olinda Alpha Landfill (OAL) flight on the corresponding day, but scaled based on a comparison of the surface winds measured by weather stations at the time, the landfills were surveyed. The BKK and PHL are close to the OAL. Therefore, the weather station at the OAL was used to estimate their surface winds. For the SCL, we used the weather station KCAGLEND17 (https://www.wunderground.com/personal-weather-station/dashboard?ID=KCAGLEND17#history/tgraphs/s20140827/e20140827/mdaily) close to this landfill site. For the simulation of, e.g., the BKK Landfill on the 01.09.2014, the surface wind speed and, thus, the wind speed used for the simulation, was the same as for the subsequent OAL flight (4.4 ms^{-1}). The EPA emission rate estimate is 15.1 $ktCH_4yr^{-1}$ for 2014, which was equally distributed over the approximate 100 sources. The parameter a used for the horizontal dispersion coefficient σ_y is based on the atmospheric stability classification (Turner, 1970) using the wind speed and solar insolation. Thus, a wind speed of 4.4 ms^{-1} and strong solar insolation results in stability class B corresponding to a value of a = 156 (Martin, 1976).

	BKK, 01.09.2014	SCL, 27.08.2014	PHL, 27.08.2014	OAL, 01.09.2014
Time of overflight	14:26 – 14:54	11:27 – 12:03	12:17 – 13:20	14:55 – 16:05
Emission rate [$ktCH_4yr^{-1}$]	15.1	5.9	5.0	14.3
Surface area [km^2]	1.4	0.85	2.4	1.7
Stability class	B	A - B	B	B
Parameter a	156	185	156	156
Wind speed [ms^{-1}]	4.4	2.5	4.0	4.4
Wind direction [°]	235	210	227	238
Ground scene size [m^2]	69	63	46	64
Precision [%]	0.30	0.27	0.33	0.34

Table S1: Summery of the relevant quantities used in the Observation System Simulation Experiments (OSSEs).

Figure S20 (a) shows such a simulation for the BKK Landfill. The resulting column enhancement has also been gridded to pixels having the same size as the approximate ground scene size of the MAMAP remote sensing flight on that day (~ 69 m^2) for better comparison. The simulated plume has additionally been rotated in the prevailing wind direction (235°). In the next step (Fig. S20, b), a noise component was added to the simulation to replicate the single measurement precision of the MAMAP remote sensing instrument. The noise was calculated as 1-σ standard deviation (0.30%) from the actual MAMAP remote sensing measurements over the BKK Landfill. In the final step (Fig. d), simulated grid points were only plotted if the MAMAP instrument also gathered data at the specific positions, that is: along the flight track. For comparison, the actual MAMAP flight track over the BKK Landfill on the 01.09.2014 is shown in Fig. S20 (c). From that, one concludes that if the BKK landfill had emitted 15.11 $ktCH_4yr^{-1}$ at the time of the measurement, it should likely have been observable by the MAMAP remote sensing instrument (for details, see also main text). The comparison of measurements and simulations for the Scholl Canyon Landfill and Puente Hills Landfill are shown in Fig. S21 and for the Olinda Alpha in Fig. 12 in the main manuscript (Sect. 4.7, including the conclusions from these experiments).

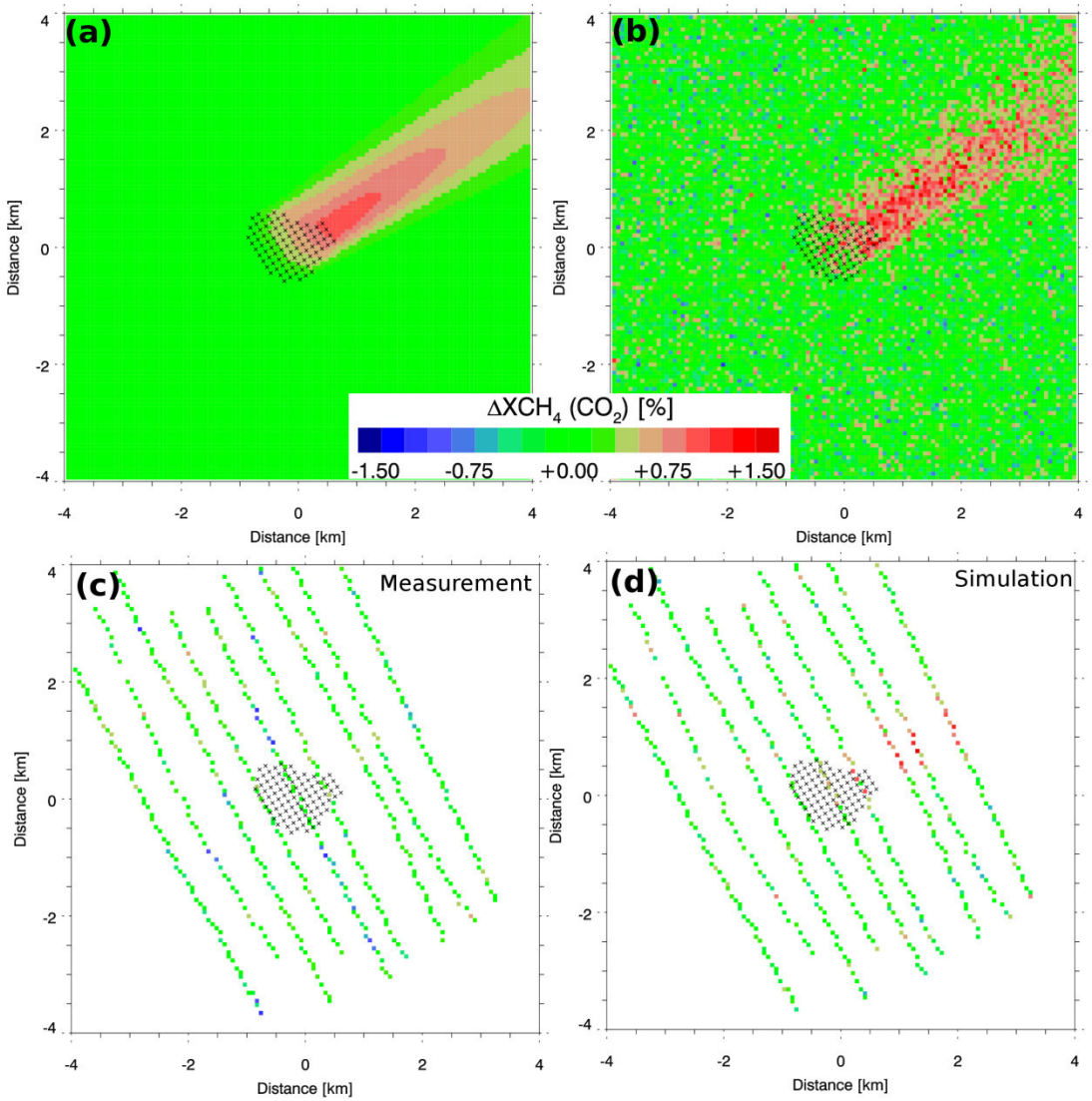

Figure S 20. (a) Shows the CH_4 variation relative to the background column for the BKK Landfill on the 01.09.2014 based on the OSSE. (b) Shows the same as (a) but with an added noise component. (d) Shows the OSSE only at the position where actual measurement have been acquired. (c) Actual measurement of the MAMAP remote sensing instrument.

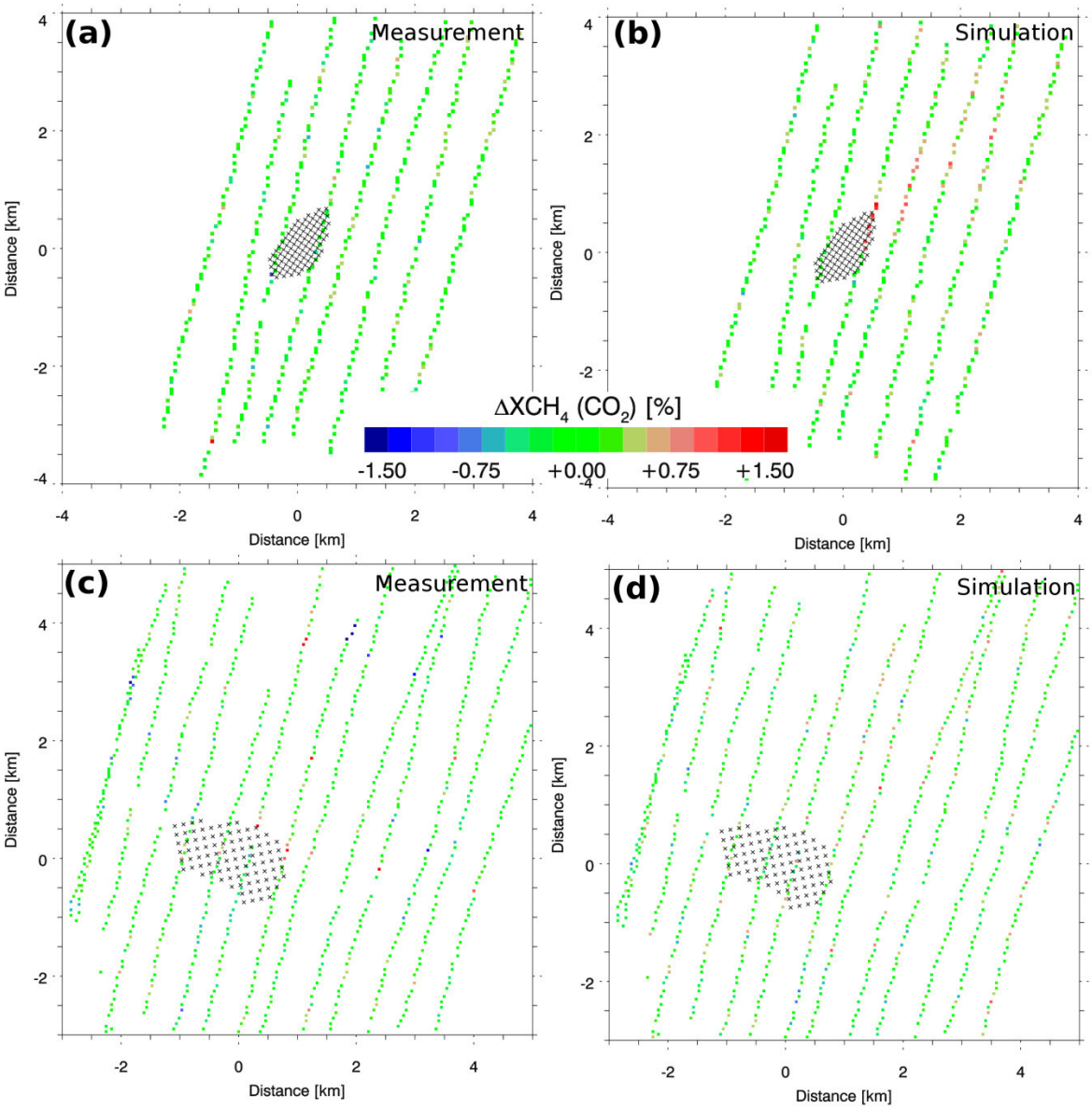

Figure S 21. As Fig. 12 but for the SCL on the 27.08.2014 (a,b) and for the PHL on the 27.08.2014 (c,d).

S9 Landfill reporting practice in the U.S.

In the U.S., landfill operators need to report landfill emissions, in case the landfill is equipped with a gas collection system, in two different ways to the United States Environmental Protection Agency (GPO, 2013). The first approach (A1, forward calculation approach) is driven by model data using, e.g., the type and amount of waste, which has historically been deposit within a landfill in combination with a first order decay model. The second approach (A2, back calculation approach) is driven by measurements of the amount of CH_4, which has been recovered by the gas collection system, and gas collection efficiencies to estimate CH_4 emissions. The official value stated by EPA always represents the larger estimate of the two.

The landfills Olinda Alpha (OAL), BKK, Scholl Canyon (SCL) and Puente Hills (PHL) investigated in this work are equipped with a gas collection system. An overview of the reported emission rates of the four landfills between 2010 and 2015 is given in Table S2.

		2010	2011	2012	2013	2014	2015
OAL							
Emission in $ktCH_4yr^{-1}$	Official	13.2	15.4	14.7	14.3	11.5	12.3
	A1	11.2	5.9	9.3	10.4	10.0	12.3
	A2	13.1	15.4	14.7	14.4	11.5	9.2
BKK							
Emission in $ktCH_4yr^{-1}$	Official	14.1	13.6	14.6	15.0	15.1	15.1
	A1	14.1	13.6	14.6	15.0	15.1	15.1
	A2	1.3	1.3	1.2	1.0	0.9	0.9
SCL							
Emission in $ktCH_4yr^{-1}$	Official	5.6	6.9	6.5	6.3	5.9	5.3
	A1	0.0	0.0	0.0	1.0	2.1	3.2
	A2	5.6	6.9	6.5	6.3	5.9	5.3
PHL							
Emission in $ktCH_4yr^{-1}$	Official	17.8	17.2	17.2	10.9	5.0	13.4
	A1	8.3	4.1	4.2	7.7	2.4	13.3
	A2	17.8	17.2	17.2	10.9	5.0	4.4

Table S2: Reported emission rates of the four landfills: Olinda Alpha Landfill (OAL), BKK Landfill (BKK), Scholl Canyon Landfill (SCL), Puente Hills Landfill (PHL). The emission rates for the year 2014 are emphasized in yellow. For each landfill and year three emission rates are given: Official (officially reported by EPA), A1 (forward calculation approach) and A2 (back calculation approach, GPO, 2013).

The emission data for the different facilities and landfills, respectively, from Table S2 can be found at the EPA website: https://ghgdata.epa.gov/ghgp/main.do, last access: 09.06.2017.
OAL: https://ghgdata.epa.gov/ghgp/service/facilityDetail/2014?id=1002320&ds=E&et=&popup=true, last access: 09.06.2017.
BKK: https://ghgdata.epa.gov/ghgp/service/facilityDetail/2014?id=1011449&ds=E&et=&popup=true, last access: 09.06.2017.
SCL: https://ghgdata.epa.gov/ghgp/service/facilityDetail/2014?id=1003198&ds=E&et=&popup=true, last access: 09.06.2017.
PHL: https://ghgdata.epa.gov/ghgp/service/facilityDetail/2014?id=1003199&ds=E&et=&popup=true, last access: 09.06.2017.

References

Gerilowski, K., Krings, T., Hartmann, J., Buchwitz, M., Sachs, T., Erzinger, J., Burrows, J. P., and Bovensmann, H.: Atmospheric remote sensing constraints on direct sea-air methane flux from the 22/4b North Sea massive blowout bubble plume, Marine and Petroleum Geology, 68, 824–835, doi:10.1016/j.marpetgeo.2015.07.011, 2015.

GPO: U.S. Government Publishing Office; U.S. Environmental Protection Agency: Rules and Regulations; Federal Register; Vol. 78; No. 230, available at http://www.gpo.gov/fdsys/pkg/FR-2013-11-29/pdf/2013-27996.pdf, last access: 15.05.2017, 2013.

Krings, T., Gerilowski, K., Buchwitz, M., Reuter, M., Tretner, A., Erzinger, J., Heinze, D., Pflüger, U., Burrows, J. P., and Bovensmann, H.: MAMAP - a new spectrometer system for column-averaged methane and carbon dioxide observations from aircraft: retrieval algorithm and first inversions for point source emission rates, Atmospheric Measurement Techniques, 4, 1735–1758, doi:10.5194/amt-4-1735-2011, 2011.

Martin, D. O.: Comment On"The Change of Concentration Standard Deviations with Distance", Journal of the Air Pollution Control Association, 26, 145–147, doi:10.1080/00022470.1976.10470238, http://dx.doi.org/10.1080/00022470.1976.10470238, 1976.

Turner, D. and Administration, U. S. N. A. P. C.: Workbook of Atmospheric Dispersion Estimates, Environmental health series: Air pollution, U.S. Department of Health Education and Welfare, Public Health Service, Environmental Health Service, National Air Pollution Control Administration, 1970.